MODELING TRANSITION METAL CATALYSTS FOR SMALL MOLECULE ACTIVATION AND FUNCTIONALIZATION

Travis M. Figg, B.S.

Dissertation Prepared for the Degree of

DOCTOR OF PHILOSOPHY

UNIVERSITY OF NORTH TEXAS

May 2013

APPROVED:

Thomas R. Cundari, Major Professor
Mohammad A. Omary, Committee Member
Michael G. Richmond, Committee Member
Angela K. Wilson, Committee Member
William E. Acree, Jr., Chair of the Department of Chemistry
Mark Wardell, Dean of the Toulouse Graduate School

Figg, Travis M. *Modeling Transition Metal Catalysts for Small Molecule Activation and Functionalization*. Doctor of Philosophy (Chemistry -Inorganic Chemistry), May 2013, 118 pp., 9 tables, 49 illustrations, chapter references.

There is a high demand for the development of processes for the conversion of ubiquitous molecules into industrially useful commodities. Transition metal catalysts are often utilized for the activation and functionalization of small organic molecules due to their diverse nature and proven utility with a myriad of chemical transformations. The functionalization of methane (CH_4) and dinitrogen (N_2) to methanol (CH_3OH) and ammonia (NH_3) respectively is of particular interest; however, both methane and dinitrogen are essentially inert due to the inherit strength of their bonds. In this dissertation a series of computational studies is performed to better understand the fundamental chemistry behind the functionalization of methane and the activation of dinitrogen in a homogeneous environment. A catalytic cycle is proposed for the oxy-functionalization of methane to methanol. The cycle consists of two key steps: (1) C-H activation across a metal-alkoxide bond (M-OR), and (2) regeneration of the M-OR species through an oxy-insertion step utilizing external oxidants. The C-H activation step has been extensively studied; however, the latter step is not as well understood with limited examples. For this work, we focus on the oxy-insertion step starting with a class of compounds known to do C-H activation (*i.e.,* Pt(II) systems). Computational studies have been carried out in an attempt to guide experimental collaborators to promising new systems. Thus, the majority of this dissertation is an attempt to extend transition metal mediated C-O bond forming reactions to complexes known to perform C-H activation chemistry. The last chapter involves a computational study of the homogeneous cleavage of N_2 utilizing iron-β-diketiminate fragments. This reaction has been studied experimentally, however, the reactive intermediates were not

isolated and the mechanism of this reaction was unknown. Density functional theory (DFT) calculations are carried out to elucidate the mechanism of the reductive cleavage of N_2 via the sequential addition of iron- β-diketiminate fragments to N_2 to form a bis-nitride (N^{3-}) intermediate. The role of potassium promoters on the dinitrogen and bis-nitride species is also investigated.

ACKNOWLEDGEMENTS

I would like acknowledge several people who made my time at the University of North Texas (UNT) one of the most productive and enjoyable times of my life. First and foremost I would like to thank my adviser, Tom Cundari, who introduced me to the world of computational chemistry. His endless patience, enthusiasm toward science, sound advice, and the ability to explain things clearly were invaluable to my scientific growth and professional development. Working under him was truly a great experience and I respect him both as a scientist and as a friend. I would not have been nearly as successful without the fruitful collaborations with my experimental friends. I would like to thank Prof. Brent Gunnoe and Dr. Joanna Webb from the University of Virginia for their contributions to the work highlighted in Chapters 3 and 4. I would also like to thank Prof. Pat Holland from the University of Rochester for the work presented in Chapter 7. I would like to extend my upmost gratitude to my amazing group members within ^{Team}Cundari. Thank you for your friendship, fruitful discussions and obscene amounts of baked goods. I would especially like to thank Dr. Glenn Morello, Cong Liu, and Dr. Bhaskar Chilikuri for helping me understand various modeling codes and for many intriguing discussions. Special thanks to my parents for their love and support throughout my academic career. Most importantly, I would like to thank my wife, Laura, for her seemingly endless love and support throughout the entirety of my graduate career.

TABLE OF CONTENTS

LIST OF TABLES

LIST OF ILLUSTRATIONS

CHAPTER 1

INTRODUCTION

1.1 An Introduction to Catalysis

A catalyst is commonly defined as a substance that increases the rate of the chemical reaction without itself being consumed.[1] Catalysts achieve this by providing an alternate route for the reaction to occur; subsequently lowering the activation energy needed to form the products (**P**) from the reactants (**R**). The alternate path offered by the catalyst can be complex involving multiple intermediates (**I**) and transition states (Figure 1.1). The catalyst itself will undergo a series of transformations to generate the product, and this series must regenerate the initial form of the catalyst, thus creating a catalytic cycle. Catalysts should, therefore, be used in sub-stoichiometric amounts compared to the reactants and desired products.[2]

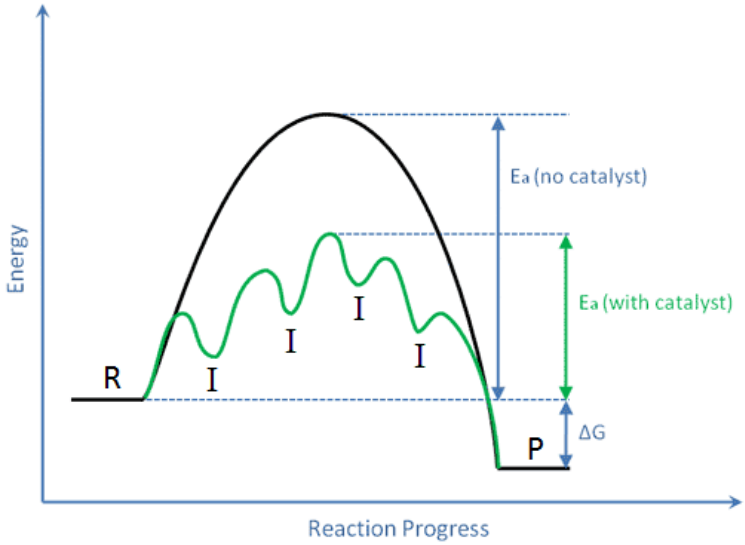

Figure 1.1. A reaction profile representing the effect of a catalyst on a reaction.

Catalysts can greatly improve the efficiency of reactions by improving reactivity and chemo-, regio-, and stereo-selectivity. The improved reactivity is a result of stabilizing one of the transition states, thus providing lower activation energy barriers ($\mathbf{E_a}$). The performance of a

catalyst is measured by the turnover number (TON), which is defined as the number of moles of substrate that a mole of catalyst can convert before becoming inactivated.[2] A second measure of performance is the turnover frequency (TOF), which describes the life cycle of the catalyst and is defined as the TON over time.[2-4] It is important to note that the catalyst only affects the reaction path kinetics ($\mathbf{E_a}$) to form the products; the overall thermodynamics ($\mathbf{\Delta G}$) are not altered by the catalyst. However, catalysts can improve the yield of the product produced. Equilibria can be shifted by changing the reaction conditions, such as temperature, pressure, and volume. Le Chatelier's principle predicts that an exothermic reaction will form higher equilibrium concentrations of the product at lower temperatures compared to concentrations at higher temperatures.[1-3] Thus, much effort has been put into developing new catalyst to perform reactions under ambient conditions which could improve the overall yield and decrease the operating cost of chemical reactions.

1.2 Transition Metals in Catalysis

Transition metals are often used in catalyst applications due to their versatility, rich chemistry, and their ability to absorb and activate small molecules on their surface. The diverse nature of transition metals comes from the ability to occupy a myriad of oxidation states, valence d-electron counts, electron configurations, various spin states, and coordination environments.[4] A critical difference between transition metals and organic elements is the ability of the former to exist in multiple oxidation states. The redox flexibility of transition metals and redox obstinacy of organic elements results in a fruitful collaboration. Transition metals can take on additional covalent bonds (*i.e.*, oxidation),[2,4-6] release new covalent bonds (*i.e.*, reduction)[2,4,5,7] and/or exchange ligands (*i.e.*, substitution)[2,4,5,8] with the resulting organic products remaining unfazed

by the transition metal's redox behavior.[2,4,5,9] Thus, transition metals make exceptional candidates for the activation and functionalization of organic molecules.

Complexes with ligands bound to transition metal centers through a carbon atom are called organometallic complexes and, for the reasons stated previously, are common in catalytic applications. The properties of the catalyst depend on the metal, ligands, substrates, and reaction conditions (*i.e.*, temperature, pressure, co-catalyst, solvent, and counter ions).[1-5] Each of these properties must be carefully selected for the application of choice when designing the appropriate catalyst.

The success of transition metals in the field of catalysis can be shown by the broad variety of applications and increasing interest in the field. Transition metals can mediate a diverse set of well-known classes of reactions involving the gain, loss, or modifications of ligands. Some of the common reactions include: ligand dissociation/association (*e.g.*, $Fe(CO)_5 \rightarrow Fe(CO)_4 + CO$),[10] oxidative addition (*e.g.*, $Ir(PR_3)_2(Cl)(CO) + H_2 \rightarrow Ir(PR_3)_2(Cl)(CO)(H)_2$),[11] reductive elimination (the microscopic reverse of oxidative addition), insertion reactions (*e.g.*, $Ni(bpy)(Et)_2 + N_2O \rightarrow Ni(bpy)(OEt)(Et) + N_2$),[12-14] and abstraction reactions (*e.g.*, $Cr(CO)_3(C_6H_6) + BuLi \rightarrow Cr(CO)_3(C_6H_5Li) + Bu$).[15] These reactions are just a few examples of the broad spectrum of organometallic reactions. Thus, the construction and fine-tuning of catalysts with transition metal centers enable many difficult chemical transformations.

1.3 Classification of Catalysts

Catalysts can be divided into two general subgroups: *homogeneous* and *heterogeneous* catalysts. A homogeneous catalyst resides in the same phase as the reagents and the medium is usually of the liquid phase. Thus, homogeneous catalysts are often discrete molecules in a suitable solvent. Heterogeneous catalysts are of a different phase from the substrate. Commonly

the catalyst will be an insoluble solid and the substrate will either be in the gas or liquid phase.[2,3] That being said, both classes of catalysts have their advantages and disadvantages.

1.3.1 Homogeneous Catalysts: Advantages and Disadvantages

Homogeneous catalysts have several advantages over heterogeneous catalysts. One major advantage is that homogeneous catalysts are much better understood at a molecular level allowing for thorough customization of the metal's inner coordination sphere resulting in the ability to tweak catalyst properties. Thus, homogeneous systems are often more reactive and selective than their heterogeneous counterparts.[2]

Conversely, homogeneous catalysts are not the most widely used for industrial applications for various reasons. Among their disadvantages is an inability to regenerate the catalyst after decomposition, which commonly occurs by an irreversible loss of a ligand or precipitation of the metal center. Thus, the cost of using homogeneous catalyst on a major scale is generally more expensive.[3] A second major disadvantage is the difficulty in separating the catalyst from the products. Homogeneous catalyst also suffer from having a lower temperature limit (approximately 250 ^{0}C) compared to the much more robust thermal stability of heterogeneous catalysts.[2]

1.3.2 Heterogeneous Catalysts: Advantages and Disadvantages

The advantages of heterogeneous catalysts are often more appealing on a large industrial scale, and thus they comprise ~ 85% of industrial catalysts.[3] Heterogeneous catalysts are often surfaces of interlinked metal atoms with no ligands attached. Some of their advantages include: low cost, ease of separation from products, high thermal stability, and the ability to regenerate (or recover) the catalyst.[3] Ligands are often the most expensive part of homogeneous catalysts and are the typical cause of the limited recycling of the catalysts. Thus, removing this

complication greatly improves the operating costs of sustaining a catalytic system.[3] Since the catalyst and reactants are of differing phases, separation from the products can often be achieved through a simple filtration processes.[3] The high thermal stability allows for completion of slow chemical reactions by increasing the temperature and/or pressure. Solid surfaces also have the possibility of containing multiple active sites resulting in the ability of the catalyst to multi-task.[2,3]

Conversely, heterogeneous catalysts often suffer from slow reaction rates due to low effective concentrations because the reaction only occurring at the interface between the solid catalysts and the gas or liquid phase reagents.[2] The catalytic conversion usually occurs on surface defects and a large surface area is needed to increase the catalyst efficiency.[3] This also leads to non-uniformity of the local structures and properties of the catalytic sites. Compared to the precise control over homogeneous catalyst, heterogeneous catalysts tend to have lower selectivity.[2] Additionally, heterogeneous catalysts suffer from catalyst poisoning. Contaminants chemically bond to the active sites effectively blocking the site from further activity, thus reducing the efficiency of the catalyst. To avoid this, most heterogeneous catalytic processes involve extra steps to prevent or reduce catalyst poisoning.[3]

While heterogeneous catalysts offer the ability to overcome unfavorable energetics, large expensive plants are often required to carry out energy intensive reactions performed under harsh conditions for high product throughput. Therefore, development of homogeneous surrogates that operate under ambient conditions is highly desirable.

1.4 Rational Catalyst Design

Currently, catalyst design is commonly engineered through experience or with an Edisonian approach (*i.e.*, trial and error). Attempts to rationally design catalysts have generally

been unsuccessful. More recently, systematic techniques through construction of ligand databases are being developed in an attempt to streamline rational catalyst design.[16-17] However, more work is required to better understand and predict ligand effects on transition metal complexes. Increasingly, improvements in rational catalyst design have been led by computational chemistry techniques, which will be discussed in detail in Chapter 2. Computational chemistry can be employed in several different ways to aid experimental collaborators in catalyst design: 1) *Explain* experimental trends and propose possible reaction pathways through the calculation of reactive intermediates and transition states.[19-21] Computational chemistry has the added bonus of being able to study unstable or air-sensitive complexes.[22] 2) *Modify* current systems to increase understanding and improve upon the current generation of catalysts.[23,24] 3) *Guide* future experimental work by employing computational chemistry in a predictive fashion.[19,25-27] The work outlined in this dissertation will feature all three uses of computational chemistry to find promising leads for future catalyst generations for small molecule activation and functionalization.

1.5 Research Motivation

Catalyst design for utilization of ubiquitous but inert molecules such as methane (CH_4) and molecular nitrogen (N_2) would have substantial impact on the chemical industry. Methane, the major component of natural gas, is an abundant resource (~26 trillion ft^3 of recoverable natural gas) in the U.S.,[28] which could provide a cleaner energy resource compared to currently used fossil fuels, reduce CO_2 emissions, and serve as a supplement for coal. Substantial natural gas reserves are domestically available; however, use is limited by the expense associated with long-distance transportation of a flammable, low boiling gas. Compression to form liquid natural gas requires substantial energy input, which limits economic feasibility and raises concerns over

safety. Although natural gas is currently used as an energy source, selective conversion of methane into a transportable liquid (such as methanol) would be an economically competitive process that would facilitate utilization of methanol on a much larger scale.[28] However, selective functionalization of methane to methanol by partial oxidation catalysis has proven to be difficult due to the inert nature of the C–H bonds with only a few reported examples.[29-34] Therefore, an application of great interest in modern catalysis research is the selective and low temperature (< 200 °C) conversion of methane (a gas) to methanol (a liquid), to facilitate the use of methane as a transportation fuel.

While the utilization of methane for industrial commodities is important, other abundant, small, but inert molecules, such as molecular nitrogen, the primary component of air, and carbon dioxide, are processed in biological systems at ambient temperature and pressure, in stark contrast to existing industrial processes, in which high drastic temperatures and pressures are needed to perform the same function. Another important industrial chemical, ammonia (NH_3), is commonly produced from the reduction of N_2 by the Haber-Bosch process (15 - 25 MPa and 300 - 550 °C). Due to these harsh conditions, designing a more facile process with transition metal catalysts is of great interest due to the demand for ammonia in fertilizer production under milder conditions.[3] Like methane, the activation of N_2 has proven to be difficult due to the kinetic and thermodynamic inertness of the molecule, arising from a very strong N≡N bond (~235 kcal/mol). Thus, a large body of catalysis research has been conducted utilizing transition metals to cleave the N≡N bond and subsequently functionalize to NH_3.

1.6 Dissertation Outline

In Chapter 3, the computer-aided design of methane activation and oxy-functionalization are explored. A proposed catalytic cycle involving two key steps was proposed: (1) C–H

activation across a metal-alkoxide bond (M–OR), and (2) regeneration of the M–OR species through an oxy-insertion step utilizing external oxidants. The C–H activation step has been extensively studied; however, the latter step is not as well understood with only limited examples. For this work, we focus on the oxy-insertion step starting with a class of compounds known to do C–H activation (*i.e.,* Pt(II) systems).[29-34] The chapter focuses on a computational Hammett analysis of a Pt(II) complex to better understand oxy-insertion into metal-carbon bonds through a concerted non-redox route akin to the Baeyer-Villiger (BV) oxidation. Chapter 4 focuses on a study to understand the influence of metal identity on organometallic BV reactions with late transition metal complexes to help guide experimentalists in an attempt to extend BV insertions to other metal systems. Chapter 5 contains a computational study exploring rare examples of late 3d metal complexes inserting oxygen into nickel–carbon bonds with nitrous oxide (N_2O) developed by Prof. Greg Hillhouse and co-workers. The oxygen atom was shown to insert with a regioselectivity similar to that of BV rearrangements. However, no mechanism was proposed by the experimentalists. Thus, we utilized computational techniques to explore various possible reaction pathways for the functionalization of nickel alkyls to nickel alkoxides. In chapter 6 we revisit the platinum complex studied in chapter 3 and computationally explore the electronic impact of the various catalytic components through an alternate mechanism. The pathway explored involves the formation of a platinum-oxo intermediate followed by aryl migration to form a phenoxide product. The results are then compared to the results outlined in chapter 3.

Chapter 7 involves a computational study on the reductive cleavage of dinitrogen (N_2). Prof. Pat Holland and co-workers recently reported a soluble iron-β-diketiminate complex that can reductively cleave the strong nitrogen-nitrogen triple bond and subsequent functionalization

to ammonia (NH_3) upon addition of an acid.[35] A density functional theory (DFT) study was performed to understand the role of cooperativity between iron-β-diketiminate fragments and potassium promoters in the N_2 activation step.

1.7 References

(1) Brown, T. L.; LeMay, H. E.; Bursten, B. E. *Chemistry: The Central Science*; Pearson Education, Inc.: New Jersey, **2006**, 577.

(2) Hartwig, J. F. *Organotransition Metal Chemistry: from Bonding to Catalysis*; University Science Books: California, **2010**, 539-549.

(3) Schlögl, R. in Handbook of Heterogeneous Catalysis, Ertl, G.; Knözinger, G.; Schüth, F.; Weitkamp, J., Eds. (Wiley-VCH, Weinheim, Germany, 2nd ed., **2008**), vol. 5, 2501–2575.

(4) Elschenbroich, C. *Organometallics* Wiley-VCH, Weinheim, Germany, 3rd ed., **2006**, 11–15.

(5) Crabtree, R. *The Organometallic Chemistry of the Transition Metals* Wiley-Interscience, **2005**, 159-180.

(6) Curtis, J.; Eisenberg, R. *J. Am. Chem. Soc.* **1985**, *107*, 3148.

(7) Bower, B. K.; Tennent, H. G. *J. Am. Chem. Soc.* **1972**, *94*, 2512.

(8) Helm, L.; Merbach, A. E. *Chem Reviews* **2005**, *105*, 1923.

(9) Miessler, G. L.; Tarr, D. A. *Inorganic Chemistry* Pearson/Prentice Hall: New Jersey, **2004**, 520-534.

(10) Snee, P. T.; Payne, C. K.; Mebane, S. D.; Dotz, K. T.; Harris, C. B. *J. Am. Chem. Soc.* **2001**, *123*, 6909.

(11) Yoneda, G.; Blake, D. M. *Inorg. Chem.* **1981**, *20*, 67.

(12) Koo, K. M.; Hillhouse, G. L.; Rheingold, A. L. *Organometallics* **1995**, *14*, 456.

(13) Matsunaga, P. T.; Hillhouse, G. L.; Rheingold, A. L. *J. Am. Chem. Soc.* **1993**, *115*, 2075.

(14) Matsunaga, P. T.; Mavropoulos, J. C.; Hillhouse, G. L. *Polyhedron* **1995**, *14*, 175.

(15) Lai, W.; Li, C.; Chen, H.; Shaik, S. *Angew. Chem. Int. Ed.*, **2012**, *51*, 5556.

(16) Houk, K. N.; Cheong, P. H.Y. *Nature*, **2008**, *455*, 309.

(17) Hoveyda, A. H.; Hird, A. W.; Kacprzynski, M. A. *Chem. Commun.* **2004**, 1799.

(18) De Vries, J. G.; Lefort, L. *Chem. Eur. J.* **2006**, *12*, 4722.

(19) Figg, T. M.; Cundari, T. R. *Organometallics* **2012**, *31*, 12920.

(20) Figg, T. M.; Holland, P. L.; Cundari, T. R. *Inorg. Chem.* **2012**, *51*, 7546.

(21) McKeown, B. A.; Gonzalez, H. E.; Friedfeld, M. R.; Gunnoe, T. B.; Cundari, T. R.; Sabat, M. *J. Am. Chem. Soc.* **2011**, *133*, 19131.

(22) Yu, Y; Sadique, A. R.; Smith, J. M.; Dugan, T. R.; Cundari, T. R.; Brennessel, W. W.; Flaschenriem, C .J.; Bill, E.; Holland, P. L. *J. Am. Chem. Soc.* **2008**, *130*, 6624.

(23) Figg, T. M.; Cundari, T. R.; Gunnoe, T. B. *Organometallics*, **2011**, *30*, 3779.

(24) DeYonker, N. J.; Foley, N. A.; Cundari, T. R.; Gunnoe, T. B.; Petersen, J. L. *Organometallics* **2007**, *26*, 6604.

(25) Figg, T. M.; Webb, J. R.; Gunnoe, T. B.; Cundar, T. R. *J. Am. Chem. Soc.* **2012**, *134*, 2332.

(26) Morello, G. R.; Cundari, T. R.; Gunnoe, T. B. *J. Organomet. Chem.* **2012**, *697*, 15.

(27) Prince, B. P.; Cundari, T. R. *Organometallics* **2012**, *31*, 1042.

(28) Olah, G. A. *Angew. Chem. Int. Ed.* **2005**, *44*, 2636.

(29) Brown, S. N.; Mayer, J. M. *J. Am. Chem. Soc.* **1996**, *118*, 12119.

(30) Brown, S. N.; Mayer, J. M. *Organometallics* **1995**, *14*, 2951.

(31) Brown, S. N.; Myers, A. W.; Fulton, J. R.; Mayer, J. M. *Organometallics* **1998**, *17*, 3364.

(32) Conley, B. L.; Ganesh, S. K.; Gonzales, J. M.; Tenn, W. J., I; Young, K. J. H.; Oxgaard, J.; Goddard, W. A., I; Periana, R. A. *J. Am. Chem. Soc.* **2006**, *128*, 9018.

(33) Gonzales, J. M.; R., D., Jr.; Periana, R. A; Goddard, W. A., III; Oxgaard, J. *J. Am. Chem. Soc.* **2007**, *129*, 15794.

(34) Bischof, S. M.; Cheng, M.-J.; Nielsen, R. J.; Gunnoe, T. B.; Goddard, W. A., III; Periana, R. A. *Organometallics* **2011**, *30*, 2079.

(35) Rodriguez, M. M.; Bill, E.; Brennessel, W. W.; Holland, P. L. *Science* **2011**, *334*, 780.

CHAPTER 2

COMPUTATIONAL METHODS

2.1 The Schrödinger Equation

Computational chemistry has flourished in recent years due to incredible strides in computing power, storage and user-friendly software development. Computational chemistry provides a powerful tool to aid rational catalyst design with the advent of various computational methodologies to determine the electronic structure and a myriad of chemical and physical properties.[1] The ultimate goal in most computational methods is the approximate solution to the non-relativistic, time-independent Schrödinger wave equation.[2-5] The Schrödinger equation in its simplest representation is:

$$\hat{H}\Psi = E\Psi \tag{2.1}$$

where Ψ is the wave function, $\hat{H}$ is the Hamiltonian operator, and E represents the eigenvalue. The Hamiltonian operator consists of five terms:

$$\hat{H} = \hat{T}_e + \hat{T}_N + \hat{T}_{eN} + \hat{T}_{NN} + \hat{T}_{ee} \tag{2.2}$$

the electronic ($\hat{T}_e$) and nuclear ($\hat{T}_N$) kinetic energy operators as well as potential energy operators that account for electron-nuclear ($\hat{T}_{eN}$), nuclear-nuclear ($\hat{T}_{NN}$), and electron-electron ($\hat{T}_{ee}$) interactions.

It is impractical to attempt to solve the Schrödinger equation in its entirety for systems with more than one electron. Therefore, approximations are made to reduce the computational cost associated with solving the Schrödinger equation. Under normal physical conditions, the nuclei are moving much slower than the associated electrons. Also, note that protons and neutrons are approximately 1800 times larger than electrons. Hence, for practical purposes, electronic relaxation with respect to nuclear motion is instantaneous. The Born-Oppenheimer

approximation decouples these two motions and assumes fixed nuclear positions.[6,7] That is, the Hamiltonian operator given in equation 2.2 can be greatly simplified. The nuclear kinetic energy term is thus approximated to be independent of the electrons, the electron-nuclear term is eliminated and the nuclear-nuclear term becomes a constant for a given geometry. Even with the various approximations, the Schrödinger equation has never been completely solved for anything other than one electron systems (H, He^+, *etc.*).[8]

Electronic structure methods are divided into two major categories: *ab initio* and semi-empirical methods. Computations that are derived directly from theoretical principles, with no inclusion of experimental data fall under the *ab initio* category and methods that are parameterized by experimental data are termed semi-empirical. Higher quality methods afford better results; however, the computational cost scales exponentially with the number of atoms.[1,9] Some prominent *ab initio* methods and their respective scaling factor (N^m), were N is the number of basis functions utilized which scales exponentially by m affecting the computational cost of the method being used: Hartree Fock (HF)[11,12] (N^{3-4}), many body perturbation theory (MBPT)[13,14] (N^{5-6}), configuration interaction (CI)[15] (N^5), and coupled cluster (CC)[16-18] (N^6). Thus, the more complex of these methods are only feasible for molecules containing 20 or fewer atoms.[10] The increase in computational cost is due to the correlation term requiring multi-determinate wavefunctions to be calculated, as opposed to a single Slater[19] determinant.

While ensuring the correct level of theory is utilized for the chemical problem at hand, there must also be a tradeoff between speed and accuracy when computing large systems that are common in organometallic systems. Also, when surveying a variety of isomers and possible catalytic pathways faster electronic structure calculations are desired. The most widespread approach is density functional theory (DFT),[20] which models the electron density as a function of

the ground state geometry as opposed to the wavefunction based methods described previously.[1,9]

2.2 Density Functional Theory

DFT is a quantum mechanical method used to investigate the electronic structure of many-body systems and is commonly employed in gas phase and solid state calculations. Unlike wavefunction based methods, the properties of a many-electron system are determined by using functionals, *i.e.* functions of another function, of the spatially dependent electron density. DFT methodology is computationally efficient due to the number of variables remaining constant as the electron density is treated as a single-body problem.[1,9,21] DFT is much simpler compared to many-body wavefunction methods where each electron contributes three variables. Thus, DFT is typically favored over *ab initio* calculations for catalyst design due to the reduced computational cost while maintaining a similar accuracy.

The theoretical framework for DFT is based on three concepts: the Thomas-Fermi model,[22,23] the Hohenberg-Kohn theorem[24] and the Kohn-Sham equations.[25] Modern day DFT, also called Kohn-Sham DFT (KS-DFT), involves the construction of a fictitious non-interacting system in such a way that its density is the same as a system with interacting electrons. In other words, the many-body interactions in a static external potential present in a model system is now replaced by non-interacting electrons in an effective potential, the Kohn-Sham potential. The total energy of an electronic structure calculation is expressed as a functional ($E[\rho]$) of the electron density (ρ) that takes the general form:

$$E[\rho] = T_s[\rho] + \int dr\, v_{ext}(r)\rho(r) + V_H[\rho] + E_{xc}[\rho] \qquad (2.3)$$

The first term, T_s, represents the Kohn-Sham electronic kinetic energy approximation. The next term, v_{ext}, represents the external potential of coulombic interactions between the nuclei and

electrons and is expressed in spherical coordinates (r). The third term, V_H, is the Hartree or Coulomb energy for the repulsion between the electron density and itself. The fourth term, E_{xc}, is the exchange-correlation functional, which accounts for electron-electron interactions. The exchange-correlation functional accounts for the correlated motion of two electrons with parallel spins and the tendency of electrons to "avoid" each other.

The major problem with DFT arises from the inadequate description of the functionals for exchange and correlation, which are not known except for in the free electron gas. However, approximations exist that permit the calculation of certain physical quantities quite accurately.[26] Over the years many functionals have appeared based on KS-DFT.[28,29] The hierarchy of DFT functionals is classically represented in Perdew's "Jacob's ladder", Figure 2.1.[27] The density functionals primarily differ in their approximations to the exact exchange and correlation energy functional (E_{xc}). As one ascends the ladder, the better the exchange-correlation functional is described; however, computational cost is also increased.

The first rung contains the local density approximation (LDA) and local spin density approximation (LSDA) functionals[30] in which the $E_{xc}[\rho]$ value depends solely on the electronic density at each point in space. This approximation is, in most cases, suitable only for the uniform electron gas models (UEG); however, LDA has been shown to give good results for some transition metal properties in the solid state. The second rung consists of generalized gradient approximation (GGA) functionals.[31-36] These functionals are local functionals much like the LSDA functionals; however, the gradient of the electron density (*i.e.*, the first derivative of the electronic density) is also accounted for. Some examples include: BP86,[31,32] BLYP[32,33] and PBE[35,36] functionals. GGA functionals are commonly employed in calculations with periodic boundary conditions, such as those utilized in solid state codes. Both LSDA and GGA methods

overestimate molecular stability and bond strengths, while HF methods typically underestimate.[1] Rung 3 consists of the meta-generalized gradient approximation (meta-GGA) functionals.

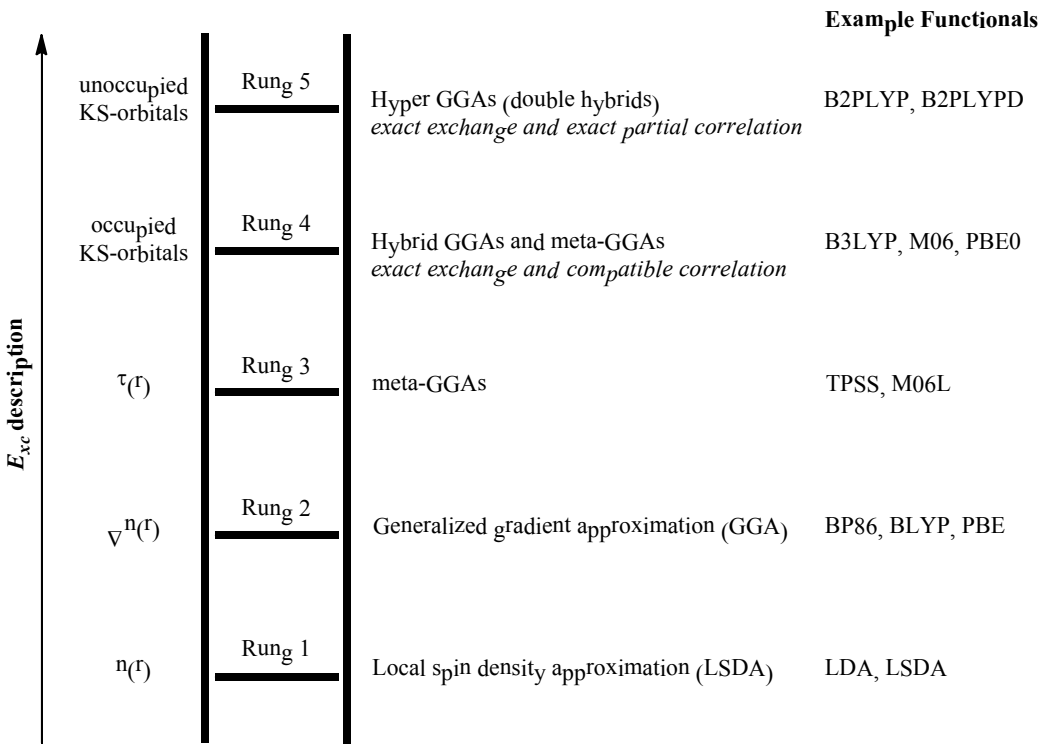

Figure 2.1. Perdew's Jacobs ladder of DFT functionals.

Meta-GGA functionals include a dependence of the kinetic energy density (*i.e.*, on the laplacian of the orbitals). Some examples of meta-GGA functionals include: TPSS[37] and M06L[38] functionals. The 4th rung consists of the hybrid functionals and is the method of choice for the entirety of this dissertation. Hybrid functionals incorporate a portion of exact exchange from Hartree-Fock theory. The $E_{xc}[\rho]$ is expressed in terms of Kohn-Sham orbitals rather than electronic density. Examples of hybrid functionals include: B3LYP,[33,39] M06-2X,[40] and PBE0[41] functionals. The B3LYP functional is utilized for the majority of the work outlined in this dissertation. B3LYP is composed of the Becke 88 exchange functional and the correlation functional of Lee, Yang and Parr. The final Rung, consists of double hybrid functionals (*e.g.*,

B2PLYP[42]), which incorporate a certain amount of HF exchange and MP2 correlation. The convergence of a double hybrid can be more difficult than with simpler functionals and the computational time is approximately twice that of a B3LYP calculation. Thus, double hybrid calculations are less commonly used.

2.2.1 Limitations of Density Functional Theory

The failings of DFT are well documented and are still problematic within the current generation of functionals. Furthermore, DFT also lacks a way to systematically converge on the exact solution unlike wavefunction based methodologies.[9,21] These issues arise from the inadequate treatment of electron self-interaction and the exchange correlation functionals. Energy states with different spin multiplicities, excited states in charge transfer systems and odd charged electron systems are particularly dependent on the DFT functional utilized.[9,21,43] The inclusion of HF exchange energy in hybrid functionals has been found to improve the modeling of such systems that favor high spin configurations. Another problematic issue is the inability to describe weak to medium-range interactions such as van der Waals forces.[9,21,43]

Dispersion forces are more pronounced in large molecules, such as the organometallic complexes commonly used in catalysts. Several approaches to overcome the inability to describe dispersion have been carried out over the years. Truhlar and Zhao have empirically fitted functionals designed to better describe van der Waals forces.[38,40] These functionals are called the Minnesota family of functionals (M06, M06-L, M06-2X, *etc.*) and are commonly employed in catalyst design. Grimme and coworkers have implemented and parameterized a correction to the energy to account for weak interactions. This correction is denoted by a "-D" on the end of functional abbreviations (*e.g.*, B3LYP-D).[44,45]

In this dissertation, hybrid functionals are utilized due to their proven utility with similar organometallic reactions. Since DFT has no systematic way for improvement, extensive calibrations were carried out testing various functionals and basis sets to ensure the level of theory utilized was adequate.

2.3 References

(1) Jensen, F. *Introduction to Computational Chemistry*; Wiley: England, **2007**.

(2) Schrödinger, E., *Phys. Rev.* **1926**, *28*, 1049.

(3) Schrödinger, *E. Ann. Phys.* **1926**, *79*, 489.

(4) Schrödinger, E. *Ann. Phys.* **1926**, *80*, 437.

(5) Schrödinger, E. *Die Naturwißenscheften* **1926**, *14*, 664.

(6) Born, M.; Oppenheimer, R. *Ann. Phys.* **1927**, *84*, 457.

(7) Eckart, C *Physical Review* **1935**, *46*, 383.

(8) Harvey, J. N. *Annu. Rep. Prog. Chem., Sect. C* **2006**, *102*, 203.

(9) Cramer, C. J. *Essentials of Computational Chemistry*; Wiley: England, **2002**.

(10) Guest, M. F.; Sherwood, P.; Nichols, J. A. *Massive Parallelism: The Hardware for Computational Chemistry?*; Kluwer: Tokyo, Japan, **1997**.

(11) Hartree, D. R. *Proc. Camb. Phil. Soc.* **1928**, *24*, 89.

(12) Fock, V. *Zeits. F. Physik* **1930**, *61*,126.

(13) Møller, C.; Plesset, M. S. *Phys. Rev.* **1934**, *46*, 618.

(14) Head-Gordon, M.; Pople, J. A.; Frisch, M. J. *Chem. Phys. Lett.* **1988**, *153*, 503.

(15) Pople, J. A.; Seeger, R.; Krishnan, R. *Int. J. Quantum Chem.* **1977**, *Y-11*, 149.

(16) Cizek, J. *J. Chem. Phys.* **1966**, *45*, 4256.

(17) Barlett, R. J.; Purvis III, G. D. *Int. J. Quantum Chem.* **1978**, *14*, 561.

(18) Pople, J. A.; Krishnan, R.; Schlegel, H. B.; Binkley, J. S. *Int. J. Quantum Chem.* **1978**, *14*, 545.

(19) Slater, J. C. *Phys. Rev.* **1951**, *81*, 385.

(20) Parr, R. G.; Yang, W. *Density Functional Theory of Atoms and Molecules*; Oxford University Press: New York, **1989**.

(21) Koch, W.; Holthausen, M. C. *A Chemist's Guide to Density Functional Theory*; Wiley-VCH: Weinheim, **2001**.

(22) Fermi, E. *Z. Phys.* **1928**, *48*, 73.

(23) Thomas, L. *Proc. Camb. Phil. Soc.* **1927**, *23*, 542.

(24) Hohenberg, P.; Kohn, W. *Phys. Rev.* **1964**, *136*, B864.

(25) Kohn, W.; Sham, L. J. *Phys. Rev.* **1965**, *140*, A1133.

(26) Ernzerhof, M.; Perdew, J.; Burke, K. *Topics in Chem.* **1996**, *180*, 1.

(27) Perdew, J. P.; Schmidt, K. AIP Conference Procceedings **2001**, *577.1*.

(28) (a) Sousa, S. F.; Fernandes, P. A.; Ramos, M. J. *J. Phys. Chem. A* **2007**, *111*, 10439-10452. (b) Zhao, Y.; Truhlar, D. G. *Acc. Chem. Res.* **2008**, *41*, 157. (c) Quintal, M. M.; Karton, A.; Iron, M. A.; Boese, A. D.; Martin J. M. L. *J. Phys. Chem. A* **2006,** *110,* 709 and references therein.

(29) (a) Buhl, M.; Kabrede, H. *J. Chem. Theory Comput.* **2006**, *2*, 1282–1290. (b) Waller, M. P.; Braun, H.; Hojdis, N.; Buhl, M. *J. Chem. Theory Comput.* **2007***, 3*, 2234-2242. (c) Buhl, M.; Reimann, C.; Pantazis, D. A.; Bredow, T.; Neese, F. *J. Chem. Theory Comput.* **2008***, 4*, 1449-1459.

(30) Slater, J. C. *Phys. Rev.* **1951**, *81*, 385.

(31) Perdew, J. P. *Phys. Rev., B.* **1986**, *33*, 8822.

(32) Becke, A. D. *Phys. Rev., B* **1988**, *38*, 3098.

(33) Lee, C.; Yang, W.; Parr, R. G. *Phys. Rev. B.* **1988**, *37*, 785.

(34) Miehlich, B.; Savin, A.; Stoll, H.; Preuss, H. *Chem. Phys. Lett.* **1989**, *157*, 200.

(35) Perdew, J. P.; Burke, K.; Ernzerhof, M. *Phys. Rev. Lett.* **1996**, *77*, 3865.

(36) Perdew, J. P.; Burke, K.; Ernzerhof, M. *Phys. Rev. Lett.* **1997**, *78*, 1396.

(37) Tao, J. M.; Perdew, J. P.; Staroverov, V. N.; Scuseria, G. E. *Phys. Rev. Lett.* **2003**, *91*, 146401.

(38) Zhao, Y.; Truhlar, D. G. *J. Chem. Phys.* **2006**, *125*.

(39) Becke, A. D. *J. Chem. Phys.* **1993**, *98*, 5648.

(40) Zhao, Y.; Truhlar, D. G. *Theor. Chem. Acc.* **2008**, *120*, 215.

(41) Adamo, C.; Barone, V. *J. Chem. Phys.* **1999**, *110*, 6158.

(42) Schwabe, T; Grimme, S. **2007**, *9*, 3397.

(43) Cohen, A. J.; Mori-Sanchez, P.; Yang, W. *Science* **2008**, *321*, 792.

(44) Grimme, S. *J. Comp. Chem.* **2004**, *25*, 1463.

(45) Grimme, S. *J. Comp. Chem.* **2006**, *27*, 1787.

CHAPTER 3

NON-REDOX OXY-INSERTION VIA ORGANOMETALLIC BAEYER-VILLIGER TRANSFORMATION: A COMPUTATIONAL HAMMETT STUDY OF PT(II) COMPLEXES*

3.1 Introduction

The petrochemical industry is predominantly based on the transformation of a handful of hydrocarbon feedstocks (*e.g.,* benzene, ethylene, propylene, butenes, toluene, methane and xylenes) to higher value materials, and many of these substrates are converted to oxygenated products.[1,2] As a result, catalysts for the *selective* partial oxidation of hydrocarbons could have substantial impact. For example, the selective and low temperature (≤ 200 ºC) functionalization of methane into methanol could facilitate the utilization of natural gas as a transportation fuel and as a precursor to a variety of chemical reagents as well as potential use of methanol as a substrate for fuel cells.[3,4] Therefore, an economically viable catalytic cycle for partial oxidation of methane to methanol (MTM) has been of interest.[1,5-10] Although heterogeneous catalysts for oxidative methane coupling and partial oxidation of methane have been reported, these systems generally provide yields < 25% for coupling and < 5% for partial oxidation.[11] Homogeneous catalysts, or single-site heterogeneous systems based on homogeneous systems, offer opportunities to fine-tune catalysts for enhanced selectivity.

The two key steps in a catalytic cycle for the MTM transformation are methane C–H activation and C–O bond formation. The discovery that Pt(II) salts catalyze the selective functionalization of methane, the Shilov system, sparked substantial interest in the potential of late transition metals as catalysts for MTM.[12]

---

* This chapter is presented in its entirety from T. M. Figg, T. B. Gunnoe, and T. R. Cundari "Non-Redox Oxy-insertion Via Organometallic Baeyer-Villiger Transformation: A Computational Hammett Study of Pt(II) Complexes" Organometallics, 2011, 30, 3779 with permission from the American Chemical Society.

In this system, studies suggest an initial Pt(II)-mediated C–H activation followed by oxidation to Pt(IV), which mediates the C–O bond formation step via a reductive nucleophilic addition of OH_n to an electrophilic methyl ligand. Despite substantial progress with this class of complexes,[6,13-15] including a highly active and selective Pt(II) complex supported by a bipyrimidine ligand,[16] a commercially viable catalyst has yet to be discovered. A primary limitation of electrophilic late transition metal catalysts, including those based upon Hg and Au, is the reaction of the catalyst with oxidant.[5,8,17-21]

A pathway that provides an alternative to the Shilov-type systems is shown in Figure 3.1. In this cycle, hydrocarbon C–H activation by a nucleophilic and basic metal alkoxide ultimately generates free alcohol and a new metal-hydrocarbyl moiety. Subsequent insertion of an oxygen atom into the M–R bond regenerates the metal alkoxide. Relevant to the C–H activation sequence, in 2004 we reported intermolecular H_2 addition across a Ru(II)–amido unit and *intra*molecular C–H activation with this same system.[22] Subsequently, we reported benzene C–H activation by Ru(II)–hydroxide and –anilido complexes at the same time that Periana, Goddard *et al.* reported benzene C–H activation by an Ir(III)–methoxide system.[22-32]

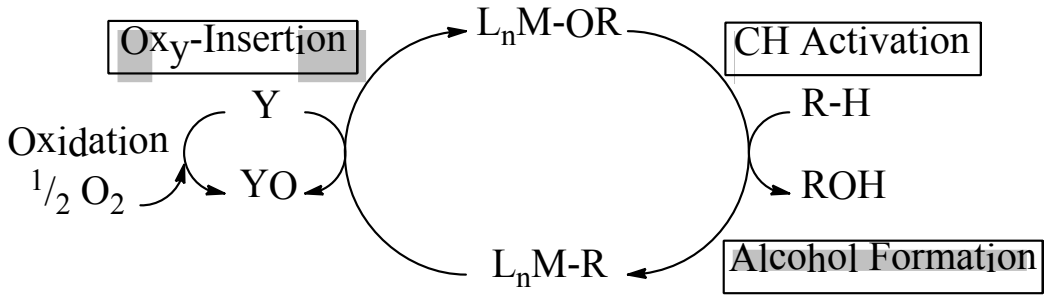

Figure 3.1. Proposed cycle for methane to methanol catalysis (R – methyl, YO = oxidant, Y = leaving group, L_nM = catalyst).

Several research groups have utilized experimental and computational methods to probe the kinetics and thermodynamics of C–H activation by middle-late transition metal-heteroatom bonded complexes, including alkoxides (L_nM–OR).[23,24,27,28,31-41]

While the 1,2-addition of C–H bonds across M–OR bonds has been observed for Ru(II), Ir(III) and Rh(I) systems, examples of oxy insertion into M–R bonds are rare. Over a decade ago, Brown and Mayer reported a well-defined thermal insertion of an oxo ligand into a Re–Ph bond with a Re(VII) system.[42] The electrophilic character of the oxo ligand, which is likely enhanced by strong oxo-to-Re π-donation, was suggested as a key feature of this unusual transformation. Recently, Periana, Goddard *et al.* reported that methylrheniumtrioxide (MTO, $MeReO_3$) reacts in water with a variety of oxidants to generate methanol (Figure 3.2).[43,44]

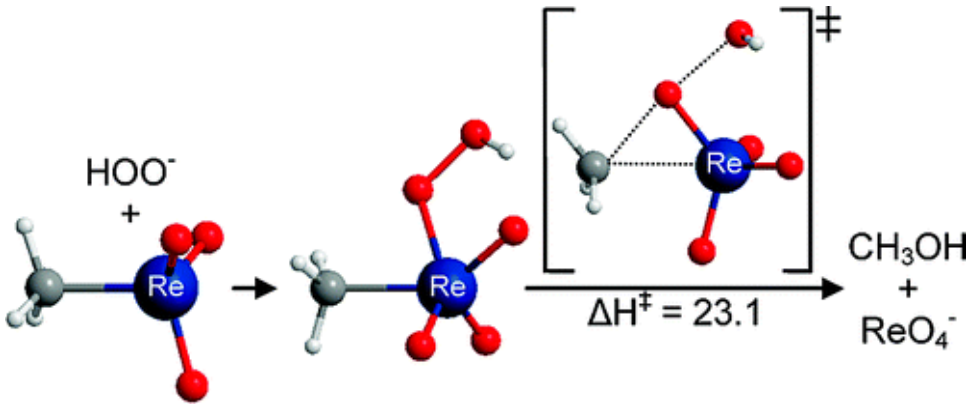

Figure 3.2. Baeyer-Villiger transition state for oxy insertion into Re–Me bond of methyl rheniumtrioxide.

For several of the oxidants,combined experimental and computational studies suggest that the mechanism of this transformation involves coordination of the oxidant followed by oxygen insertion into the Re–Me bond via a "Baeyer-Villiger" (BV) type pathway. Consistent with the proposed BV pathway, $(Ar)ReO_3$ (Ar = aryl) reacts more rapidly than $MeReO_3$.[45] This seminal discovery suggests that metal-mediated C–O bond formation need not involve formation of a

bona fide metal–oxo (M=O) intermediate.[42,46-48] This is potentially important since metal–oxo bonds are typically strong and can be unreactive. In addition, for late transition metals the formation of oxo complexes starting from low valent systems that may be capable of activating C-H bonds (*e.g.*, Pt(II), Ir(I), Rh(I)) is rare.[49-53] Hence, a route for the M–R + YO → M–OR + Y conversion that does not involve M=O formation is potentially promising within the context of MTM catalysis.

Given the limited studies of metal-mediated BV processes that involve oxygen insertion into M–R bonds, we believe that there are two primary and fundamental issues to be addressed: (1) To what extent does the analogy to the organic BV reaction apply *vis-à-vis* expected similarities in reactivity trends? (2) Can BV-type oxy-insertion reactions be extended to other metal systems (especially those that might be capable of C–H activation following oxy-insertion)? With these goals in mind, we sought to augment our understanding of the "organometallic" BV reaction by probing the influence of the metal (M), oxidant (YO), transfer group (R) and supporting ligand (L_n) upon the non-redox insertion of oxygen into metal-carbon bonds (eq 3.1).

$$L_nM^q(R) + OY \rightarrow L_nM^q(OR) + Y \qquad (3.1)$$

Since the ultimate utility of the organometallic BV reaction for hydrocarbon functionalization will depend on coupling this transformation with C–H activation, one of the most pressing issues for MTM catalysis is to determine the importance of metal identity and oxidation state for the oxy-insertion transformation. To our knowledge, there are no reports of studying this reaction outside of the MTO system. Thus, we have begun to explore, experimentally and computationally, the organometallic BV reaction with low valent systems known to activate C–H bonds. Given the ability of Pt(II) systems to activate the C–H bonds of

hydrocarbons,[15,33,36,54-57] we selected Pt(II) systems as an entry point into a broad-based combined experimental and computational study. Since we have reported recently that $[(^{t}bpy)Pt(R)]^{+}$ (^{t}bpy = 4,4'-di-*tert*-butyl-bipyridyl; R = aryl or alkyl) systems activate aromatic C–H bonds,[58] this ligand framework was selected as a starting point.

Herein, we report the results of a computational Hammett study of organometallic BV transformations focusing on d^8-Pt(II) systems $[(^{X}bpy)Pt(R)(OY)]^{+}$ (R = *p*-X-C_6H_4; Y = 4-X-pyridine; ^{X}bpy = 4,4'-X-bpy; X = NO_2, H, NMe_2). Since the $[(^{X}bpy)Pt(R)(OY)]^{+}$ motif offers the capability of placing an electron withdrawing/donating group (EWG/EDG) in the *para* positions of the migrating group (R), 4 position of the oxidant (YO), and 4/4' positions of the bpy ligand, this system allowed a thorough assessment of structure/activity relationships for oxy-insertion using computational modeling. Our primary goals were to: (1) compare the electronic effects predicted by computational studies of the Pt(II) systems versus the organic BV reaction (using previously reported studies), and (2) compare the calculated pathways for oxy-insertion for the Pt(II) complexes and the previously reported $MeReO_3$ system.[43-45] Addressing the latter goal would provide an entry point to begin assessing the viability of the organometallic BV reaction with different classes of metal complexes (in this case, an electrophilic late transition metal).

3.2 Computational Methods

Unless stated otherwise, a standard level of theory – B3LYP[59-61]/CEP-31G(d)[62,63] – was utilized within the Gaussian 09 package[64] to facilitate comparison among the various complexes. The current approach, which has been used in numerous computational studies by our group,[22,23,35,39,65-70] was calibrated versus computations reported by Periana *et al.*[44] for the study of BV oxidations of ReO_3Me. For example, the Baeyer-Villiger transition state ($BV^{‡}$) for $[O_3ReMe(OOH)]^{-}$ → $BV^{‡}$ → $[O_3Re(OH)(OMe)]^{-}$ is calculated to be 27.1 kcal/mol using a

B3LYP/CEP-31G(d) level of theory, which compares to 23.3 kcal/mol (gas phase).[44] Additionally, calibration of this standard double-zeta-plus-polarization (triple zeta for transition metals) valence basis sets (VBSs) against larger triple-zeta-plus-polarization VBSs (CEP-121G(d)) did not lead to appreciable differences in calculated energetics despite larger resource demands for the latter.

Calculated free energies of activation quoted below (1 atm, 298.15 K) are for the respective $BV^{‡}$ relative to the "adduct" (or metallo-Criegee intermediate (MCI)), $[(bpy)Pt^{II}(Ph)(PyO)]^{+}$, or its *para*-substituted derivatives. Test calculations in a polar solvent (THF solvent, CPCM continuum solvation model)[71,72] did not substantially affect the energetics – thermodynamics and kinetics – of model metallo-BV transformations. The present results incorporating solvent echo those seen previously for MTO oxy-insertion modeling whereby incorporation of continuum solvent effects had only a minimal impact on the barrier to oxy-insertion.[44]

3.3 Results and Discussion

Since our goal is to focus on the impact of the various catalyst components on the energetics of the oxy insertion step rather than an overall transformation, we have not calculated the energetics of coordination of "YO" to the $[(bpy)Pt(Ar)]^{+}$ systems. The $[(bpy)Pt(Ph)(OPy)]^{+}$ (OPy = pyridine-*N*-oxide) complex was defined as the baseline metallo-Criegee intermediate for the present computational Hammett studies. The influence of placing NMe_2 [electron donating group (EDG)] and NO_2 [electron withdrawing group (EWG)] groups in the *para* position of the phenyl ligand, the 4-position of the pyridine of pyridine-*N*-oxide and the 4/4' positions of the bipyridyl ligand was probed. The NMe_2 and NO_2 substituents, with Hammett sigma values (σ_p) for NMe_2 and NO_2 of -0.83 and +0.78, allow us to test two extreme electronic situations for the

three catalyst variables: ancillary ligand, migrating group and leaving group of the oxygen delivery reagent.[73]

3.3.1 Hammett Studies of the Migrating Aryl Group (R)

The calculated pathways are displayed in Figure 3.3 from the MCI to the alkoxide product via a non-redox, BV-type transition state. The activation barrier for conversion of $[(bpy)Pt(Ph)(OPy)]^+$ to $[(bpy)Pt(OPh)(Py)]^+$ by a BV type pathway (Figure 3.3) was calculated to be 42.1 kcal/mol. The geometry of the calculated BV transition state is given in Figure 3.4.

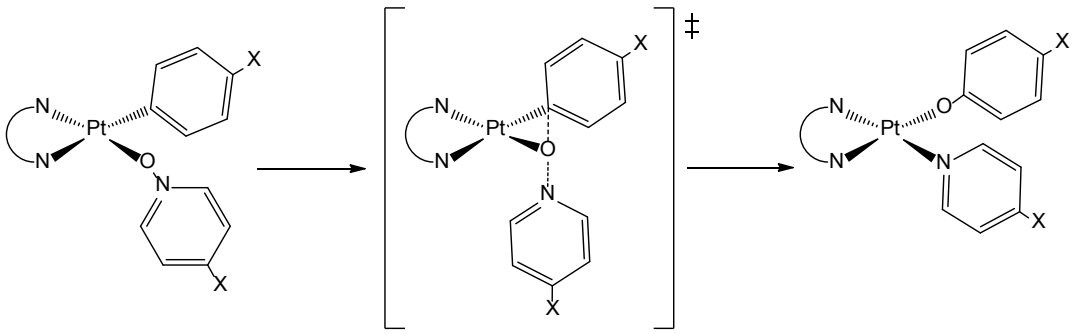

Figure 3.3. Calculated BV pathways from the metallo-Criegee intermediate (MCI) to the metal-alkoxide product a BV-type transition state (X = H, NMe_2, or NO_2).

The calculated transition states for systems in which electron-withdrawing NO_2 and electron-donating NMe_2 have been substituted in the phenyl *para* position. The orientations of the NO_2 and NMe_2 groups in the calculated transition states enable π-interaction with the aryl substituent. The transition states were confirmed by the presence of a single imaginary frequency, typically ~500i cm^{-1}, which primarily corresponds to expansion/compression of the O_Y-Pt-C_{Ph} angle. Compared to the parent system (Figure 3.4) placement of a *p*-NO_2 group in the phenyl ring results in minimal change in the bonds surrounding the core of the oxy insertion TS.

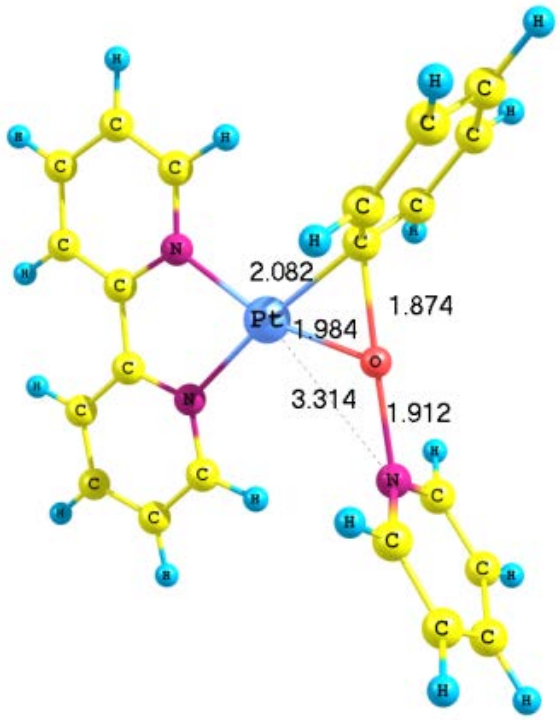

Figure 3.4. Geometry of calculated Baeyer-Villiger transition state for "parent" complex $[(bpy)Pt(Ph)(PyO)]^+$ (bond lengths in Å).

The free energy of activation for the BV insertion of oxygen into the Pt–aryl bond is calculated to *increase* by 3.5 kcal/mol from 42.1 to 45.6 kcal/mol upon placement of the NO_2 group on the migrating phenyl. Introduction of the NMe_2 group into the *para* position of the phenyl migrating group *lowers* the free energy to the BV transition state to 33.7 kcal/mol, a decrease of 8.5 kcal/mol from the 42.1 kcal/mol calculated for $[(bpy)Pt(Ph)(OPy)]^+$. The larger energetic impact of NMe_2 versus NO_2 correlates with the larger geometric perturbation of this substituent in the BV transition state as discussed above. As in the organic reaction,[74] the electronic demands of the migrating group are calculated to have a substantial impact on the barriers to organometallic Baeyer-Villiger oxy-insertion. *This points to a potential limitation of the organometallic BV reaction, since, unlike the oxidant or the ancillary ligands of the catalyst, the migrating group is dictated by the hydrocarbon substrate and cannot be used to optimize the*

rate of reaction. The calculated $\Delta\Delta G_R^{\ddagger}$ between the NO_2 and NMe_2 systems is 11.9 kcal/mol ($\%\Delta G_R^{\ddagger} \approx 30\%$) {$\%\Delta G$ is defined as (maximum barrier – minimum barrier)/average barrier}.

3.3.2 Hammett Studies of the Oxidant

The same EWG (NO_2) and EDG (NMe_2) were attached to the 4-position of pyridine-*N*-oxide, and the energetics for the migration step of organometallic BV were calculated for $[(bpy)Pt(Ph)(OY)]^+$ (Y = pyridine, 4-NMe_2-pyridine or 4-NO_2-pyridine). The BV barrier for 4-NO_2-PyO oxidant was calculated to *decrease* to 40.0 kcal/mol (down by 2.1 kcal/mol versus $[(bpy)Pt(Ph)(OPy)]^+$). The 4-NMe_2-PyO free energy barrier *increases* to 44.0 kcal/mol (up by ~2.0 kcal/mol). The calculated $\Delta\Delta G^{\ddagger}$ from the NMe_2 to NO_2 systems is 4.0 kcal/mol. Thus, the impact of migratory group modification has a more substantial impact than the leaving group with respect to changes in the BV free energy barriers. Structural alterations in the BV transition states upon changing the oxidant substituents is discussed below.

3.3.3 Hammett Studies of the Ligand

A computational Hammett study was conducted to determine the extent to which substitution of the 4 and 4' positions of the bpy ligand with EDGs/EWGs impact the free energy of activation for the oxy-insertion step. Transition metal complexes that possess these substituted bpy ligands have been reported.[75] Calculated transition state geometries are discussed below within the context of establishing catalyst structure-property relationships between calculated TS bond lengths and free energies of activation (*vide infra*).

Incorporation of the 4,4'-NO_2-bpy results in a calculated BV free energy barrier of 41.7 kcal/mol versus 42.1 kcal/mol for $[(bpy)Pt(Ph)(OPy)]^+$. For 4,4'-NMe_2-bpy, the calculated $\Delta G^{\ddagger}$ is 42.0 kcal/mol for the BV reaction. The calculated changes in free energy barriers are thus negligible versus $[(bpy)Pt(Ph)(PyO)]^+$ between the 4,4' substituted and parent bpy systems. The

calculated $\Delta\Delta G_{bpy}^{\ddagger}$ for the NO_2- and NMe_2-substituted bpy ligands is only 0.4 kcal/mol. The results imply that realizing more reasonable oxy-insertion barriers by fine tuning the electronics of the ligand environment may be difficult, and that more drastic modifications to the supporting ligation may be needed to substantially modulate activity for these and related d^8 catalysts. Of course, an important caveat is that the calculations take into account only the energetics of the oxy insertion step and not the potential role of coordination of the oxidant, which might be more heavily influence by the donor ability of the ancillary ligands.

3.3.4 Combining Multiple Substituents

Another series of calculations explored the influence of optimizing the electronic structure for the BV reaction by modifying *both* the migrating aryl and oxidant. To do so, a *p*-EDG (NMe_2) was placed on the migrating phenyl group *and* an EWG (NO_2) was added to the 4-position of the oxidant. The calculated barrier of the organometallic BV for this system was found to be 32.2 kcal/mol, which is *ca.* 1.5 kcal/mol below the BV barrier when R = *p*-NMe_2-C_6H_4 and Y = PyO.

3.3.5 Comparison to the Classical BV System

The classic organic Baeyer-Villiger mechanism is generally considered to occur by a two-step process. Addition of the oxidant to the carbonyl forms the "Criegee intermediate," which is akin to the $L_nM(R)(OY)$ adducts (metallo-Criegee intermediate) studied here. The second step is the oxy-insertion step, which is the subject of this work. Understanding electronic demands within organic BV reactions has been assisted by Hammett linear free energy relationship (LFER) studies. For example, computational Hammett studies were reported by Reyes and coworkers to assess the effect of electron-donating/withdrawing substituents on the kinetics of BV reactions.[76] The reactions studied were conversions of *para*-substituted

acetophenones to esters by reaction with *m*-chloroperbenzoic acid (*m*-CPBA). In the Reyes study, the Criegee intermediate results from nucleophilic addition to the carbonyl group and proton transfer from *m*-CPBA to the carbonyl oxygen. For the organic BV transformation, donor groups on the acetophenone aryl group were calculated to facilitate the aryl migration step.[74,76] For example, for the organic BV reaction changes of 5 kcal/mol (performic acid oxidant) and 6 kcal/mol (trifluoroperacetic acid oxidant) have been calculated for free energies of activation ($\Delta\Delta G_R^{\ddagger}$) from the most ($NO_2$) to least electron-donating (OCH_3) migrating group substituent.[74,76] This is ~ 50% of the $\Delta\Delta G_R^{\ddagger}$ calculated for the present organometallic BV transition states (see above), although the electronic impact of substituent modification is more commensurate in percentage terms. In addition, the differences in identity of the oxidants complicate a direct comparison of the influence of the electronic effects of the migrating group for the organic and organometallic systems. Reyes *et al.*[74,76] also noted the possibility of a change in the rate determining step from aryl migration to carbonyl addition when a *p*-OMe substituent is present on the acetophenone aryl group. The detailed study by included the impact of an acid catalyst, which promotes the reaction through protonation of the carbonyl oxygen.[74,76] EDGs on the migrating aryl group were found to reduce the activation barrier for the migration step, and the magnitude of this effect is dependent on the identity of the oxidant. Importantly, the influence of the substituents on the aryl group of the acetophenone is more substantial for the migration step than for the initial addition step to make the Criegee intermediate. In terms of the peracid used, the stronger the acid (*i.e.*, the better the leaving group) the lower the calculated BV free energy barriers.

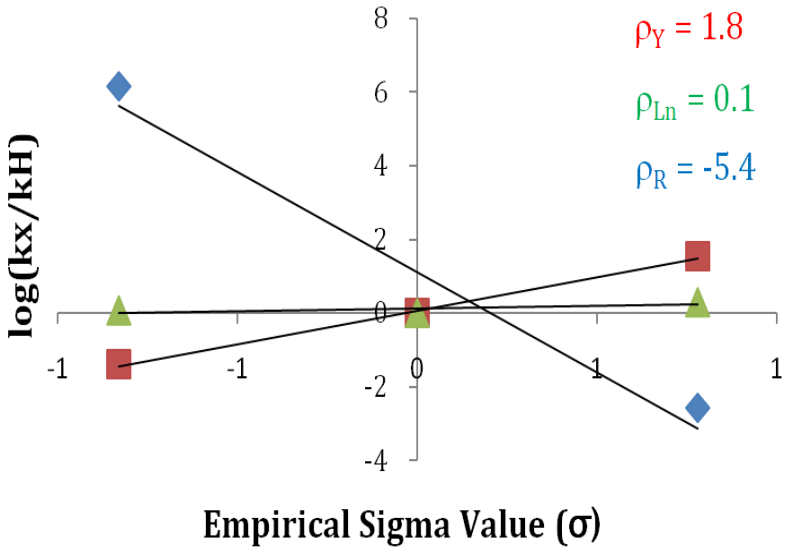

Figure 3.5. Hammett plot of $\log(k_X/k_H)$ versus the empirical sigma value (ρ_p) for *para* substituents on $[(^{X}bpy)Pt(R)(OY)]^+$ (R = *p*-X-C_6H_4, shown in blue (ρ_R); Y = 4-X-pyridine, shown in red (ρ_Y); ^{X}bpy = 4,4'-X-bpy, shown in green (ρ_{Ln}); X = NO_2, H, NMe_2).

A Hammett plot was constructed to assess the impact of varying the substituents of R, Y and the bpy ligand (Figure 3.5). Table 1 summarizes the calculated free energies for BV oxy-insertion for all complexes studied in this research. The present calculations reveal similarities to the calculations of the organic analog: the influence of modulating the donor ability of the migrating group is more impactful than the altering the donor ability of the leaving group of the oxidant.

Table 3.2 lists the "active site" bond lengths (*i.e.*, those among Pt, C_{ipso} of aryl transfer group, and O/N of the oxidant) for each of the calculated BV transition states. The calculated M–O (1.99 ± 0.01 Å) and M–C (2.08 ± 0.02 Å) bond distances in the BV transition states are close to ground state Pt–O bond lengths of Pt–aryloxide structures extracted from the Cambridge Structural Database (CSD):[77] Pt–aryloxide = 2.02 ± 0.04 Å (n = 147), n = sample size. Note that the average Pt–pyridine distance derived from an analysis of the CSD [2.04 ± 0.04 Å (n = 64)] is

much shorter than calculated Pt–N bond distances (≥ 3.2 Å), suggesting that there is little to no interaction between Pt and the pyridine moiety in these BV transition states.

Table 3.1. Calculated free energy barriers for organometallic Baeyer-Villiger oxy-insertion.

R	YO	L_n	$\Delta G_{BV}^{\ddagger}$ (kcal/mol)
Ph	PyO	bpy	42.1
p-NO2-C6H4	PyO	bpy	45.6
p-NMe2-C6H4	PyO	bpy	33.7
Ph	4-NO2-PyO	bpy	40.0
Ph	4-NMe2-PyO	bpy	44.0
p-NMe2-C6H4	4-NO2-PyO	bpy	32.2
Ph	PyO	4,4'-NO_2-bpy	42.0
Ph	PyO	4,4'-NMe_2-bpy	41.7

A plot of the free energy barriers versus O–N bond lengths was created to elucidate any possible correlation between the size of the barriers and the "lateness" of the BV transition state (Figure 3.6). From the plot in Figure 3 it is seen that *the BV barrier decreases as the O–N bond distance decreases*. The O–C and O–N distances have opposite linear correlations with respect to $\Delta G_{BV}^{\ddagger}$ as these two bond lengths are highly negatively correlated (R = -0.987) with each other. Thus, as *the O--C bond length increases the activation barrier to the BV reaction decreases* (Figure 3.7). These correlations suggest that an "earlier" BV transition state correlates with a lower free energy barrier, a reasonable result in line with the Hammond postulate.

Table 3.2. Summary of calculated bond lengths (Å) for the transition states of organometallic BV reactions. The last row provides average bond distances from Cambridge Structural Database.

Complex	Pt–O	Pt–N	Pt–C	O–N	O–C
$[(bpy)Pt(Ph)PyO]^+$	1.98	3.31	2.08	1.91	1.87
$[(bpy)Pt(p\text{-}NO_2\text{-}C_6H_4)(PyO)]^+$	1.98	3.34	2.10	1.94	1.83
$[(bpy)Pt(p\text{-}NMe_2\text{-}C_6H_4)(PyO)]^+$	2.00	3.26	2.05	1.84	1.96
$[(bpy)Pt(Ph)(4\text{-}NO_2\text{-}PyO)]^+$	1.99	3.30	2.08	1.88	1.91
$[(bpy)Pt(Ph)(4\text{-}NMe_2\text{-}PyO)]^+$	1.98	3.30	2.09	1.94	1.85
$[(bpy)Pt(p\text{-}NMe_2\text{-}C_6H_4)(4\text{-}NO_2\text{-}PyO)]^+$	2.01	3.25	2.04	1.79	2.00
$[(4,4'\text{-}NO_2\text{-}bpy)Pt(Ph)PyO]^+$	1.98	3.30	2.08	1.92	1.87
$[(4,4'\text{-}NMe_2\text{-}bpy)Pt(Ph)PyO]^+$	1.99	3.32	2.09	1.91	1.89
Calculated Average	1.99 ± 0.01	3.30 ± 0.03	2.08 ± 0.02	1.89 ± 0.05	1.90 ± 0.06
Crystal Structure Average[77]	2.02 ± 0.04	2.04 ± 0.04	2.03± 0.05	1.32± 0.02	1.33± 0.02

3.4 Summary and Conclusions

Calculated Hammett trends for $[(^{X}bpy)Pt(R)(OY)]^+$ (R = p-X-C_6H_4; Y = 4-X-pyridine; ^{X}bpy = 4,4'-X-bpy; X = NO_2, H, NMe_2) with respect to influence of the migrating group (R) and the oxidant (YO) are consistent with the organic BV literature in two regards. First, electron-withdrawing capability on the oxidant will stabilize a negative charge on the inserting oxygen and lower the barrier to the organometallic BV transformation. Second, electron-donating groups on the migrating group are predicted to facilitate the reaction. These similarities between the organic and organometallic BV transformations suggest that the greater body of research[78] that is published on organic BV chemistry may be pertinent in realizing organometallic BV transformations.

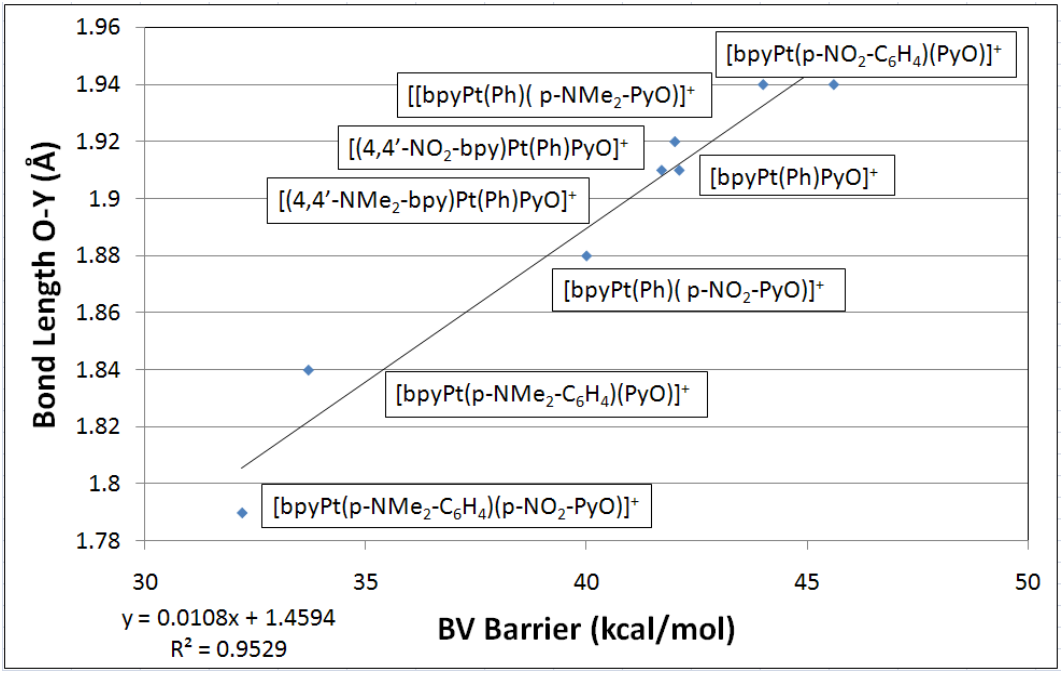

Figure 3.6. Bond length correlation plot of the active site bond lengths in the transition states. A plot of BV free energy barriers versus O–N bond distances.

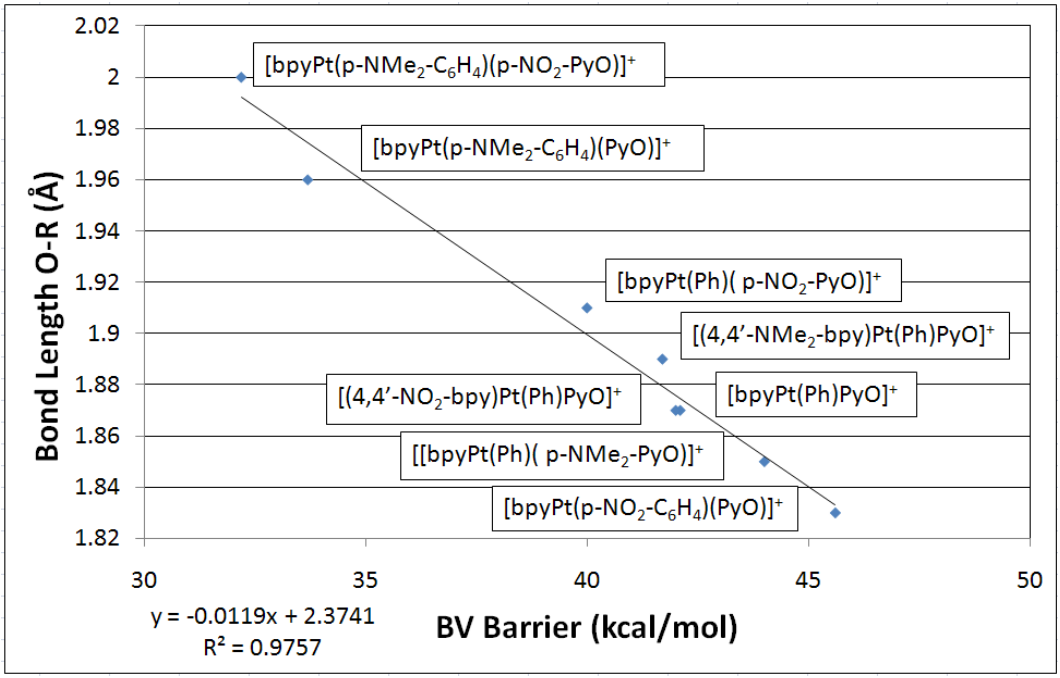

Figure 3.7. Bond length correlation plot of the active site bond lengths in the transition states. A plot of BV free energy barriers versus O–C bond distances.

The three point Hammett plot (Figure 3.5) reveals ρ_Y = 1.8, which reflects a modest impact on the activation barrier. As in the study by Reyes *et al.*,[74] the impact of changing the electronic demand of the leaving group of the oxidant (Y) is not as significant as that calculated for modifying the migratory group (R). For the *p*-NO_2/*p*-NMe_2-substituted aryl migrating groups, the "spread" [$\Delta\Delta G^{\ddagger}(R_{NMe2,NO2})$] is 12 kcal/mol, which is three times larger $\Delta\Delta G^{\ddagger}(YO_{NMe2,NO2})$ ~ 4 kcal/mol] than 4-NO_2/4-NMe_2-substituted oxidant leaving groups. Furthermore, the Hammett correlation for substitution of the migrating group gives ρ_R = -5.4, Figure 3.5, which is a substantially greater magnitude than the 1.8 value for ρ_Y. For this d^8 model, the influence of bipyridyl modification is minimal, $\Delta\Delta G^{\ddagger}(L_{NMe2,NO2})$ ~ 0.4 kcal/mol. Of course, whether or not these calculated trends will extend to other metal systems remains to be determined.

It is worth noting that the N–O bond strength is calculated to be *weakened* by 1.0 kcal/mol in the 4-NO_2-PyO versus PyO (determined by calculating the enthalpy of YO → Y + ½ O_2), and strengthened by 2.5 kcal/mol for 4-NMe_2-PyO at the same B3LYP/CEP-31G(d) level of theory employed for the Pt-based simulations. Hence, it is plausible that the impact on the free energy barriers upon modification of the 4-pyridine substituent ($\Delta\Delta G_Y^{\ddagger}$ ~ 4 kcal/mol) reflects, at least in part, changes in N–O bond strengths and thus oxidant power. Interestingly, calculated homolytic Pt–C bond strengths for the phenyl migrating group (*i.e.*, [(bpy)Pt(*p*-X-C_6H_4)(OPy)]$^+$ → ([(bpy)Pt(OPy)]$^{+\bullet}$ + *p*-X$^{\bullet}$-C_6H_4, X = H, NO_2, NMe_2) are calculated to be weakened by 1.6 kcal/mol in the 4-NO_2-Ph versus the unsubstituted phenyl, and strengthened by 2.2 kcal/mol for 4-NMe_2-Ph, a trend that counteracts the observed $\Delta\Delta G_R^{\ddagger}$ ~ 12 kcal/mol. However, the C–O bond enthalpy differences for the *p*-OX-C_6H_4X moiety that is formed (determined by calculating the enthalpy of *p*-X$^{\bullet}$-C_6H_4 + ½ O_2 → *p*-XO$^{\bullet}$-C_6H_4 are calculated to be weakened by 2.3 kcal/mol for the 4-NO_2-PhO$^{\bullet}$ versus the standard PhO, and strengthened by 9.5 kcal/mol for 4-NMe_2-PhO$^{\bullet}$.

The foregoing implies a thermodynamic advantage when the EDG is present in forming of the R–O bond, which correlates with the lower barrier for this migrating group modification. Further, the impact of the C–O bond formation is greater than the Pt–C bond being broken during the course of the oxy-insertion event. Such a result is reasonable in view of the calculated TS geometries (Table 3.2, Figures 3.6 and 3.7) that show minimal lengthening of the Pt–C bond and substantial formation of the O–C bond in the calculated Baeyer-Villiger transition states.

Evidence for an organometallic BV pathway for metal-mediated C–O bond formation has been observed with $MeReO_3$.[43-45] To our knowledge, the present report is the first study that extends this reaction to other metals. Our studies provide two salient conclusions: (1) Moving toward a more electrophilic metal center, Pt(II), results in a substantial increase in the activation barrier for the C–O bond forming step. This is likely explained by a substantial decrease in the nucleophilicity of the hydrocarbyl ligand coordinated to the cationic Pt(II) metal. The natural population analysis derived atomic charges imply oxidation of the phenyl migrating group and reduction of the pyridine leaving group from the MCI to the BV transition state. These changes in atomic charges on R and Y are consistent with the Hammett ρ values. Interestingly, the platinum and oxygen atoms have no major net change in the charge. This study suggests that facile organometallic BV transformations may be difficult to achieve with late transition metal systems. (2) Hammett correlations (using calculated $\Delta G^{\ddagger}$ values) suggest that modification of the R group's nucleophilicity has a substantial impact while modifications of the ancillary ligands and of the leaving pyridyl group have a relatively minor impact on the activation barriers. Since the migrating group of organometallic BV transformations would be dictated by the substrate being converted (*e.g.*, R = Me for MTM catalysis), this limits opportunities to manipulate rates of the oxy-insertion by the BV pathway. Hence, the present computational studies imply that

future experimental studies be directed at other transition metals, dramatically different ligand motifs (especially those with more substantial electronic coupling between metal and ligand), and protocols to catalyze the organometallic BV reaction and net oxy-insertion by different mechanisms.

3.5 References

(1) Chenier, P. J. *Survey of Industrial Chemistry*; John Wiley & Sons, Inc.: New York, **1986**.

(2) Weissermel, K. *Industrial Organic Chemistry*; VCH: New York, **1997**.

(3) Olah, G. A. *Beyond Oil and Gas: The Methanol Economy*; Wiley-VCH, **2006**.

(4) Olah, G. A.; Goeppert, A.; Prakash, G. K. S. *J. Org. Chem.* **2009**, *74*, 487.

(5) Labinger, J. A. *J. Mol. Cat.* **2004**, *220*, 27.

(6) Owen, J. S.; Labinger, J. A.; Bercaw, J. E. *J. Am. Chem. Soc.* **2006**, *2006*, 2005.

(7) Stahl, S. S.; Labinger, J. A.; Bercaw, J. E. *Angew. Chem.* **1998**, *37*, 2181.

(8) Conley, B. L.; III, W. J. T.; Young, K. J. H.; Ganesh, S. K.; Meier, S. K.; Ziatdinov, V. R.; Mironov, O.; Oxgaard, J.; Gonzales, J.; III, W. A. G.; Periana, R. A. *J. Mol. Cat.* **2006**, *251*, 8.

(9) Goldberg, K. I.; Goldman, A. S. *Activation and Functionalization of C-H Bonds*; American Chemical Society: Washington, DC, **2004**.

(10) Webb, J. R.; Bolano, T.; Gunnoe, T. B. *ChemSusChem* **2011**, *4*, 37.

(11) Wolf, D. *Angew. Chem. Int. Ed.* **1998**, *37*, 3351.

(12) Shilov, A. E.; Shul'pin, G. B. *Chem. Rev.* **1997**, *97*, 2879.

(13) Zhong, H. A.; Labinger, J. A.; Bercaw, J. E. *J. Am. Chem. Soc.* **2002**, *124*, 1378.

(14) Johansson, L.; Tilset, M.; Labinger, J. A.; Bercaw, J. E. *J. Am. Chem. Soc.* **2000**, *122*, 10846.

(15) Lersch, M.; Tilset, M. *Chem. Rev.* **2005**, *105*, 2471.

(16) Periana, R. A.; Taube, D. J.; Gamble, S.; Taube, H.; Satoh, T.; Fujii, H. *Science* **1998**, *280*, 560.

(17) Wong-Foy, A. G.; Henling, L. M.; Mike Day; Labinger, J. A.; Bercaw, J. E. *J. Mol. Cat.* **2002**, *189*, 3.

(18) Lin, M.; Shen, C.; Garcia-Zayas, E. A.; Sen, A. *J. Am. Chem. Soc.* **2001**, *123*, 1000.

(19) Jones, C.; Taube, D.; Ziatdinov, V. R.; Periana, R. A.; Nielsen, R. J.; Oxgaard, J.; III, W. A. G. *Angewandte Chemie* **2004**, *116*, 4726.

(20) Periana, R. A.; Taube, D. J.; Evitt, E. R.; Loffler, D. G.; Wentrcek, P. R.; Voss, G.; Masuda, T. *Science* **1993**, *259*, 340.

(21) Periana, R. A.; Bhalla, G.; William J. Tenn, I.; Young, K. J. H.; Liu, X. Y.; Mironov, O.; Jones, C.; Ziatdinov, V. R. *J. Mol. Cat.* **2004**, *220*, 7.

(22) Conner, D.; Jayaprakash, K. N.; Cundari, T. R.; Gunnoe, T. B. *Organometallics* **2004**, *23*, 2724.

(23) Feng, Y.; Lail, M.; Barakat, K. A.; Cundari, T. R.; Gunnoe, T. B.; Petersen, J. L. *J. Am. Chem. Soc.* **2005**, *127*, 14174.

(24) Hashiguchi, B. G.; Young, K. J. H.; Yousufuddin, M.; III, W. A. G.; Periana, R. A. *J. Am. Chem. Soc.* **2010**, *132*, 12542.

(25) Bischof, S. M.; Ess, D. H.; Meier, S. K.; Oxgaard, J.; Nielsen, R. J.; Bhalla, G.; William A. Goddard, I.; Periana, R. A. *Organometallics* **2010**, *29*, 742.

(26) William J. Tenn, I.; Young, K. J. H.; Bhalla, G.; Oxgaard, J.; William A. Goddard, I.; Periana, R. A. *J. Am. Chem. Soc.* **2005**, *127*, 14172.

(27) William J. Tenn, I.; Young, K. J. H.; Oxgaard, J.; Nielsen, R. J.; William A. Goddard, I.; Periana, R. A. *Organometallics* **2006**, *25*, 5173.

(28) Oxgaard, J.; William J. Tenn, I.; Nielsen, R. J.; Periana, R. A.; William A. Goddard, I. *Organometallics* **2007**, *26*, 1565.

(29) Gonzales, J. M.; Oxgaard, J.; Periana, R. A.; III, W. A. G. *Organometallics* **2007**, *26*, 1505.

(30) Bhalla, G.; Liu, X. Y.; Oxgaard, J.; Goddard, W. A.; Periana, R. A. *J. Am. Chem. Soc.* **2005**, *127*, 11372.

(31) Ess, D. H.; Bischof, S. M.; Oxgaard, J.; Periana, R. A.; III, W. A. G. *Organometallics* **2008**, *27*, 6440.

(32) Feng, Y.; Lail, M.; Foley, N. A.; Gunnoe, T. B.; Barakat, K. A.; Cundari, T. R.; Petersen, J. L. *J. Am. Chem. Soc.* **2006**, *128*, 7982.

(33) Bercaw, J. E.; Hazari, N.; Labinger, J. A. *Organometallics* **2009**, *28*, 5489.

(34) Hanson, S. K.; Heinekey, D. M.; Goldberg, K. I. *Organometallics* **2008**, *27*, 1454.

(35) Pierpont, A. W.; Cundari, T. R. *Inorg. Chem.* **2010**, *49*, 2038.

(36) Balcells, D.; Clot, E.; Eisenstein, O. *Chem. Rev.* **2010**, *110*, 749.

(37) Boutadla, Y.; Davies, D. L.; Macgregor, S. A.; Poblador-Bahamondeb, A. I. *Dalton Trans.* **2009**, 5820.

(38) Young, K. J. H.; Mironov, O. A.; Periana, R. A. *Organometallics* **2007**, *26*, 2137.

(39) Cundari, T. R.; Grimes, T. V.; Gunnoe, T. B. *Journal of the American Chemical Society* **2006**, *129*, 13172.

(40) Kloek, S. M.; Heinekey, D. M.; Goldberg, K. I. *Angew. Chem.* **2007**, *119*, 4820.

(41) Ess, D. H.; Gunnoe, T. B.; Cundari, T. R.; III, W. A. G.; Periana, R. A. *Organometallics* **2010**, *29*, 6801.

(42) Brown, S. N.; Mayer, J. M. *J. Am. Chem. Soc.* **1996**, *118*, 12119.

(43) Conley, B. L.; Ganesh, S. K.; Gonzales, J. M.; William J. Tenn, I.; Young, K. J. H.; Oxgaard, J.; William A. Goddard, I.; Periana, R. A. *J. Am. Chem. Soc.* **2006**, *128*, 9018.

(44) Gonzales, J. M.; Jr., R. D.; Periana, R. A.; III, W. A. G.; Oxgaard, J. *J. Am. Chem. Soc.* **2007**, *129*, 15794.

(45) Bischof, S. M.; Cheng, M.-J.; Nielsen, R. J.; Gunnoe, T. B.; III, W. A. G.; Periana, R. A. *Organometallics* **2011**, *30*, 2079.

(46) Brown, S. N.; Mayer, J. M. *J. Am. Chem. Soc.* **1994**, *116*, 2219.

(47) Brown, S. N.; Myers, A. W.; Fulton, J. R.; Mayer, J. M. *Organometallics* **1998**, *17*, 3364.

(48) Brown, S. N.; Mayer, J. M. *Organometallics* **1995**, *14*, 2951.

(49) Anderson, T. M.; Neiwert, W. A.; Kirk, M. L.; Piccoli, P. M. B.; Schultz, A. J.; Koetzle, T. F.; Musaev, D. G.; Morokuma, K.; Cao, R.; Hill, C. L. *Nature* **2004**, *306*, 2074.

(50) Poverenov, E.; Efremenko, I.; Frenkel, A. I.; Ben-David, Y.; Shimon, L. J. W.; Leitus, G.; Konstantinovski, L.; Martin, J. M. L.; Milstein, D. *Nature* **2008**, *455*, 1093.

(51) Efremenko, I.; Poverenov, E.; Martin, J. M. L.; Milstein, D. *J. Am. Chem. Soc.* **2010**, *132*, 14886.

(52) Woerpel, K. A.; Bergman, R. G. *J. Am. Chem. Soc.* **1993**, *115*, 7888.

(53) McGhee, W. D.; Foo, T.; Hollander, F. J.; Bergman, R. G. *J. Am. Chem. Soc.* **1988**, *110*, 8543.

(54) Zhong, H. A.; Labinger, J. A.; Bercaw, J. E. *J. Am. Chem. Soc.* **2002**, *124*, 1378.

(55) Butschke, B.; Schwarz, H. *Organometallics* **2011**, *30*,1588.

(56) Hill, G. S.; Yap, G. P. A.; Puddephatt, R. J. *Organometallics* **1999**, *18*, 1408.

(57) Hill, G. S.; Rendina, L. M.; Puddephatt, R. J. *Organometallics* **1995**, *14*, 4966.

(58) McKeown, B. A.; Foley, N. A.; Lee, J. P.; Gunnoe, T. B. *Organometallics* **2008**, *27*, 4031.

(59) Stephens, P. J.; Devlin, F. J.; Chabalowski, C. F.; Frisch, M. J. *J. Phys. Chem.* **1994**, *98*, 11623.

(60) Lee, C.; Yang, W.; Parr, R. G. *Phys. Rev. B* **1988**, *37*, 785.

(61) Becke, A. D. *J. Phys. Chem.* **1988**, *98*, 11623.

(62) Stevens, W. J.; Basch, H.; Krauss, M. J. *J. Chem. Phys.* **1984**, *81*, 6026.

(63) Cundari, T. R.; Stevens, W. J. *J. Chem. Phys.* **1993**, *98*, 5555.

(64) Frisch, M. J.; et al. Gaussian 09, R. A., Gaussian, Inc., Wallingford CT **2009**.

(65) Cundari, T. R.; Jimenez-Halla, J. O. C.; Morello, G. R.; Vaddadi, S. *Journal of the American Chemical Society* **2008**, *130*, 13051.

(66) DeYonker, N. J.; Foley, N. A.; Cundari, T. R.; Gunnoe, T. B.; Petersen, J. L. *Organometallics* **2007**, *26*, 6604.

(67) Cundari, T. R.; Stevens, W. J. *Journal of Chemical Physics* **1993**, *98*, 5555.

(68) Feng, Y.; Lail, M.; Foley, N. A.; Gunnoe, T. B.; Barakat, K. A.; Cundari, T. R.; Petersen, J. L. *J. Am. Chem. Soc.* **2006**, *128*, 7982.

(69) Feng, Y.; Gunnoe, T. B.; Grimes, T. V.; Cundari, T. R. *Organometallics* **2006**, *25*, 5456.

(70) Foley, N. A.; Lee, J. P.; Ke, Z.; Gunnoe, T. B.; Cundari, T. R. *Accounts of Chemical Research* **2009**, *42*, 585.

(71) Cossi, M.; Rega, N.; Scalmani, G.; Barone, V. J. *J. Comput. Chem.* **2003**, *24*, 669.

(72) Barone, V.; Cossi, M. *J. Phys. Chem. A* **1998**, *286*, 253.

(73) Hansch, C.; Leo, A.; Taft, R. W. *Chem. Rev.* **1990**, *91*, 165.

(74) Reyes, L.; Alvarez-Idaboy, J. R.; Mora-Diez, N. *J. Phys. Org. Chem.* **2009**, *22*, 643.

(75) Kinnunen, T. J.; Haukka, M.; Nousiainen, M.; Patrikka, A.; Pakkanen, T. A. *J.Chem.Soc.,Dalton Trans.* **2001**, 2649.

(76) Reyes, L.; Castro, M.; Cruz, J. n.; Rubio, M. *J. Phys. Chem. A* **2005**, *109*, 3383.

(77) Allen, F. *Acta Cryst.* **2002**, *58*, 380.

(78) Renz, M.; Meunier, B. *Eur. J. Org. Chem.* **1999**, 737.

CHAPTER 4

CARBON–OXYGEN BOND FORMATION *VIA* ORGANOMETALLIC BAEYER–VILLIGER TRANSFORMATIONS: A COMPUTATIONAL STUDY ON THE IMPACT OF METAL IDENTITY*

4.1 Introduction

Selective catalysts for the direct partial oxidation of hydrocarbons, especially alkanes, have been a long-standing goal.[1-13] Several strategies for catalytic C–H functionalization have evolved, with the most heavily studied systems including electrophilic late transition metals (*e.g.*, Pt, Pd, Hg and Au),[1-4, 9, 14-16] high valent metal–oxo or nitrene systems,[17-22] and transition metal carbene complexes.[23, 24] Among the more promising catalysts for hydrocarbon partial oxidation are electrophilic late transition metal systems.[1-3, 9, 14, 15] For example, heating aqueous solutions of Pt(II) salts with hydrocarbons and an external oxidant produces alcohol or alkyl chloride compounds (the Shilov system).[1, 12, 25] The most commonly invoked pathway for Shilov catalysts involves initial alkane C–H activation to generate a Pt(II)–alkyl intermediate, oxidation of the Pt(II)–alkyl to produce a Pt(IV)–alkyl species, nucleophilic attack by water or chloride on the hydrocarbyl ligand and dissociation of the functionalized product. Despite numerous studies that have revealed details of this and related systems,[4, 9, 12, 16, 26] several limitations that prevent the implementation of scaled-up processes have not been overcome.

One key goal for the development of catalysts for selective hydrocarbon partial oxidation is the incorporation of inexpensive oxidants that can be regenerated from dioxygen. The original Shilov catalytic system utilized Pt(IV) as the stoichiometric oxidant,[25] and although examples

* This chapter is presented in its entirety from T. M. Figg, J. R. Webb, T. B. Gunnoe, and T. R. Cundari "Carbon–Oxygen Bond Formation via Organometallic Baeyer–Villiger Transformations: A Computational Study on the Impact of Metal Identity" J. Am. Chem. Soc., 2012, 134, 2332 with permission from the American Chemical Society.

with other oxidants have been reported (*e.g.*, H_2SO_4),[3] the development of processes that utilize oxidants other than Pt(IV)) has been challenging.[9, 27, 28]

An alternative strategy to Shilov-type catalysis is a process that involves C–O bond formation by net oxygen-atom insertion into a M–R bond. An example of such a catalytic cycle is shown in Figure 4.1, which involves C–H activation by 1,2-CH-addition across a M–OR bond and oxygen-atom insertion into a M–R bond as the key steps.[5, 29-31] In Figure 4.1, two distinct pathways for oxygen-atom insertion are shown. One involves the formation of a metal oxo complex upon dissociation of "Y," which formally oxidizes the metal by two electrons, followed by net migration of the ligand R to the oxo to produce an alkoxide ligand. Well-defined methyl migration to oxo ligands has only been observed for a few systems,[32, 33] and examples of thermally induced (R)M≡O → M–OR are extremely rare.[32]

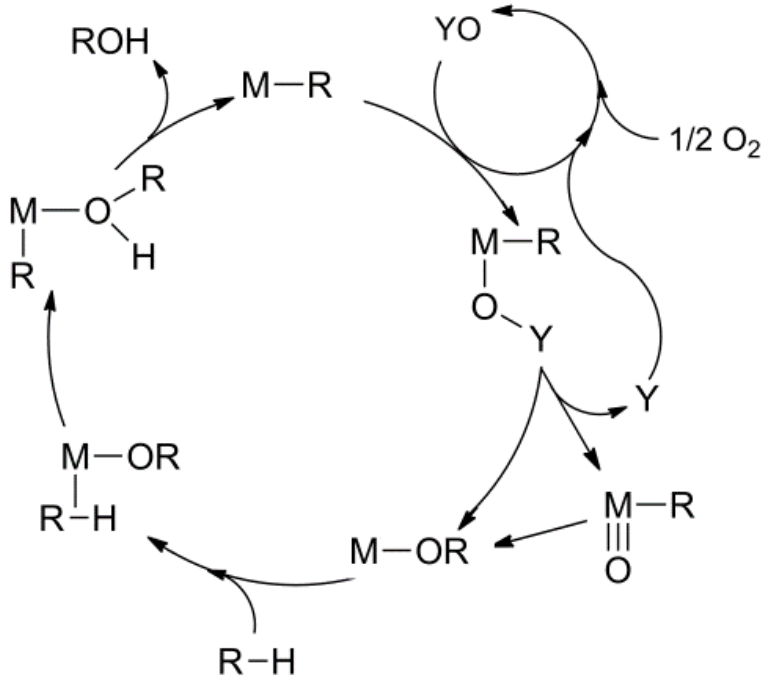

Figure 4.1. Possible pathways for C–H functionalization involving oxygen atom insertion into a M–R bond and 1,2-CH-addition across a metal–heteroatom bond.

As previously discussed, [32] an inherent challenge to oxo insertion into M–R bonds is that metal–hydrocarbyl and metal–oxo bonds are often polarized such that the hydrocarbyl and oxo are both nucleophilic. In fact, Mayer and Brown have suggested that oxo insertion into a Re(VII)–phenyl bond is a result of strong oxo-to-Re π-donation, which enhances the electrophilicity of the oxo ligands. A second pathway for C–O bond formation in Scheme 1 is a direct oxygen-atom insertion and concomitant loss of Y without prior formation of a metal oxo complex. Henceforth, this pathway will be referred to as an organometallic Baeyer–Villiger (OMBV) reaction. The OMBV reaction occurs without changing the formal oxidation state of the metal.

Despite the possible utility of metal-mediated C–O bond forming reactions, the net insertion of oxygen into metal–alkyl or metal–aryl bonds of middle to late transition metals to give alkoxide or aryloxide ligands has been observed only rarely. Brown and Mayer have reported oxo insertion into M–R bonds with Re(VII) under both thermal and photolytic conditions.[32, 33] Hillhouse *et al.* have reported examples of Ni–C → Ni–O–C transformations.[34-36] For example, the reaction of $(PMe_3)_2Ni(\kappa^2\text{-}C,C\text{-}CH_2CMe_2\text{-}o\text{-}C_6H_4)$ with N_2O in C_6D_6 for three days at 55 ºC produces $[(PMe_3)Ni(\kappa^2\text{-}O,C\text{-}O\text{-}o\text{-}C_6H_4CMe_2CH_2)]_2$. Oxygen atom insertion into Pd–aryl bonds has been reported,[37] and proposed pathways involve the formation of Pd(IV) oxo complexes;[38] however, evidence for the formation of Pd(IV) oxo systems has not been reported. Espenson *et al.* reported that the reaction of methyltrioxorhenium (MTO) with oxidants generates methanol.[39] Recently, Periana, Goddard *et al.* reported that the reaction of MTO with two equivalents of external oxidant (*e.g.*, PhIO, H_2O_2 and IO_4^-) in D_2O at 25 ºC for one hour generates methanol. The conversion of external oxidants and the Re–Me bond of MTO to a methoxide ligand does not involve the migration of a methyl group to an oxo ligand.[29, 40] Rather, an OMBV pathway was proposed with a calculated activation barrier of 17 kcal/mol for IO_4^-

(Figure 4.2). Application of this reaction to an analogous Re–aryl system, O_3ReAr (Ar = mesityl), has been demonstrated to proceed through an OMBV pathway to produce the corresponding phenol.[41]

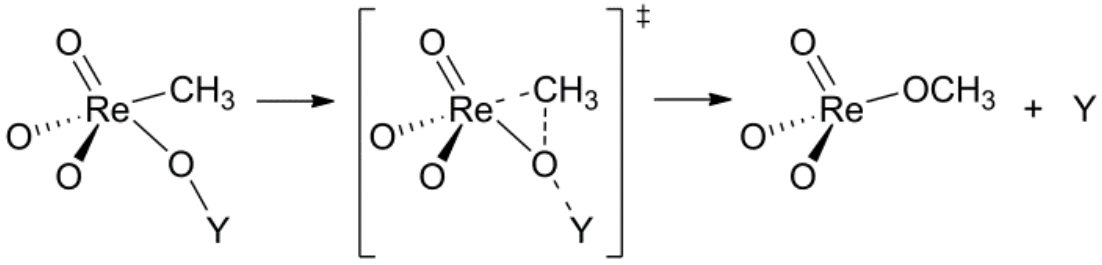

Figure 4.2. Organometallic Baeyer–Villiger transition state for oxygen atom insertion into the Re–Me bond of methyltrioxorhenium (MTO).

Extension of the OMBV transformation to systems for which the resulting metal–alkoxide (or aryloxide) can activate C–H bonds[5, 30, 31, 42-48] offers the opportunity to develop catalytic processes for the direct conversion of hydrocarbons to alcohols. The Re(VII) methoxide complex $O_3Re(OMe)$, which forms from MTO and YO (Y = HO^-, pyridine, IO_3^-, PhI), is insufficiently reactive to activate C–H bonds, and this is likely a common feature of d^0 M–OMe complexes. Thus, completion of the catalytic cycle shown in Figure 4.1 would likely require access to the OMBV transformation with more d-electron rich metals. However, the features of the metal that facilitate the OMBV reaction are not well understood. For example, Re(VII) and Ni(II) systems have been proposed to undergo oxygen-atom insertion via the OMBV reaction, which are quite disparate transition metal complexes. In addition to the experimental studies, we have reported a computational Hammett study based on bipyridyl-Pt(II) complexes.[49] These studies suggested electronic effects similar to the organic BV reaction and indicated that the OMBV reaction with electrophilic late transition metals would have prohibitively high activation barriers. Given the scarcity of well-defined oxygen-atom insertions into M–R bonds, we sought to use DFT to establish trends that could effectively guide future experimental efforts to study

and optimize M–R → M–O–R reactions via the OMBV pathway. In this report, a systematic study was performed to elucidate trends in the OMBV reaction as a function of metal identity and coordination number. We have evaluated the reaction of a series of Group 7-10 four-coordinate d^8 and six-coordinate d^6 complexes with hydroperoxide as the oxidant. In order to focus on the impact of the metal, the ancillary ligand, 2,2'-bipyridyl (bpy), was held constant for the series of complexes studied. These studies provide distinct trends in $\Delta G^{\ddagger}$ as a function of metal identity and coordination number.

4.2 Computational Methods

The Gaussian 09 package[50] was used to model ground and transition states. Geometry optimization and vibrational frequency calculations were performed at the density functional theory (DFT) level, using the hybrid functional B3LYP,[51, 52] and the Stevens valence basis sets with psuedopotentials, and d functions added to the main group elements, *i.e.*, (CEP-31G(d)).[53-55] The current level of theory was calibrated versus computations reported against the known OMBV oxidations of ReO_3Me, (*i.e.*, $[O_3ReMe(OOH)]^- \rightarrow [O_3Re(OH)(OMe)]^-$), with no appreciable differences. Additionally, calibration of standard double-ζ-plus-polarization valence basis sets (VBSs) against larger triple-ζ-plus-polarization with diffuse functions VBSs (CEP-121G+(d)) did not afford appreciable differences in the calculated geometries and energetics. All minima and transition states were discerned by the presence of 0 or 1 imaginary frequencies, respectively, from the calculated energy Hessians. The current level of theory has been used in a previous study of organometallic Baeyer–Villiger mediated oxidation,[49] among many other analyses of organometallic catalysis, and will be used in this study to compare/contrast complexes of Group 7, 8, 9 and 10 metals of varying coordination number and d-electron count.

The free energies of activation are calculated at standard conditions (1 atm, 298.15 K) for the respective OMBV transition states, and for each metal/ligand combination the free energies are reported relative to the adduct formed by coordination of hydroperoxide, which we have termed the metallo-Criegee intermediate (MCI), $[(bpy)_xM(Me)(OOH)]^n$ (x = 1 for four-coordinate, d^8-square planar systems; x = 2 for six-coordinate, d^6-octahedral systems). Different spin states for the 3d metal systems were evaluated; whereas, 4d and 5d systems are assumed to be in the lowest singlet spin state. Most of the MCIs and the alkoxide products have the same spin state. Exceptions include the Fe(II) complex, where the MCI is a quintet and the alkoxide product is a singlet, and the Co(I) and Co(III) complexes, which exhibit spin crossover in the OMBV transition state.

Solvation was modeled using the conductor-like polarization continuum model (CPCM)[56] with THF as the model solvent. However, no substantial impact on the thermodynamics and kinetics were observed for the OMBV pathways. The present results incorporating solvent are complemented by those seen previously for another known OMBV system, MTO (O_3ReMe), whereby incorporation of continuum solvent effects had only a minimal impact on the barrier to oxy-insertion.[29]

4.3 Results

4.3.1 Oxygen Atom Insertion Reactions with Square Planar d^8 Complexes.

We begin with four-coordinate d^8 precursors of the type $[(bpy)M(OOH)(Me)]^n$ (bpy = 2,2'-bipyridyl) for which the overall charge n is varied to maintain a d^8 electron count. The OMBV reaction is shown in Figure 4.3. DFT was used to calculate $\Delta G^{\ddagger}$ and ΔG_{rxn} for complexes with M = Pt(II), Pd(II) or Ni(II) (n = 0) and M = Ir(I), Rh(I) or Co(I) (n = –1). Attempts to extend the calculations to four-coordinate or six-coordinate metals another group in either direction

(Group 8 or 11 and Group 6 or 10 respectively), while maintaining the d^8 or d^6 electronic configuration of the metal ion, led to either a non-OMBV transformation or an unstable conformation.

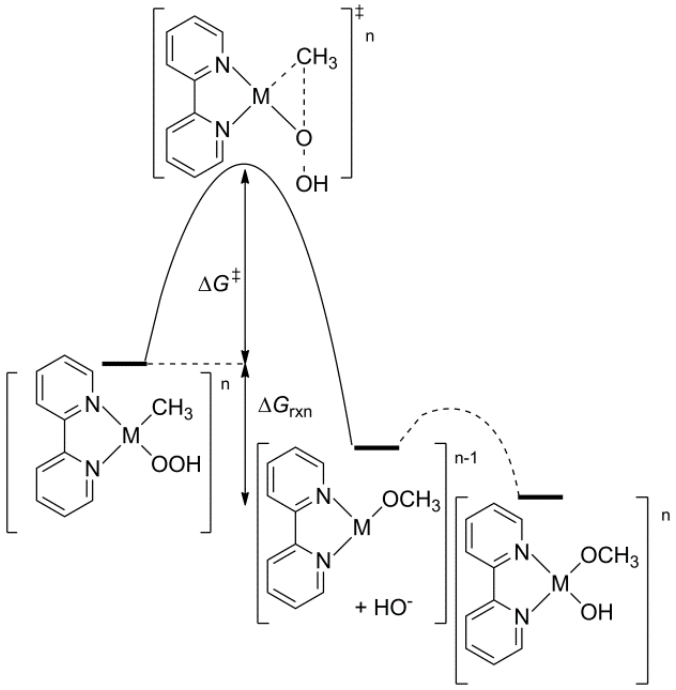

Figure 4.3. The calculated reaction pathway for an OMBV transformation starting from a four-coordinate, square planar system. The activation energy of the second step (*i.e.*, coordination of HO^-) was assumed to be negligible and was not calculated.

Table 4.1. Calculated energetics (kcal/mol) for oxygen atom insertion for d^8 four-coordinate Group 9 and 10 complexes $[(bpy)M(OOH)(Me)]^n$.

Metal	Overall Charge (n)	$\Delta G^{\ddagger}$	ΔG_{rxn}
Ni(II)	0	39.3	–67.4
Pd(II)	0	48.6	–53.2
Pt(II)	0	57.5	–51.7
Co(I)	1^-	26.3	–69.3
Rh(I)	1^-	35.6	–61.4
Ir(I)	1^-	38.6	–58.6

The calculated energetics for oxy-insertion of the Group 9 and 10 four-coordinate systems are displayed in Table 4.1. A few trends are apparent: 1) the activation barriers for 3d metals are substantially smaller than their 4d and 5d counterparts. 2) Within a congeneric series, more exergonic insertions lead to lower barriers for the oxygen atom insertion reaction. 3) The $\Delta G^{\ddagger}$'s for Group 9 complexes have consistently lower $\Delta G^{\ddagger}$'s than their Group 10 counterparts. For both Group 9 and 10 systems, with the exception of Ir(I) → Rh(I), each change in metal identity 5d → 4d → 3d results in a decrease in $\Delta G^{\ddagger}$ of ~ 9 kcal/mol. The transition from Group 10 to Group 9 results in reductions of calculated $\Delta G^{\ddagger}$'s of 27% - 33%.

Figure 4.4 shows the optimized ground state metallo-Criegee intermediate (MCI), $[(bpy)M(Me)(OOH)]^n$ and OMBV transition state geometries for the calculated d^8 four-coordinate complexes. The OMBV transition state is characterized by four co-planar chemical groups in the active site (*i.e.*, methyl, O atom, metal and hydroxide). Inspection of the calculated structures reveals some similarities. In all six cases, conversion from the MCI intermediate to the OMBV transition state results in an increase in the M–OH bond distance. Thus, these 16-electron complexes do not compensate for O–O bond cleavage by coordinating the hydroxide moiety during the O atom insertion into the metal–methyl bond. With the exception of Ir, the M–O bond distance of the coordinated oxygen atom decreases by ~ 0.06-0.1 Å upon conversion to the transition state for the OMBV reaction. In each case, the C–O bond distance in the transition state is shorter for the Group 10 complex relative to the Group 9 counterpart by 0.14-0.17 Å, which suggests a later transition state for the Group 10 systems. The position of the transition state (*i.e.*, early transition state) appears to correlate with calculated ΔG_{rxn} as the Group 10 systems are calculated to be less exothermic than corresponding Group 9 systems in the same row. The C–O bond distance in the calculated transition state for oxygen atom insertion into the

Re–Me bond of $O_3Re(Me)(OOH)$ (2.079 Å) is substantially longer than any C–O bond of the systems calculated here. The longer C–O bond distance in the MTO transition state is consistent with the calculated lower activation barrier and more exothermic reaction.[40]

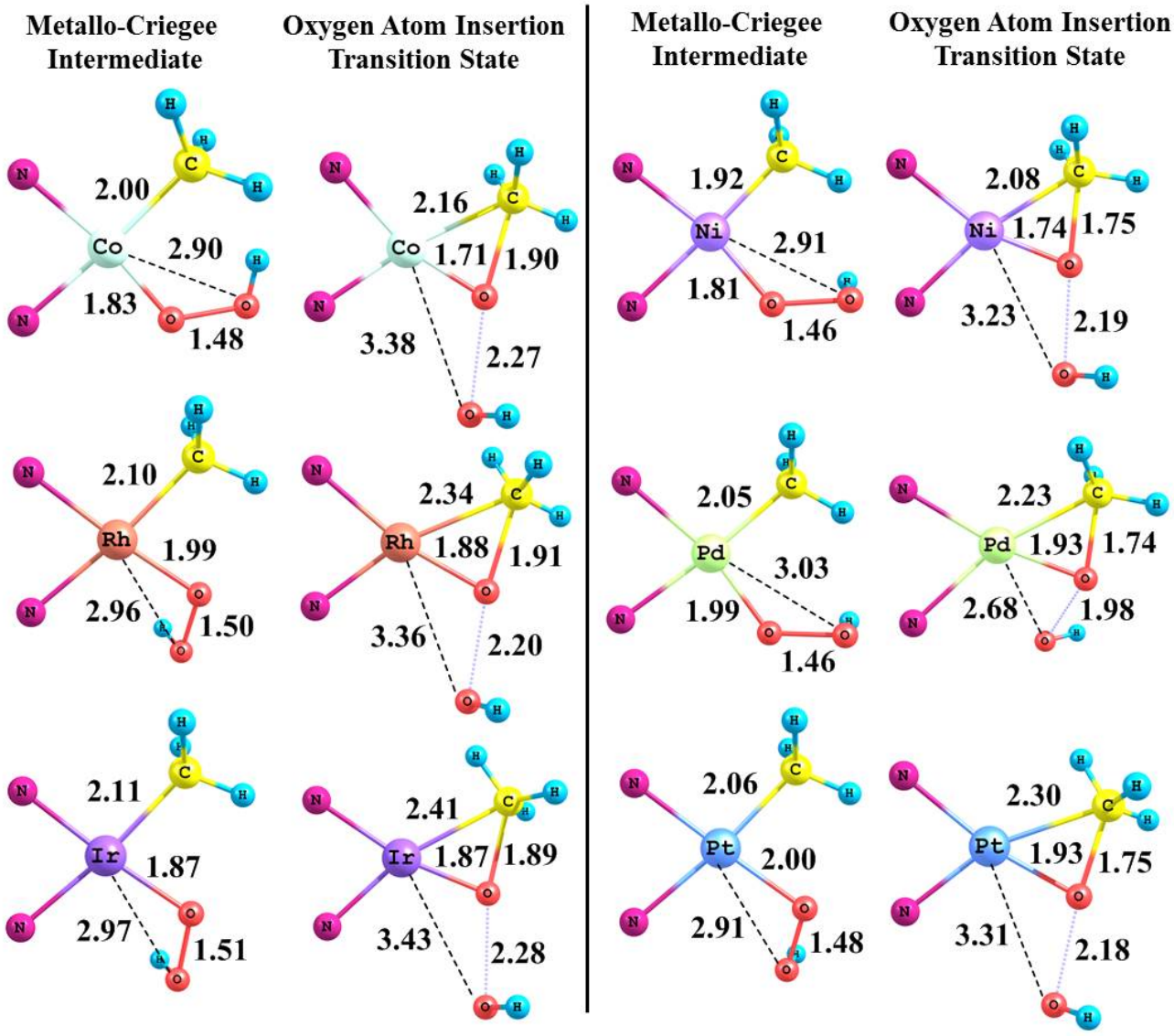

Figure 4.4. Core geometries for the four-coordinate Pt(II), Pd(II), Ni(II), Ir(I), Rh(I) and Co(I) metallo-Criegee intermediates and related OMBV transition states. Bond lengths in Å. Bpy atoms are removed, except for the N atoms, for clarity purposes.

The calculated structures for Pd reveal two distinctions relative to the other five d^8 systems. First, in the Pd transition state, the active site components (Pd, CH_3, O, and OH) are not

in the same plane, with a C–Pd–O–O dihedral angle of 160° as opposed to a dihedral angle of ~ 180° observed for every other four-coordinate OMBV transition state modeled in this research. In addition, the Pd OMBV transition state is closer to a κ^2-O,O conformation, with the hydroxide leaving group of the oxidant at a much shorter distance (Pd–OH = 2.68 Å) than the other OMBV transition states.

4.3.2 Oxygen Atom Insertion Reactions with Octahedral d^6 Complexes.

The OMBV pathway was also modeled using a series of valence isoelectronic d^6 metal complexes of the type $[(bpy)_2M(OOH)(Me)]^n$ (M = Co, Rh or Ir, n = 1; M = Fe, Ru, or Os, n = 0; Mn or Tc, n = –1) (Figure 4.5). The six-coordinate complexes display trends in $\Delta G^{\ddagger}$ that are similar to the four-coordinate d^8 systems (Table 4.2).

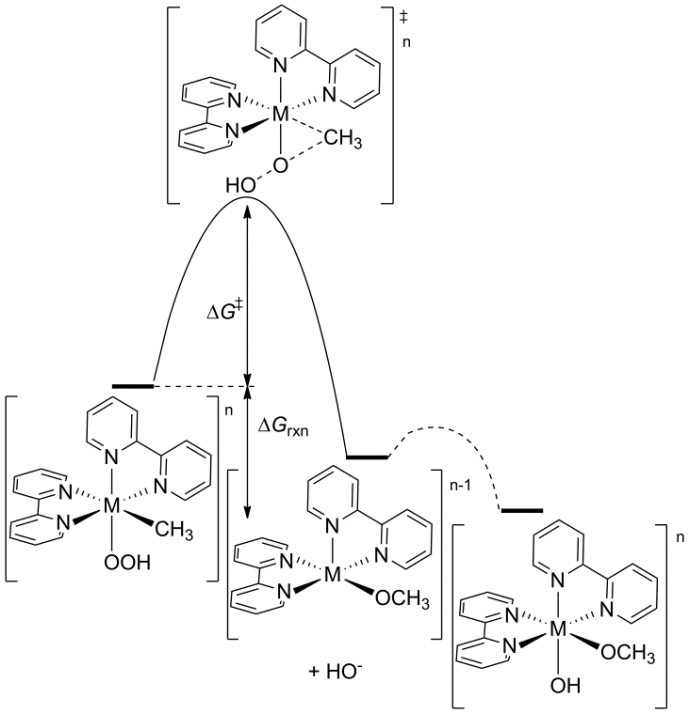

Figure 4.5. The calculated reaction pathway for an OMBV transformation through a six-coordinate system. The activation energy of the second step (*i.e.*, coordination of OH^-) was assumed to be negligible and was not calculated.

Table 4.2. Calculated energetics (kcal/mol) for oxygen atom insertion for d^6 six-coordinate Group 7, 8 and 9 complexes $[(bpy)_2M(OOH)(Me)]^n$.

Metal	Overall Charge	$\Delta G^{\ddagger}$	ΔG_{rxn}
Co(III)	1+	41.8	–61.8
Rh(III)	1+	54.7	–51.7
Ir(III)	1+	61.8	–50.1
Fe(II)	0	29.0	–71.0
Ru(II)	0	43.3	–60.4
Os(II)	0	46.5	–60.1
Mn(I)	1^-	22.6	–71.2
Tc(I)	1^-	29.0	–67.2

The more exergonic OMBV transformations correlate with smaller activation barriers, and the calculated $\Delta G^{\ddagger}$'s decrease from right to left in a row and bottom to top in a group. For the Group 9 metals, the calculated OMBV barriers for the d^6 six-coordinate complexes are significantly higher than the corresponding d^8 four-coordinate systems (*i.e.*, four-coordinate Co(I), Rh(I) and Ir(I)). Fe(II) was calculated to possess a quintet ground state for the MCI and a singlet ground state for the OMBV transition state. Mn(I) was found to be a septet for both stationary points. All other systems were singlets in the MCI ground state.

Figure 4.6 shows the optimized ground state MCI and OMBV transition state geometries for the series of d^6 six-coordinate complexes. Similar to the four-coordinate systems, all the six-coordinate OMBV transition states appear to involve a κ^1-OOH moiety as all M--O_β bond distances are $\geq$ 2.78 Å; however, for the six-coordinate complexes the distance between the metal and β-oxygen in the calculated transition state is only slightly elongated relative to the

ground state (the largest $\Delta M–O_\beta$ bond distance from MCI to transition state is 0.24 Å), while this change in bond distance is > 0.3 Å for the four-coordinate systems (with the exception of Pd).

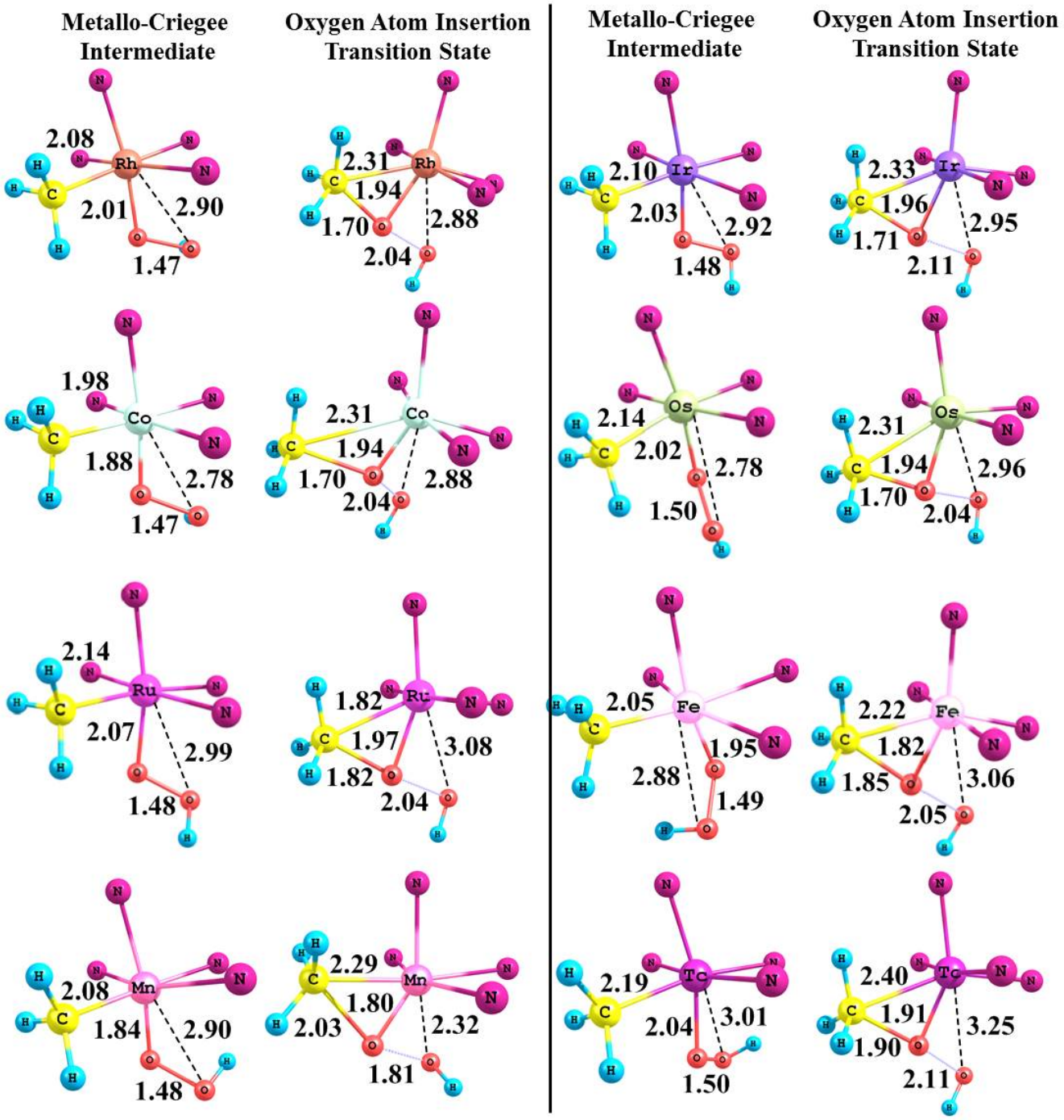

Figure 4.6. Core geometries for the six-coordinate Rh(III), Co(III), Ir(III), Fe(II), Ru(II), Os(II), Mn(I) and Tc(I) metallo-Criegee intermediates and related OMBV transition states. Bond lengths in Å. Bpy atoms are removed, except for the N atoms, for clarity purposes.

The C–O bond distances in the transition state are longest for the Group 7 complexes and shortest for the Group 9 complexes. This trend is consistent with an early transition state since the OMBV reactions for Group 9 systems are calculated to be less exothermic than the corresponding Group 7 and 8 systems in the same row.

4.4 Discussion

The calculated free energies for the OMBV reactions indicate distinct trends. For all complexes, the calculated $\Delta G^{\ddagger}$'s decrease from bottom to top within a group and from right to left within a row. For the four-coordinate precursors, calculated $\Delta G^{\ddagger}$'s for Group 9 systems are between 13 and 19 kcal/mol lower than the $\Delta G^{\ddagger}$'s of their Group 10 counterparts. For six-coordinate precursors, the magnitude of the change in $\Delta G^{\ddagger}$ on moving to the left in the period is similar to the four-coordinate systems. For example, the Group 8 systems all yielded $\Delta G^{\ddagger}$'s that are lower than the calculated barriers for Group 9 systems by 11-15 kcal/mol. In addition, a comparison of four-coordinate versus six-coordinate Group 9 precursors reveals a consistent trend of lower $\Delta G^{\ddagger}$'s for the four-coordinate systems by ~38%.

We sought a rationalization of the trends in $\Delta G^{\ddagger}$ revealed by the calculations, which would potentially allow the development of systems designed specifically to mediate the OMBV transformation. A summary of the OMBV barriers, thermodynamics, d-electron count, overall charge, homolytic bond dissociation free energies (BDFE) and Mulliken charges for the peroxide/methyl transition metal starting complexes is given in Table 4.3, which, along with the calculated $\Delta G^{\ddagger}$'s, will form the foundation of our discussion.

Table 4.3. Summary of calculated energetics, d-electron count, and atomic charges for carbon and metal atoms of MCI for four- and six-coordinate Group 7, 8 and 9 complexes (all energies given in kcal/mol; BDFE = bond dissociation free energy).

Metal	d-electron count	Overall Charge	Metal Charge	Carbon Charge	M–C BDFE	M–O BDFE	$\Delta G^{\ddagger}$	ΔG_{rxn}
Ni(II)	8	0	–0.025	–0.577	18.8	37.9	39.3	–67.4
Pd(II)	8	0	+0.036	–0.518	32.0	40.3	48.6	–53.2
Pt(II)	8	0	–0.022	–0.467	47.5	52.2	57.5	–51.7
Co(I)	8	1^-	+0.147	–0.759	9.3	30.8	26.3	–69.3
Rh(I)	8	1^-	–0.115	–0.641	32.9	51.0	35.6	–61.4
Ir(I)	8	1^-	–0.217	–0.536	39.9	54.5	38.6	–58.6
Co(III)	6	1+	–0.567	–0.468	-0.1	14.3	41.8	–61.8
Rh(III)	6	1+	–0.415	–0.400	29.3	34.4	54.7	–51.7
Ir(III)	6	1+	–0.838	–0.260	42.7	45.9	61.8	–50.1
Fe(II)	6	0	+0.173	–0.720	1.4	18.3	29.0	–71.0
Ru(II)	6	0	–0.478	–0.431	30.1	44.5	43.3	–60.4
Os(II)	6	0	–0.847	–0.369	34.7	48.3	46.5	–60.1
Mn(I)	6	1^-	+0.163	–0.546	5.4	17.5	22.6	–71.2
Tc(I)	6	1^-	–0.140	–0.593	19.0	43.4	29.0	–67.2

In a previous computational study of OMBV reactions for Pt^{II} systems, correlations among the bond distances in the active site and computed barriers were identified and analyzed to yield a working picture of the transition state for the OMBV transformation.[39] However, in the present case for a diversity of metal ions and coordination environments, examining the geometries of the four and six-coordinate species revealed no correlation between the computed barriers and the active site bond lengths. To identify correlations between properties of the precursor complexes and the calculated $\Delta G^{\ddagger}$'s, we plotted the $\Delta G^{\ddagger}$'s versus ΔG_{rxn}'s, the calculated metal-methyl and metal-oxygen bond dissociation free energies (BDFEs), Pauling

electronegativities for the metals, and the Mulliken charges for the metals and the carbon of the migrating methyl group.

A reasonable linear correlation is found for the plot of the $\Delta G^{\ddagger}$'s and the ΔG_{rxn}'s (Figure 4.7). The more exergonic the overall reaction the lower the activation barriers for the systems discussed. In order to better understand this trend, we looked for correlations between the calculated $\Delta G^{\ddagger}$'s and the strengths of M–CH_3 and M–O bonds by plotting the calculated M–CH_3 and M–O BDFEs versus $\Delta G^{\ddagger}$'s. Bond strengths for the M–CH_3 were determined by calculating the BDFEs for each system under study (eq 4.1). The bond strengths for M–O were measured by calculating the BDFEs for each system (eq 4.2). The plot of M–CH_3 BDFEs against the OMBV barriers gives a reasonable correlation (R^2 ~0.73), which shows that weaker M–CH_3 bonds tend to yield lower activation barriers (Figure 4.8). In contrast, plotting the M–O BDFE versus OMBV barriers reveals little correlation (R^2 ~0.39) (see Supporting Information for more details), suggesting that M–C bond strengths are a more significant determinant of activation barriers for the OMBV transformation than M–O bond strengths.

$$[(bpy)_xM(CH_3)(OOH)]^n \rightarrow [(bpy)_xM(OOH)]^n\bullet + \bullet CH_3 \qquad (4.1)$$

$$[(bpy)_xM(OCH_3)(OH)]^n \rightarrow [(bpy)_xM(OH)]^n\bullet + \bullet OCH_3 \qquad (4.2)$$

The Mulliken charges of the metal and carbon of the methyl group were calculated for the MCI (Table 4.3), and we plotted $\Delta G^{\ddagger}$'s as a function of these charges. While there is weak correlation between the charges on the metals and the OMBV activation barriers (R^2 = 0.38), there exists a reasonable correlation (R^2 = 0.65) between the calculated Mulliken charge on the carbon of the migrating methyl group in the MCI and the OMBV barriers (Figure 4.9).

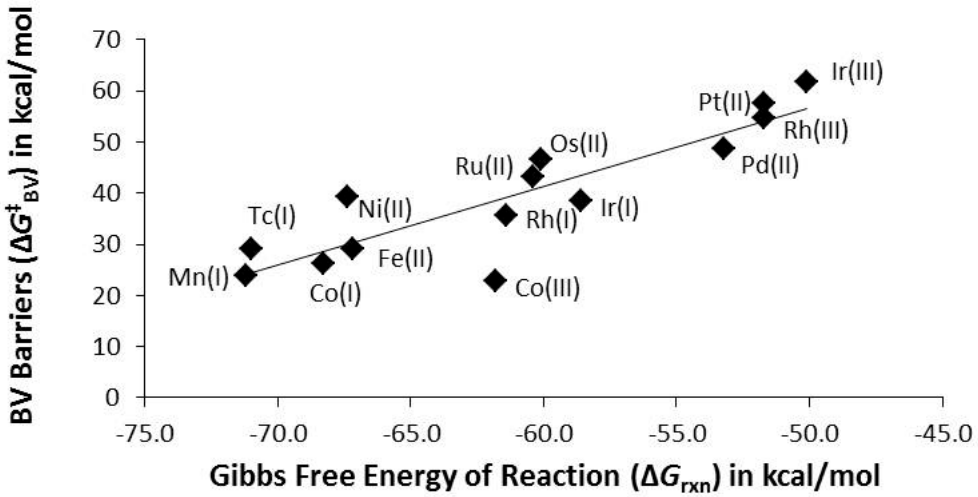

Figure 4.7. A plot of ΔG_{rxn}, $\Delta G^{\ddagger}$ (free energies, kcal/mol) for the OMBV reaction with four- and six-coordinate $[(bpy)_xM(Me)(OOH)]^n$ systems. For each data point, the metal ion and oxidation state are indicated ($R^2 = 0.77$).

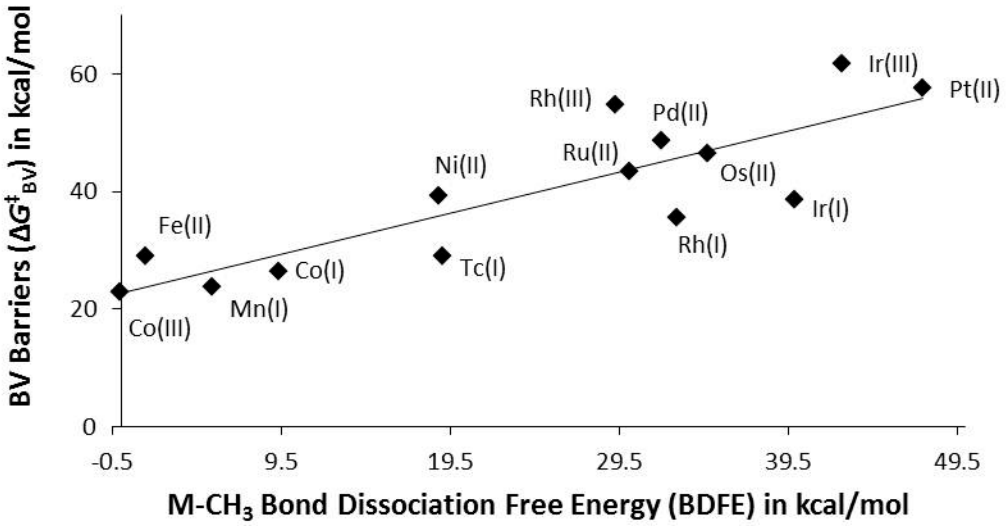

Figure 4.8. Plot of calculated M–CH_3 bond dissociation free energies (BDFE) against OMBV activation barriers in kcal/mol ($R^2 = 0.73$). The metal ion is indicated.

Much like the OMBV transformations, organic BV systems show a strong connection between the nature of the migrating group and the activation barriers for the oxidation reactions.[57-59] Thus,

the correlation in Figure 4.9 suggests that increasing the nucleophilicity of the migrating carbon results in lower activation barriers for the OMBV transformations, while the influence of the metal's charge in the MCI ground state is less predictable. To further probe the nature of the OMBV reaction, the charges for the carbon of the methyl groups, the metal, and the coordinated oxygen were calculated for the OMBV transition states. There exists a correlation between the Mulliken charges on the methyl carbon in OMBV transition state and the barriers ($R^2 = 0.60$) (Figure 4.10) as was seen for the MCI ground state. The calculated charges suggest a reduction in the negative charge of the methyl carbon during the OMBV transition state as the methyl group migrates and transfers negative charge to the oxygen atom ligated to the metal center (Table 4.4). There is no obvious linear correlation between the Pauling electronegativities of the various metals and the OMBV barriers ($R^2 = 0.22$ for four-coordinate systems and $R^2 = 0.06$ for six-coordinate systems); therefore, for the series of $[(bpy)_xM(Me)(OOH)]^n$ complexes studied herein, a higher degree of electropositive nature for the metal, at least insofar as measured by the Pauling electronegativity, does not correlate with lower OMBV activation barriers. The overall charge of the complex could also affect the activation barriers in OMBV transformations. This is evident when comparing the anionic systems, which afford lower barriers, to the neutral and cationic systems. The lower barriers could be attributed to improving the "leaving group" conditions for the anionic OH^- species.

The high spin state for Mn(I) is about 40 kcal/mol lower in energy than the low spin state for both the MCI and the corresponding OMBV transition state. Therefore, the activation barrier for oxygen atom insertion is essentially the same for high and low spin states of Mn(I).

Table 4.4. Summary of calculated atomic charges for metal, carbon, and oxygen of the MCI ground state and OMBV transition state for four- and six-coordinate Group 7, 8 and 9 complexes (all energies given in kcal/mol; BDFE = bond dissociation free energy).

Metal	MCI Metal Charge	MCI Carbon Charge	MCI Oxygen Charge	OMBV Metal Charge	OMBV Carbon Charge	OMBV Oxygen Charge
Ni(II)	–0.025	–0.577	–0.348	–0.020	–0.396	–0.299
Pd(II)	+0.036	–0.518	–0.383	+0.084	–0.404	–0.323
Pt(II)	–0.022	–0.467	–0.314	+0.046	–0.408	–0.311
Co(I)	+0.147	–0.759	–0.358	–0.087	–0.528	–0.303
Rh(I)	–0.115	–0.641	–0.339	–0.086	–0.552	–0.325
Ir(I)	–0.217	–0.536	–0.310	–0.124	–0.476	–0.314
Co(III)	–0.567	–0.468	–0.263	–0.192	–0.461	–0.291
Rh(III)	–0.415	–0.400	–0.292	–0.339	–0.347	–0.295
Ir(III)	–0.838	–0.260	–0.276	–0.713	–0.333	–0.234
Fe(II)	+0.173	–0.720	–0.373	–0.574	–0.445	–0.264
Ru(II)	–0.478	–0.431	–0.352	–0.491	–0.390	–0.294
Os(II)	–0.847	–0.369	–0.305	–0.813	–0.347	–0.238
Mn(I)	+0.163	–0.546	–0.343	+0.119	–0.477	–0.253
Tc(I)	–0.140	–0.593	–0.298	–0.093	–0.515	–0.314

The Fe(II) complex entails a spin flip from the quintet MCI ground state to a singlet in the OMBV transition state. Unlike the Mn(I) complex, there is a noticeable impact calculated for the spin-conserved barriers. For the oxygen atom insertion from low spin Fe(II) to the low spin transition state, ^{1}MCI → ^{1}OMBV transition state, the calculated $\Delta G^{\ddagger}$ is ~21 kcal/mol, which is ~8 kcal/mol lower than the quintet ground state converting to low spin transition state. In

contrast, the conversion of a quintet ground state to a quintet transition state occurs with a much larger calculated $\Delta G^{\ddagger}$ of ~46 kcal/mol.

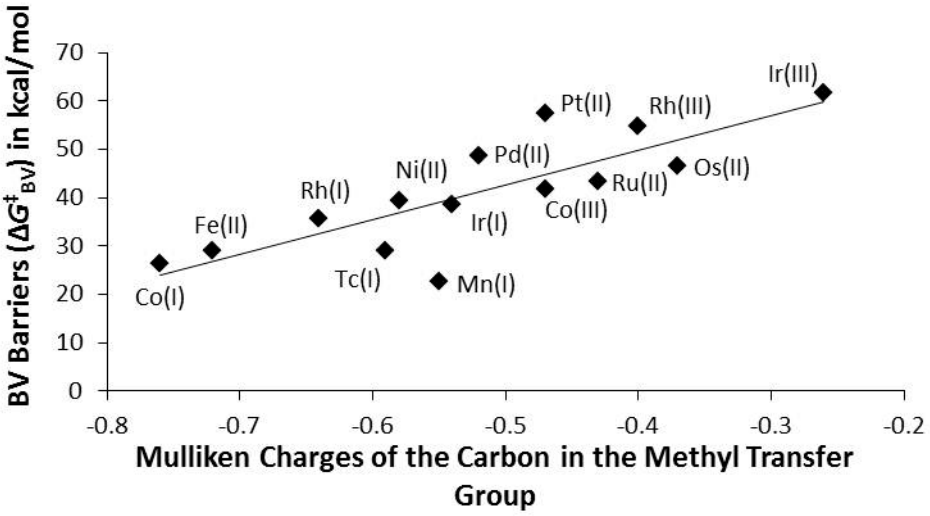

Figure 4.9. A plot of calculated Mulliken charges on the carbon of the methyl migrating group for four- and six-coordinate metallo-Criegee intermediates and calculated OMBV barriers (free energies, kcal/mol)($R^2 = 0.65$). The central metal ion is indicated.

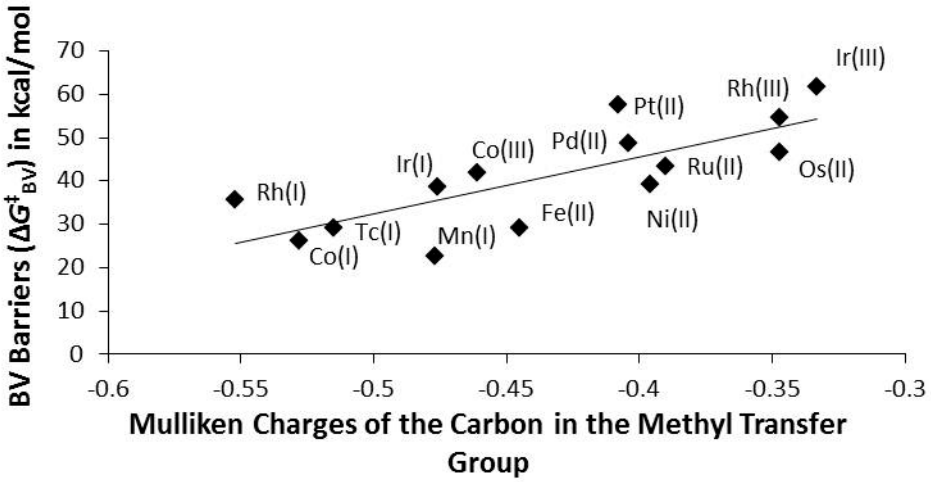

Figure 4.10. A plot of calculated Mulliken charges on the carbon of the methyl migrating group of the OMBV transition states and calculated barriers (free energies, kcal/mol) for four- and six-coordinate geometries discussed in the text ($R^2 = 0.60$). The central metal ion is indicated.

4.5 Summary and Conclusions

The OMBV reaction provides a route for C–O bond formation via M–R + YO → M–OR + Y. To our knowledge, two examples of this transformation, one with Re(VII) and one with Ni(II), have been suggested.[29, 34] In order to rationally extend this transformation to other complexes and, hence, to potentially incorporate OMBV into catalytic sequences for hydrocarbon functionalization, a better understanding of the factors that control the energetics of the reaction is needed. Within the confines of d^6 and d^8 complexes, our calculations suggest clear guidelines to optimize systems for the OMBV reaction, including the use of middle transition metals (*i.e.*, earlier metals) in a row (at least to Group 7), first row metals, and low coordinate complexes (four versus six-coordinate). The focus on d^6 and d^8 complexes is motivated by examples of Y–H (Y = C or H) activation by M–OR systems with these d-electron counts.[30, 31, 42-48, 60-62] The source of these trends appears to lie in metal–carbon BDFE's and/or charges on the migrating methyl group.

4.6 References

(1) Shilov, A. E.; Shulpin, G. B., *Russ. Chem. Rev.* **1987,** *56*, 442-464.

(2) Periana, R. A.; Taube, D. J.; Evitt, E. R.; Loffler, D. G.; Wentrcek, P. R.; Voss, G.; Masuda, T., *Science* **1993,** *259*, 340-343.

(3) Periana, R. A.; Taube, D. J.; Gamble, S.; Taube, H.; Satoh, T.; Fuji, H., *Science* **1998,** *280*, 5650.

(4) Labinger, J. A., *J. Mol. Cat. A: Chem.* **2004,** *220*, 27-35.

(5) Webb, J. R.; Bolaño, T. B.; Gunnoe, T. B., *ChemSusChem* **2011,** *4*, 37-49.

(6) Conley, B. L.; Tenn, W. J.; Young, K. J. H.; Ganesh, S. K.; Meier, S. K.; Ziatdinov, V. R.; Mironov, O.; Oxgaard, J.; Gonzales, J.; Goddard, W. A.; Periana, R. A., *J. Mol. Cat. A: Chem.* **2006,** *251*, 8-23.

(7) Periana, R. A.; Bhalla, G.; Tenn, W. J.; Young, K. J. H.; Liu, X. Y.; Mironov, O.; Jones, C. J.; Ziatdinov, V. R., *J. Mol. Cat. A: Chem.* **2004,** *220*, 7-25.

(8) Goldberg, K. I.; Goldman, A. S., *Activation and Functionalization of C-H Bonds*. American Chemical Society: Washington, DC, 2004; Vol. 885.

(9) Stahl, S. S.; Labinger, J. A.; Bercaw, J. E., *Angew. Chem. Int. Ed.* **1998,** *37*, 2180-2192.

(10) Jones, W. D., *Science* **2002,** *295*, 289-290.

(11) Fulton, J. R.; Holland, A. W.; Fox, D. J.; Bergman, R. G., *Acc. Chem. Res.* **2002,** *35*, 44-56.

(12) Shilov, A. E.; Shul'pin, G. B., *Chem. Rev.* **1997,** *97*, 2879-2932.

(13) Crabtree, R. H., *J. Chem. Soc., Dalton Trans.* **2001**, 2437-2450.

(14) Jones, C. J.; Taube, D.; Ziatdinov, V. R.; Periana, R. A.; Nielson, R. J.; Oxgaard, J.; Goddard III, W. A., *Angew. Chem. Int. Ed.* **2004,** *43*, 4626-4629.

(15) Muehlhofer, M.; Strassner, T.; Herrmann, W. A., *Angew. Chem. Int. Ed.* **2002,** *41*, 1745.

(16) Lersch, M.; Tilset, M., *Chem. Rev.* **2005,** *105*, 2471-2526.

(17) Theopold, K. H.; Gunay, A., *Chem. Rev.* **2010,** *110*, 1060-1081.

(18) Chen, M. S.; White, M. C., *Science* **2007,** *318*, 783-787.

(19) Que, J., L.; Ho, R. Y. N., *Chem. Rev.* **1996,** *96*, 2607-2624.

(20) Diaz-Requejo, M. M.; Belderrain, T. R.; Nicasio, M. C.; Trofimenko, S.; Perez, P. J., *J. Am. Chem. Soc.* **2003,** *125*, 12078-12079.

(21) Badiei, Y. M.; Dinescu, A.; Dai, X.; Palomino, R. M.; Heinemann, F. W.; Cundari, T. R.; Warren, T. H., *Angew. Chem. Int. Ed.* **2008,** *47*, 9961-9964.

(22) Au, S.-M.; Huang, J.-S.; Yu, W.-Y.; Fung, W.-H.; Che, C.-M., *J. Am. Chem. Soc.* **1999,** *121*, 9120-9132.

(23) Doyle, M. P.; Duffy, R.; Ratnikov, M.; Zhou, L., *Chem. Rev.* **2010,** *110*, 704-724.

(24) Asensio, G.; Caballero, A.; Despagnet-Ayoub, E.; Diaz-Requejo, M. M.; Diaz-Rodriguez, A.; Gonzalez-Nunez, M. E.; Mello, R.; Munoz, B. K.; Ojo, W. S.; Etienne, M.; Perez, P. J., *Science* **2011,** *332*, 835-838.

(25) Gol'dshleger, N. F.; Tyabin, M. B.; Shilov, A. E.; Shteinman, A. A., *Zh. Fiz. Khim. (Engl. Transl.)* **1969,** *43*, 1222.

(26) Bhalla, G.; Mironov, O.; Jones, C. J.; Tenn III, W. J.; Nakamura, S.; Periana, R. A., *Handbook of C-H Transformations*. Wiley-VCH: 2005; Vol. 2, p 529-542.

(27) Labinger, J. A.; Weinberg, D. R.; Bercaw, J. E., *Organometallics* **2007,** *26*, 167-172.

(28) Zhong, H. A.; Labinger, J. A.; Bercaw, J. E., *J. Am. Chem. Soc.* **2002,** *124*, 1378-1399.

(29) Conley, B. L.; Ganesh, S. K.; Gonzales, J. M.; Tenn, W. J.; Young, K. J. H.; Oxgaard, J.; Goddard, W. A.; Periana, R. A., *J. Am. Chem. Soc.* **2006,** *128*, 9018-9019.

(30) Tenn, I., W. J.; Young, K. J. H.; Bhalla, G.; Oxgaard, J.; Goddard III, W. A.; Periana, R. A., *J. Am. Chem. Soc.* **2005,** *127*, 14172-14173.

(31) Feng, Y.; Lail, M.; Barakat, K. A.; Cundari, T. R.; Gunnoe, T. B.; Petersen, J. L., *J. Am. Chem. Soc.* **2005,** *127*, 14174-14175.

(32) Brown, S. N.; Mayer, J. M., *J. Am. Chem. Soc.* **1996,** *118*, 12119-12133.

(33) Brown, S. N.; Mayer, J. M., *Organometallics* **1995,** *14*, 2951-2960.

(34) Koo, K. M.; Hillhouse, G. L.; Rheingold, A. L., *Organometallics* **1995,** *14*, 456-460.

(35) Matsunaga, P. T.; Hillhouse, G. L.; Rheingold, A. L., *J. Am. Chem. Soc.* **1993,** *115*, 2075-2077.

(36) Matsunaga, P. T.; Mavropoulos, J. C.; Hillhouse, G. L., *Polyhedron* **1995,** *14*, 175-185.

(37) Alsters, P. L.; Teunissen, H. T.; Boersma, J.; Spek, A. L.; Vankoten, G., *Organometallics* **1993,** *12*, 4691-4696.

(38) Kamaraj, K.; Bandyopadhyay, D., *Organometallics* **1999,** *18*, 438-446.

(39) AbuOmar, M. M.; Hansen, P. J.; Espenson, J. H., *J. Am. Chem. Soc.* **1996,** *118*, 4966-4974.

(40) Gonzales, J. M.; Distasio, R.; Periana, R. A.; Goddard, W. A.; Oxgaard, J., *J. Am. Chem. Soc.* **2007,** *129*, 15794-15804.

(41) Periana, R. A.; Bischof, S. M.; Cheng, M. J.; Nielsen, R. J.; Gunnoe, T. B.; Goddard, W. A., *Organometallics* **2011,** *30*, 2079-2082.

(42) Feng, Y.; Lail, M.; Foley, N. A.; Gunnoe, T. B.; Barakat, K. A.; Cundari, T. R.; Petersen, J. L., *J. Am. Chem. Soc.* **2006,** *128*, 7982-7994.

(43) Tenn, I., W. J.; Young, K. J. H.; Oxgaard, J.; Nielson, R. J.; Goddard III, W. A.; Periana, R. A., *Organometallics* **2006,** *25*, 5173-5175.

(44) Kloek, S. M.; Heinekey, D. M.; Goldberg, K. I., *Angew. Chem., Int. Ed.* **2007,** *46*, 4736-4738.

(45) Hanson, S. K.; Heinekey, D. M.; Goldberg, K. I., *Organometallics* **2008,** *27*, 1454-1463.

(46) Bercaw, J. E.; Hazari, N.; Labinger, J. A., *Organometallics* **2009,** *28*, 5489-5492.

(47) Cundari, T. R.; Grimes, T. V.; Gunnoe, T. B., *J. Am. Chem. Soc.* **2007,** *129*, 13172-13182.

(48) Ess, D. H.; Gunnoe, T. B.; Cundari, T. R.; Goddard III, W. A.; Periana, R. A., *Organometallics* **2010,** *29*, 6801-6815.

(49) Figg, T. M.; Cundari, T. R.; Gunnoe, T. G., *Organometallics* **2011,** *30*, 3779-3785.

(50) Frisch, M. J.; al, e. *Gaussian 09*, Gaussian Inc.: Wallingford, CT, 2009.

(51) Lee, C.; Yang, W.; Parr, R. G., *Phys. Rev., B* **1988,** *37*, 785-789.

(52) Becke, A. D., *J. Phys. Chem.* **1988,** *38*, 3098.

(53) Stevens, W. J.; Basch, H.; Krauss, M., *J. Chem. Phys.* **1984,** *81*, 6026-6033.

(54) Cundari, T. R.; Stevens, W. J., *J. Chem. Phys.* **1993,** *98*, 5555.

(55) Stephens, P. J.; Devlin, F. J.; Chabalowski, C. F.; Frisch, M. J., *J. Phys. Chem.* **1994,** *98*, 11623-11627.

(56) Cossi, M.; Rega, N.; Scalmani, G.; Barone, V., *J. Comput. Chem.* **2003,** *24*, 669-681.

(57) Reyes, L.; Castro, M.; Cruz, J.; Rubio, M., *J. Phys. Chem. A* **2005,** *109*, 3383-3390.

(58) Reyes, L.; Alvarez-Idaboy, J. R.; Mora-Diez, N., *J. Phys. Org. Chem.* **2009,** *22*, 643-649.

(59) Renz, M.; Meunier, B., *Eur. J. Org. Chem.* **1999**, 737-750.

(60) Oxgaard, J.; Tenn, I., W. J.; Nielson, R. J.; Periana, R. A.; Goddard III, W. A., *Organometallics* **2007,** *26*, 1565-1567.

(61) Webb, J. R.; Pierpont, A. W.; Munro-Leighton, C.; Gunnoe, T. B.; Cundari, T. R.; Boyle, P. D., *J. Am. Chem. Soc.* **2010,** *132*, 4520-4521.

(62) Fulmer, G. R.; Muller, R. P.; Kemp, R. A.; Goldberg, K. I., *J. Am. Chem. Soc.* **2009,** *131*, 1346.

CHAPTER 5

A MECHANISTIC STUDY OF OXY-INSERTION INTO NICKEL–CARBON BONDS WITH NITROUS OXIDE*

5.1 Introduction

Oxy-insertion into metal–alkyl or metal–aryl bonds of middle to late transition metals to give alkoxide or aryloxide ligands is rarely observed. Brown and Mayer have reported alkyl migrations into metal–alkyl bonds with Re(VII) complexes.[1,2] Ison and coworkers have reported a Re(V) oxo complex that was shown to undergo oxy-insertion upon coordination of a CO ligand.[3] Periana and Goddard reported a reaction of methylrheniumtrioxide (MTO) in conjunction with external oxidants, such as, PhIO, H_2O_2 and IO_4^-. However, the oxy-insertion into the Re–Me bond of MTO to form a methoxide did not occur via an oxo-intermediate and is thus unlike the Re systems reported by Brown and Mayer.[4,5] The MTO systems were found to undergo concerted non-redox insertions akin to the Baeyer-Villiger oxidation (BV). Recently, our group has reported several computational studies involving organometallic Baeyer-Villiger (OMBV) reactions with four- and six-coordinate bipyridyl (bpy) complexes.[6,7] Computations showed the oxidant in a Pt(II) system showed to have a moderate ($\Delta\Delta G^{\ddagger} \sim 3 - 4$ kcal/mol) Hammett impact on the OMBV barrier heights.[6] A systematic study of the influence on coordination and metal identity for OMBV insertions was performed for Group 7 – 10 metals of the 3d, 4d, and 5d rows, which revealed that earlier, lower coordinate, 3d metals have lower barriers for OMBV insertions due to weaker metal–carbon bonds and more nucleophilic carbons in the alkyl transfer groups.[7]

---

* This chapter is presented in its entirety from T. M. Figg, and T. R. Cundari "A Mechanistic Study Of Oxy-Insertion Into Nickel □Carbon Bonds Wi
the American Chemical Society.

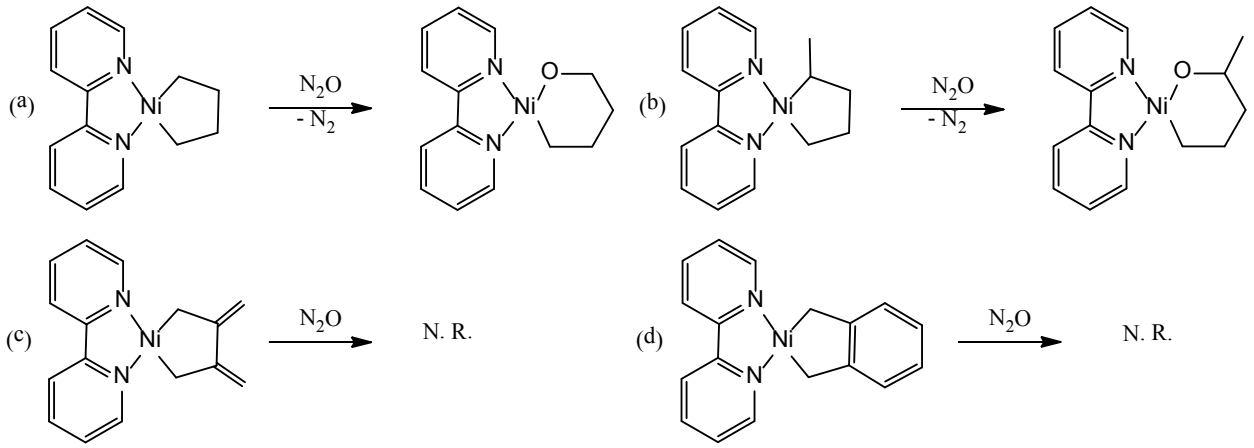

Figure 5.1. Synthesized nickel metallacycle complexes reacting with nitrous oxide to form the respective metal-alkoxide complexes; N.R. indicates that no reaction took place upon reaction with N_2O.

Hillhouse and coworkers have reported a series of nickel metallacycle complexes, which upon reaction with N_2O yield the respective metal alkoxide complexes. For example, reacting $(PMe_3)_2Ni(\kappa^2\text{-}C,C\text{-}CH_2CMe_2\text{-}o\text{-}C_6H_4)$ with N_2O produces $[(PMe_3)Ni(\kappa^2\text{-}O,C\text{-}O\text{-}o\text{-}C_6H_4CMe_2CH_2)]_2$.[8-10] Examples involving bpy supporting ligation are displayed in Figure 5.1. Complexes (a) and (b) were found to do net oxy-insertion upon reaction with N_2O. However, the complexes in which the β-carbon in the alkyl ring is sp^2-hybridized (Figure 5.1 (c) and (d)) did not form alkoxides upon reaction with N_2O. The pathway for oxy-insertion was also uncertain, although regioselectivity was displayed when comparing complexes (a) and (b). The oxygen was found to insert into the more substituted carbon and Ni–aryl is preferred over Ni–alkyl much like the classical BV oxidation.[11] To our knowledge, the aforementioned nickel complexes are the only examples of 3d metals undergoing net oxy-insertion. Thus, understanding this reaction could pave the way for future design of catalysts for selective partial hydrocarbon oxidation using Earth-abundant 3d metals.

An interesting characteristic of nitrous oxide as an oxidant in transition metal chemistry is its various binding possibilities onto transition metal centers. Much effort has been put into

understanding the chemistry behind N_2O and its interactions with transition metals.[12,13] Possible linkage isomers are given in Figure 5.2. In this paper we aim to elucidate the possible pathways for oxy-insertion into nickel–carbon bonds with N_2O. Equipped with a better understanding of the fundamental chemistry behind OMBV reactions with 3d metals could guide future experimental efforts at catalyst design.

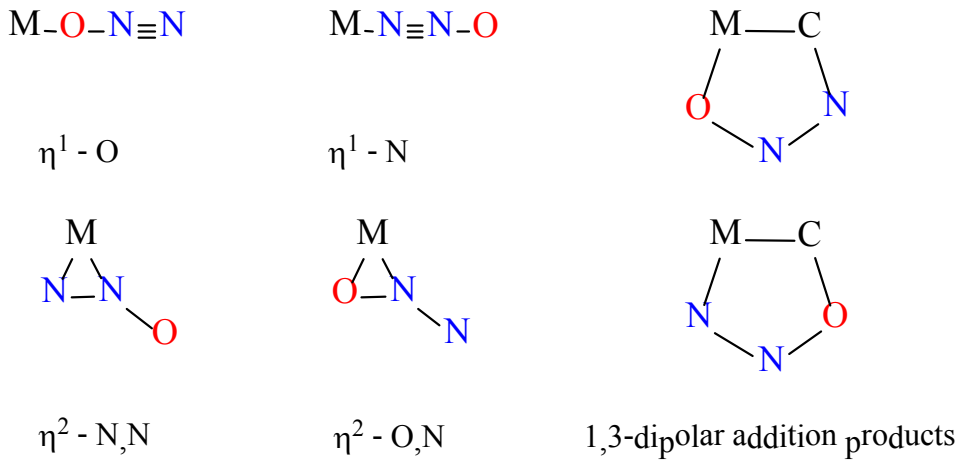

Figure 5.2. Possible linkage isomers for the interaction of N_2O with a metal alkyl complex.

5.2 Computational Methods

Density functional theory (DFT) was utilized to elucidate the mechanistic details pertaining to the oxy-insertion of various Ni complexes. The Gaussian 09 software package[14] was used for geometry optimizations and vibrational frequency calculations. Minima and transition states were distinguished by the presence of 0 or 1 imaginary frequencies, respectively, obtained from the calculated energy Hessians. The hybrid functionals B3LYP[15,16] and M06[17] were compared for a majority of the systems discussed; however, the differences in the geometries and energetics were small (< 5 kcal/mol). Thus, the reactions presented will be the results obtained with the B3LYP functional in conjunction with the all-electron basis set, 6-31+G(d). All electrons are modeled explicitly with added diffuse and polarization functions to non-hydrogen atoms. All energetics are reported as free energies in kcal/mol and calculated

under standard conditions (1 atm and 298.15 K). Singlet and triplet spin states were calculated for each stationary point.

5.3 Results and Discussion

Binding of nitrous oxide to bpyNi(II)(cyclo-$(CH_2)_4$) in a η^1-O or η^1-N fashion yielded a weakly bound adduct, Figure 5.3, with a $\Delta G \approx 4.6$ kcal/mol compared to the separated reactants. Adding N_2O across the nickel-alkyl bond in a [2+2] fashion yields the two covalently bound isomers, **2+2a** and **2+2b** shown in Figure 5.3. The **2+2a** isomer, in which the oxygen atom is in proximity to the nickel center is found to be the lower energy isomer, $\Delta G = 0.2$ kcal/mol, by ~ 9.8 kcal/mol compared to the **2+2b** addition product. The free energy difference could be attributed to the stabilization of the dangling oxygen atom by the nickel center (Ni-O = 2.6 Å in **2+2a**).[13]

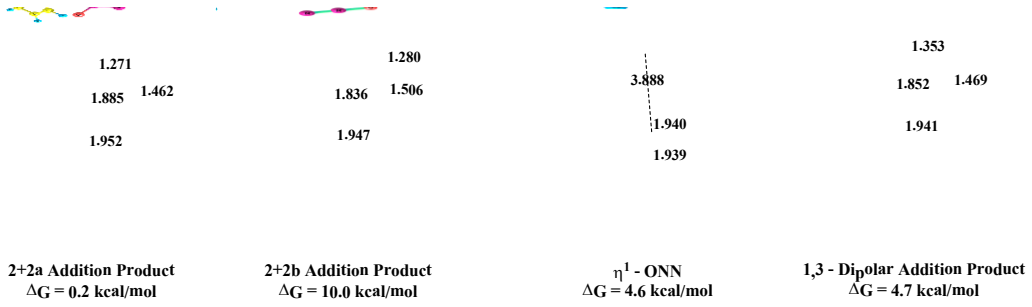

Figure 5.3. Calculated lowest energy isomers for the addition of N_2O onto bpyNi^{II}(cyclo-$(CH_2)_4$). Free energies are relative to separated reactants. Bond lengths are given in Å.

Two linkage isomers arising from the 1,3-dipolar addition of N_2O into the nickel carbon bond were calculated. The 1,3-dipolar addition product in which the oxygen is connected to the carbon (Ni-N-N-O-C cycle) was found to be unstable. The 1,3-dipolar addition product in which the oxygen is connected to the nickel atom (Ni-O-N-N-C cycle) was found to have a $\Delta G = 4.7$ kcal/mol, Figure 5.3. Calculations investigating the possibility of κ^1-bpy conformations resulted in higher energies and will not be discussed further. Singlet and triplet spin states were

investigated for each isomer in Figure 5.3; however, in each case the singlet was found to be lower in energy.

5.3.1 Proposed Reaction Pathway

The free nickel metallacycle, [**1**] in Figure 5.4, was found to possess a singlet ground state with a square planar geometry. Given the possible binding isomers of N_2O just discussed one can envision several pathways for the formation of the nickel alkoxide product, [**6**]. One possible pathway consists of a 1,3-dipolar addition of N_2O to a Ni–C bond followed by a [2+2] release of N_2 to form the Ni(II)-alkoxide product.

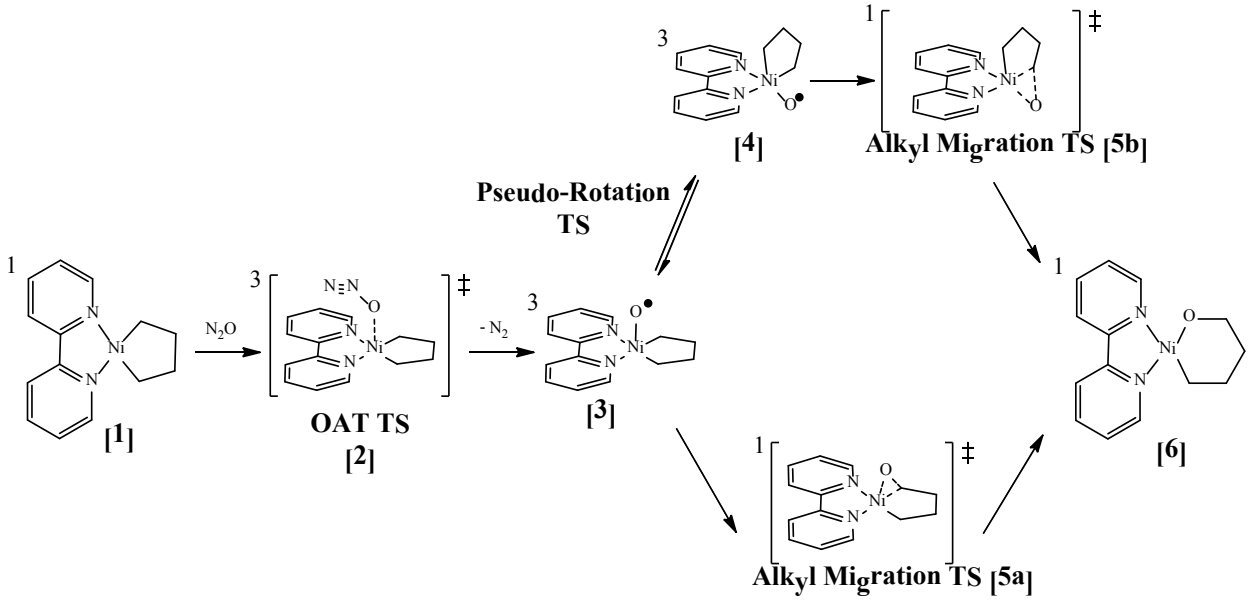

Figure 5.4. Proposed mechanisms of the reaction of N_2O with complex [**1**] to form the respective nickel-alkoxide complex. Spin states are given as superscripts in the upper left corner of the respective geometries. OAT TS = oxygen atom transfer transition state.

However, this pathway yielded very large calculated barriers, $\Delta G^{\ddagger}$ = 44.1 and 71.0 kcal/mol for the initial 1,3-dipolar addition and subsequent 2+2 elimination of N_2, respectively. Thus, the large barriers suggest that this pathway is improbable and it will not be discussed further.

Another possible pathway, Figure 5.4, consists of attack in a κ^1 fashion through the oxygen atom of N_2O onto the nickel center forming a square pyramidal oxo complex, [**3**],

coupled with expulsion of N_2. The B3LYP/6-31+G(d) OAT (oxygen atom transfer) transition state geometry, [**2**], in the triplet spin state is given in Figure 5.5, which yields a calculated barrier, $\Delta G_{OAT}^{\ddagger}$, of 29.4 kcal/mol relative to N_2O plus [**1**] and which is exergonic by 8.5 kcal/mol upon formation of the oxo complex, [**3**]. The oxo complex [**3**] is predicted to have a triplet ground state and from here two plausible routes for oxy-insertion are (1) alkyl migration or insertion, [**5a**], of the apical oxo ligand of [**3**] into the Ni–CH_2 bond of the ring, or (2) pseudorotation of the [**3**] to form a pseudo trigonal bipyramidal oxo complex, [**4**], (Figure 5.4) followed by oxo insertion into the nickel-alkyl bond. The triplet oxo complex [**4**] is found to have a trigonal bipyramidal (TBP5) geometry that is 6.1 kcal/mol more stable than the triplet oxo complex with a square pyramidal geometry (SP5), [**3**]. The extra stability could be attributed to the shortening of the oxo bond in complex [**4**], from 1.83 to 1.75 Å (~ 2.2%). Oxo insertion into the metal carbon bond is found to be facile with an effective transition state barrier, $\Delta G_{eff}^{\ddagger}$, of 6.2 kcal/mol for [**4**] → [**5b**]. The resulting product is a singlet nickel-alkoxide [**6**], which is calculated to be exergonic by 67.0 kcal/mol relative to the separated reactants **[1]**.

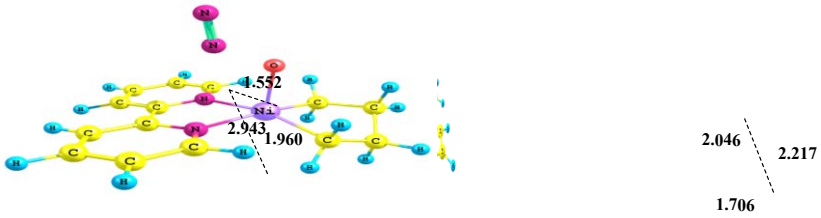

Figure 5.5. Calculated transition state geometries for oxygen atom transfer by nitrous oxide **[2]** and alkyl migration into a nickel-carbon bond **[5b]**. Bond lengths in Å.

5.3.2 Pseudorotation from Square Pyramidal to Trigonal Bipyramidal

The pseudorotation transition state connecting [**3**] and [**4**] was not isolated, despite numerous attempts; however, pseudorotation from SP5 to TBP would be expected to be facile

with an oxo ligand.[18] The isomerization of [**3**] to [**4**] is thermodynamically favored by 6.1 kcal/mol. The HOMO for a d^6 complex with SP5 geometry (e in Figure 5.6) would be lower compared to the HOMO for a TBP structure (e' in Figure 5.6) and thus the SP5 would be the preferred orientation. However, the predicted barrier for a pseudorotation to TBP from a SP5 geometry with an apical oxo ligand would be low for a d^6 complex along the "b_2 pathway" from the Walsh diagram in Figure 5.6. The orbital energy differences between the e" term and e' term will be reduced due to the π-donor effects of the oxo ligands upon the d_{xz}/d_{yz} orbitals in the SP5 geometry likely making the b_2 pathway in Figure 5.6 even more accessible than for σ-only ligands.

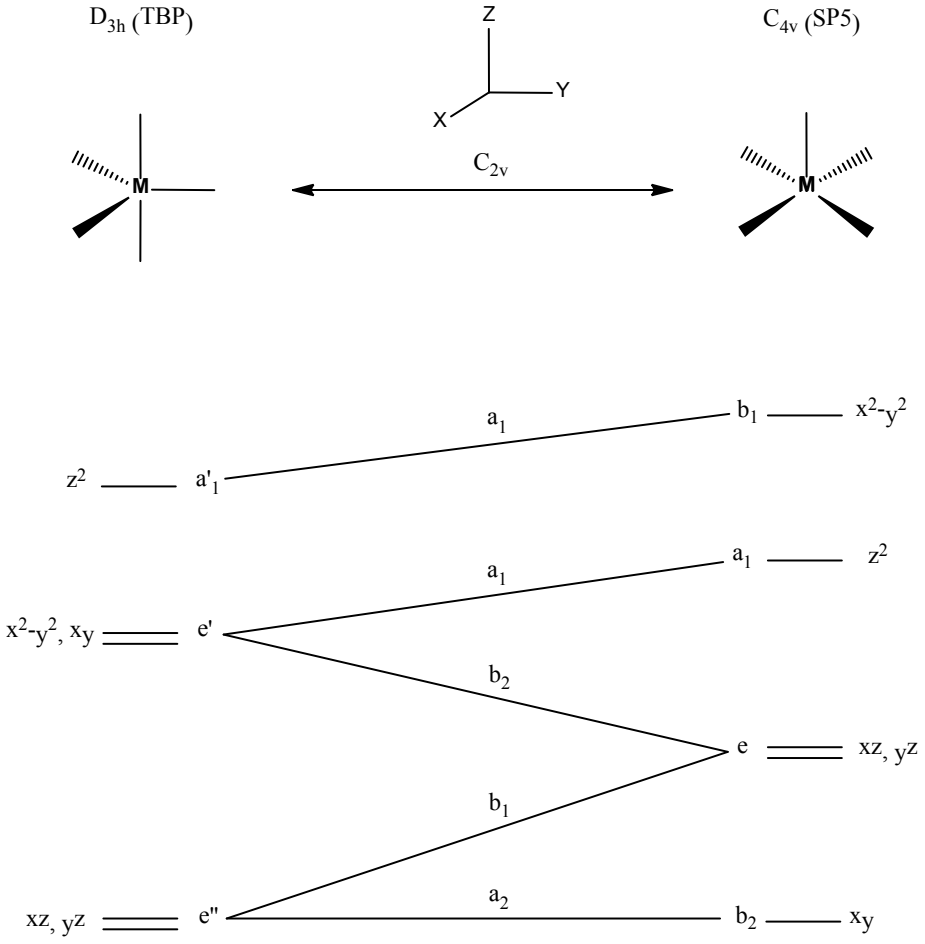

Figure 5.6. Orbital correlation diagram for metal d-orbitals which connect trigonal bipyramidal and square pyramidal geometries. Adapted from reference 18.

The geometries for the oxo complexes [**3**] and [**4**] are given below in Figure 5.7.

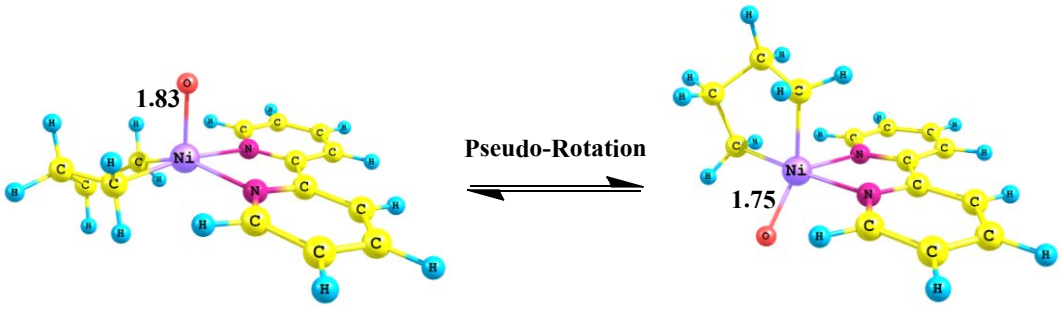

Figure 5.7. Calculated Ni^{III}-oxyl geometries in the triplet ground states. Bond lengths in Å.

The extra stability of the TBP structure may be attributed to the HOMO orbitals (xz and yz) of the SP5 attaining more π-antibonding character, reducing the bond order of the nickel-oxo bond, and resulting in a bond length of 1.83 Å. Switching to a TBP geometry alleviates these π-antibonding interactions, thus yielding a stronger metal-oxo bond, which is evident in the 1.75 Å metal-oxo bond length. Note that the spin density on the oxygen atoms of [**3**] and [**4**] are both ~1.0 e^-, suggesting that these species are best thought of as Ni(III)–oxyl (*i.e.*, $O^{\bullet -}$) entities.

Oxy-insertion into the nickel-alkyl carbon of [**1**], Figure 5.8 (red), has been experimentally shown to occur at 50 °C in 48 hours.[10] However, a complex in which the β-carbon is sp^2-hybridized, such as the examples given in Figure 5.8 (blue and green), does not yield oxy-insertion products and leads to decomposition at elevated temperatures. Calculations revealed that for each complex in Figure 5.8 the rate-determining step was the OAT transition state. There exists a spin "flip" from the singlet ground state for complex [**1**] to the triplet surface in the transition state [**2**] to form the Ni(III)–oxyl intermediates [**3**] and [**4**]. Another spin state flip occurs from the triplet oxo-intermediate to the singlet oxy-insertion transition state [**5b**] forming the alkoxide product [**6**]. The free energy barrier to oxo formation for parent complex [**1**] is calculated to be 2 - 3 kcal/mol lower than the derivatives with sp^2-hybridized carbons in

the β-positions. As 1 kcal/mol translates into approximately one order of magnitude for the rate constant according to Arrhenius theory the computations are consistent with the experimental reactivity trends.

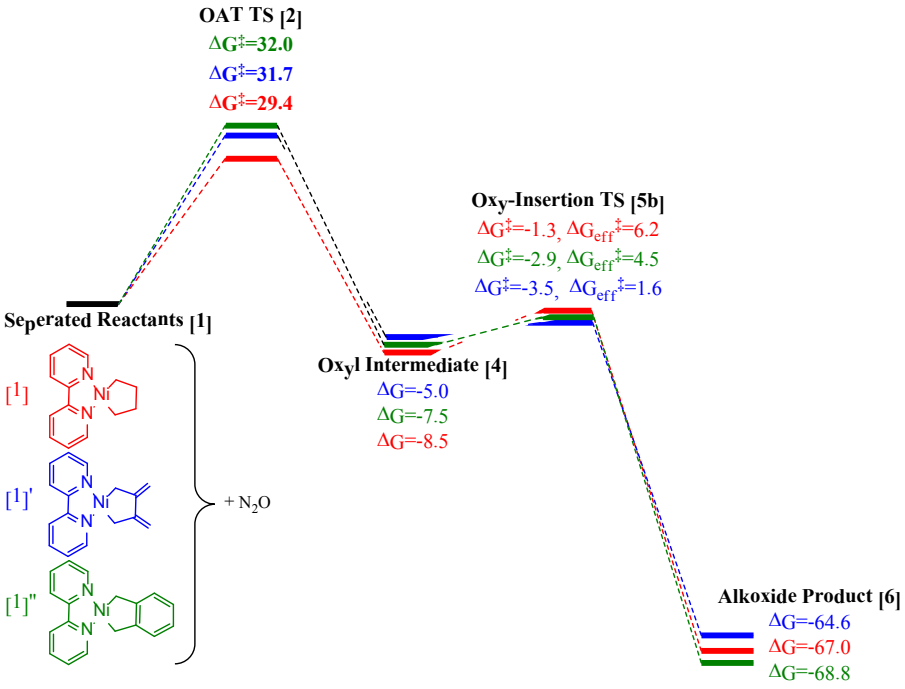

Figure 5.8. Comparison of proposed oxy-insertion pathway between the sp^3-hybridized bpyNi^{II}(cyclo-$(CH_2)_4$) system [**1**] and related compounds with sp^2-hybridized β-carbons ([**1**]' and [**1**]").

5.3.3 Regioselectivity of Oxy-insertion

Oxy-insertion into the nickel–alkyl bond was shown to have a certain degree of selectivity. For instance, Hillhouse *et al.* found that the oxygen atom from N_2O would selectively insert into the more substituted nickel-carbon bond (*i.e.*, secondary over primary).[10] A methyl, primary, and secondary nickel system were studied in order to elucidate selectivity trends. The three systems studied are given in Figure 5.9. The barriers for the alkyl migration transition states akin to [**5b**] were calculated to be 9.1, 6.2, and 2.7 kcal/mol for methyl, primary, and secondary substituted alkyls. The insertion for this organometallic system follows the same pattern as expected for organic Baeyer-Villiger oxidation. Note, however, these reactions are

best thought of as two-step oxy-insertions with initial Ni(III)-oxyl formation followed by alkyl migration to the oxyl ligand.

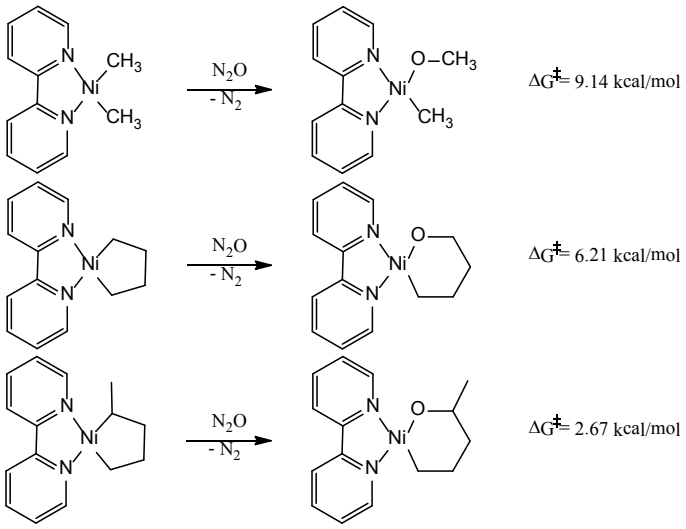

Figure 5.9. Oxy-insertion selectivity patterns for (bpy)Ni(alkyl) systems. Barriers for alkyl migration are given on the right.

5.3.4 Connection between BV and Alkyl Migrations

A Baeyer-Villiger-type reaction involves a single step in which the metal-carbon bond is cleaved while the oxygen-carbon bond are formed in concert, Figure 5.10. While the Hillhouse system shows selectivity trends reminiscent of BV-type insertions, the simulations indicate that the nickel systems under study first form a Ni(III)–oxyl intermediate before oxy-insertion to make the alkoxide. Repeated attempts to isolate a Baeyer-Villiger transition state led to the oxy-insertion transition state [**5b**].

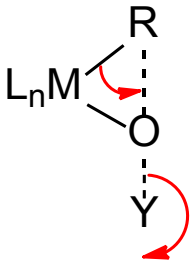

Figure 5.10. Organometallic Baeyer-Villiger transition state where R = alkyl or aryl transfer group, YO = oxidant, and L_n = ancillary ligand.

This may be attributed to the "good" leaving group capacity of N_2 generated by the N_2O oxidant. There exists a connection in oxy-insertion transformations, a BV or non-redox pathway or an oxo (redox) pathway, which can be thought to lie on a continuum that is linked to the identity of the oxidant (YO) and the degree of participation of the leaving group (Y) in the TS active site, Figure 5.11.

Figure 5.11. Proposed connection between Baeyer-Villiger and oxo pathways for oxy-insertion (MR + [O] → MOR) where M = metal, R = alkyl or aryl transfer group, Y = leaving group, and L_n = ancillary ligand.

In the present case N_2O affords an excellent leaving group N_2 and thus does not directly participate in the oxy-insertion. Hence, N_2O may be expected to move the oxy-insertion TS toward the oxo end of the continuum stylized in Figure 5.11. On the other side of the continuum there exists a BV-type transformation in which the leaving group directly participates in the oxy-insertion transition state.

To test this hypothesis, a "worse" leaving group compared to N_2 such as pyridine-N-oxide was utilized to test the link between leaving group capacity and the nature of oxy-insertion. Pyridine-N-oxide has been utilized in previous examples of oxy-insertion of the BV variety.[5] The transition state involving a κ^1-O OAT transition state afforded a much larger barrier, $\Delta G^{\ddagger} = 49.7$ kcal/mol and was found to be slightly endergonic compared to the separated reactants, $\Delta G = 10.0$ kcal/mol, consistent with the Hammond postulate and the weaker oxidizing potential of PyO versus N_2O.[19] Attempts to isolate a BV-type insertion TS for PyO led to an N-O oxidative addition transition state for which was found to have an even larger barrier, $\Delta G^{\ddagger} = 62.6$ kcal/mol.

The transition state geometries for the OAT and oxidative addition of pyridine-N-oxide to [**1**] are given in Figure 5.12.

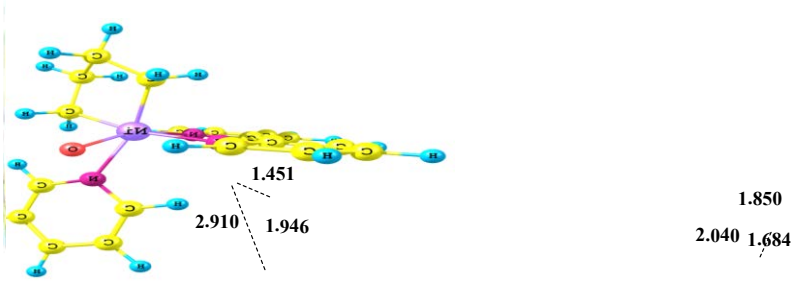

Figure 5.12. Oxyl formation transition states via an κ^1-O OATS (left) and oxidative addition (right) in the triplet spin states. Bond lengths are in Å.

5.4 Conclusions

DFT calculations were performed to elucidate the oxy-insertion mechanism of various Ni(II)–alkyl complexes with N_2O as oxidant. The complexes showed selectivity patterns for oxy-insertion upon the introduction of additional methyl groups to the α-carbon in the metallacycle ring that are similar to classic Baeyer-Villiger oxidations. However, unlike BV insertions, which are concerted non-redox transformations, the reaction was found to proceed through an oxo intermediate that is coupled with a formal $2e^-$ reduction (if the oxo ligand is considered as O^{2-}) of the nickel center. Note, however, analysis of the electronic structure implies that the "oxo" intermediates are best thought of as Ni(III)–oxyl (*i.e.*, $O^{\bullet -}$) entities.

The DFT-proposed pathway involved a two-step mechanism: (1) formation of a Ni(III)–oxyl intermediate, and (2) oxo insertion into the nickel carbon bond to form the alkoxide product. The rate-determining step was found to be the initial oxygen atom transfer with a barrier height of 29.4 kcal/mol for N_2O plus bpyNi(II)(cyclo-$(CH_2)_4$). Complexes that contain sp^2-

hybridized β-carbons within the metallacycle were found to not undergo net oxy-insertion experimentally. These complexes were calculated to have higher barriers (2 - 3 kcal/mol) compared to the systems that underwent oxy-insertion. Factors such as rigidity of the nickelacycle rings could also play a role in the outcome of this reaction. A key advantage of utilizing N_2O for these reactions is the large thermodynamic driving forces afforded by expulsion of N_2. Oxidants such as pyridine-N-oxide which afford "worse" leaving groups were found to have much higher barriers for oxo-formation due to a loss in the thermodynamic driving force.

5.5 References

(1) Brown, S. N.; Mayer, J. M., *J. Am. Chem. Soc.* **1996,** 118, 12119-12133.

(2) Brown, S. N.; Mayer, J. M., *Organometallics* **1995,** 14, 2951-2960.

(3) Smeltz, J. L.; Boyle, P. D.; Ison, E. A. *J. Am. Chem. Soc.* **2011**, 133, 13288-13291.

(4) Conley, B. L.; Ganesh, S. K.; Gonzales, J. M.; Tenn, W. J.; Young, K. J. H.; Oxgaard, J.; Goddard, W. A.; Periana, R. A., *J. Am. Chem. Soc.* **2006,** 128, 9018-9019.

(5) Gonzales, J. M.; Distasio, R.; Periana, R. A.; Goddard, W. A.; Oxgaard, J., *J. Am. Chem. Soc.* **2007,** 129, 15794-15804.

(6) Figg, T. M.; Cundari, T. R.; Gunnoe, T. B., *Organometallics* **2011**, 30, 3779-3785.

(7) Figg, T. M.; Webb, J. R.; Cundari, T. R.; Gunnoe, T. B., *J. Am. Chem. Soc.* **2012**, 134, 2332-2339.

(8) Koo, K. M.; Hillhouse, G. L.; Rheingold, A. L., *Organometallics* **1995,** *14*, 456-460.

(9) Matsunaga, P. T.; Hillhouse, G. L.; Rheingold, A. L., *J. Am. Chem. Soc.* **1993,** 115, 2075-2077.

(10) Matsunaga, P. T.; Mavropoulos, J. C.; Hillhouse, G. L., *Polyhedron* **1995,** 14, 175-185.

(11) Renz, M.; Meunier, B. *Eur. J. Org. Chem.* **1999**, 4, 737-750.

(12) Tolman, W. B., *Angew. Chem. Int. Ed.* **2010**, 49, 1018-1024.

(13) Yu, H.; Jia, G.; Lin, Z., *Organometallics* **2007**, 26, 6769-6777.

(14) Fisch, M. J. *et al.* Gaussian 09, Gaussian, Inc.: Wallingford, CT, **2009**.

(15) Becke, A. D. *J. Chem. Phys.* **1993**, 98, 1372– 1378.

(16) Becke, A. D. *J. Chem. Phys.* **1993**, 98, 5648– 5652.

(17) Zhao, Y.; Truhlar, D. G. *Theor. Chem. Acc.* **2008**, 120, 215-241.

(18) Holmes, R. R. *J. Am. Chem. Soc.* **1984**, 106, 3745-3750.

(19) Holm, R. H.; Donahue, J. P. *Polyhedron* **1993**, 12, 571-589.

CHAPTER 6

COMPUTATIONAL HAMMETT ANALYSIS OF REDOX BASED OXY-INSERTION BY PT(II) COMPLEXES*

6.1 Introduction

Recently, we reported a series of computational studies to better understand carbon-oxygen bond formation mediated by late transition metals.[1-3] A better understanding of oxygen atom transfer reactions involving transition metal-alkyls is critical to facilitate the design of selective catalytic cycles for alkane and arene functionalization to alcohols and phenols, respectively.[4,5] A firm theoretical underpinning is particularly essential, as experimentally characterized examples of middle to late (non-d^0) transition metal complexes undergoing oxy-insertion into metal-carbon bonds are very rare,[6-14] and mechanistic details rarer still. Among these examples, a handful of d^0 complexes (*i.e.*, $MeReO_3$ (MTO), $PhReO_3$ (PTO), and $MeTaCp^*_2$) have been shown to undergo a concerted O-atom transfer akin to the Baeyer-Villiger (BV) oxidation upon reaction with an external oxidant (YO).[11-13] A prototypical example of an organometallic Baeyer-Villiger (OMBV) reaction pathway is depicted in Figure 6.1.

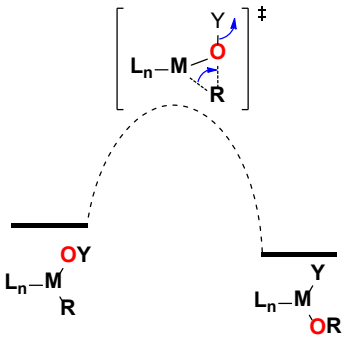

Figure 6.1. Protypical OMBV rearrangement (R = alkyl or aryl, Y = leaving group of the YO oxidant, and L_n = ancillary ligand) from a metallo-Criegee intermediate (MCI) to an alkoxide or aryloxide product.

*This chapter is presented in its entirety from T. M. Figg, and T. R. Cundari "Computational Hammett Analysis of Redox Based Oxy-Insertion By Pt(II) Complexes" Dalton Trans., 2013, 42, 4114 with permission from the Royal Society of Chemistry.

To test the possibility of extending BV-type reactions to other d-counts, calculations surveying Group 7 –10 metals and the 3d, 4d, and 5d congeners within each group were carried out. The calculations suggested that oxy-insertion with late-metals through a BV-type mechanism would be feasible for 3d metals.[2] This trend arose primarily due to weaker metal–carbon bonds and a more nucleophilic nature on the migrating methyl. Hillhouse *et al.* reported examples of Ni d^8 systems undergoing net oxy-insertion into nickel–carbon bonds using N_2O as the oxidant.[14,15]

While no mechanism was proposed, the reaction showed similar regioselectivity characteristic of a BV mechanism. However, when this reaction was probed computationally, the reaction was proposed to go through a Ni(III)–oxyl intermediate followed by alkyl migration onto the oxyl ($O^{\bullet-}$) ligand.[3] Oxygen atom transfer to palladium–carbon bonds have also been reported for several Pd(II) systems. These reactions were proposed to form Pd(IV)–oxo complexes prior to aryl migration, which forms the aryloxide product. Experimental evidence for the formation of Pd(IV)–oxo (or Pd(III)–oxyl) intermediates has not, to our knowledge, been reported.[8,9] Milstein and coworkers isolated and structurally characterized a Pt(IV)–oxo complex. DFT studies by Martin and coworkers elucidated the terminal oxo bonding environment and various key interactions in oxygen insertion mechanisms into Pt–P bonds.[16,17] Thus, current computational and experimental evidence implies formation of an oxo/oxyl reactive intermediate for late metal complexes within the Group 10 family with a d^8 electronic configuration.

Recently, we reported a Hammett analysis on a $[(bpy)Pt(Ph)(PyO)]^+$ complex undergoing a BV-type insertion of an oxygen atom into a Pt–Ph bond using pyridine-N-oxide (PyO) as the external oxidant.[1] Once the oxidant was bound to the platinum(II) center, forming the MCI, the

oxygen atom inserted in a concerted, non-redox fashion. The electronic impact was modeled by placing electron-donating (NMe_2) and electron-withdrawing (NO_2) groups in the *para* positions of the phenyl, pyridinyl, and bipyridyl ligands. The calculations suggested the phenyl migrating group has the largest electronic impact ($\Delta\Delta G$ = -12.0 kcal/mol) upon the BV reaction, where $\Delta\Delta G^{\ddagger} = (\Delta G_{NMe2} - \Delta G_{NO2})$, and the rate was accelerated by the electron-donating group. The electronic impact of the migrating group was in agreement with previous studies on d^0 MTO and organic BV reactions.[18-21] The oxidant (PyO) had a milder, albeit non-negligible, impact ($\Delta\Delta G$ = +4.2 kcal/mol) on BV oxy-insertion and the rate was accelerated by the presence of an electron-withdrawing group. The supporting bipyridyl ligand had almost no impact ($\Delta\Delta G$ = +0.4 kcal/mol) on this OMBV system.[1] The aforementioned Pt^{II} Hammett results for Bayer-Villiger oxy-insertion coincided with similar theoretical studies of organic BV oxidations.[18-20]

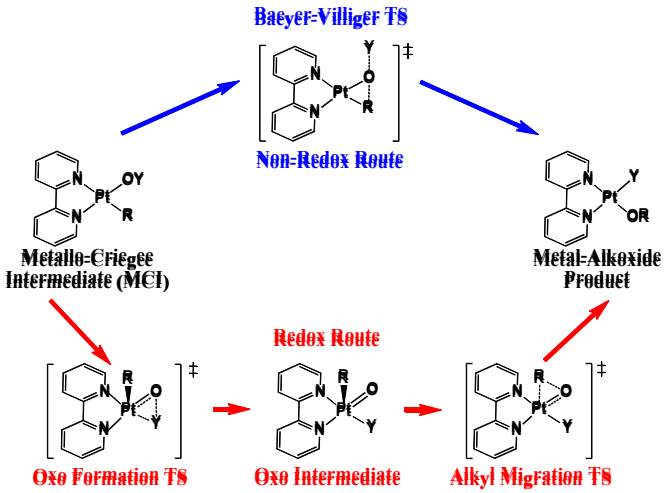

Figure 6.2. A comparison between the Baeyer-Villiger (blue) and the two step redox pathway (red) (R = alkyl or aryl migrating group and Y = leaving group component of the oxidant).

Further calculations comparing these two oxy-insertion pathways, the BV and aryl migration from an oxo-intermediate (Figure 6.2), suggested an important conceptual connection between the two transition states, which were linked in a structural sense to the identity of the external

oxidant for d^6 and d^8 complexes.[3] It was proposed that oxidants that afford "better" leaving groups (Y) resulted in more "oxo-like" transition states and "worse" leaving groups yielded more "BV-like" transition states, Figure 6.3.[3] For example, if N_2O was utilized as an external oxidant, the transition state geometry was pushed toward the "oxo-like" extreme and conversely if PyO is used, the geometry was pushed toward the "BV-like" transition state extreme.[3]

Figure 6.3. Proposed connection between a "BV-like" and an "oxo-like" transition state geometry (R = alkyl or aryl migrating group and Y = leaving group component of the YO oxidant).

In the present study we return to the $[(bpy)Pt(Ph)(PyO)]^+$ MCI complex focusing on the formation of a Pt(IV)–oxo intermediate followed by oxygen insertion into the Pt–aryl bond to form the Pt–aryloxide product. Electron-donating (EDG) and electron-withdrawing groups (EWG) were placed in both the *meta* and *para* positions of the phenyl (R), 4- and 3- positions of the pyridine (Y), and the 4,4'- and 5,5'- positions of the bipyridyl supporting ligand to assess inductive and resonance effects. Herein, we report the results of a computational Hammett analysis of reaction (6.1), where R = *p*-X-C_6H_4, *m*-X-C_6H_4; Y = 4-X-pyridine, 3-X-pyridine; ^{X}bpy = 4,4'-X-bpy or 5,5'-X-bpy; X = NO_2, H, OMe, NMe_2. Previous studies in our group and other groups have shown that a small selection of strong EDG and EWG such as NMe_2 and NO_2 have a significant enough distinction within their Hammett sigma values and relative enthalpies to delineate crucial electronic factors in catalytic reactions.[1,21,22]

$$[(^{X}bpy)Pt^{II}(R)(OY)]^{+} \rightarrow [(^{X}bpy)Pt^{IV}(R)(O)(Y)]^{+} \rightarrow [(^{X}bpy)Pt^{II}(OR)(Y)]^{+} \quad (6.1)$$

MCI **Oxo Intermediate** **Alkoxide**

The goal of this research is to better understand the electronic factors governing a redox-based, oxo-mediated oxy-insertion pathway and to compare and contrast with the non-redox BV-type mechanism previously reported.[1] For the sake of brevity, this account focuses on the aryl migration step given its relation to the BV-type transition state, Figure 6.2, and the conceptual advances that may result from better understanding the factors that control the position of oxy-insertion transition states in the continuum depicted in Figure 6.3.

6.2 Computational Methods

Density functional theory (DFT) was utilized to assess the electronic properties of the various platinum complexes. The Gaussian 09 software package[23] was used for geometry optimizations and vibrational frequency calculations. Minima and transition states (TS) were distinguished by the presence of 0 or 1 imaginary frequencies, respectively, obtained from the calculated energy Hessians. The TS for the aryl/oxo to aryloxide migration was characterized by the compression and expansion of the C_{ipso}-PtiO bond angle with one imaginary frequency, $\nu_i \sim 250\ cm^{-1}$. Intrinsic reaction coordinate (IRC) calculations were carried out to further characterize calculated transition states.

The hybrid functional B3LYP[24,25] was used in conjunction with the relativistic effective core potential (RECP) Stevens double-ζ valence basis sets with d functions added to the main group elements, *i.e.*, (CEP-31G(d)).[26-28] This level of theory was used in previous studies,[1] namely the Hammett analysis performed for the $[(bpy)Pt(Ph)(PyO)]^{+}$ complex undergoing BV-type (non-redox) oxy-insertions and was calibrated against the larger triple-ζ basis set (*i.e.*, CEP-121G(d) with no appreciable differences. Test CPCM[29,30] calculations in a continuum polar

solvent (THF, ε = 7.58) were carried out as a single point correction to the gas phase free energies, again yielding no appreciable differences. Thus, the calculations reported in this paper were modeled in the gas phase under standard conditions (1 atm and 298.15 K). The energetics are reported as free energies in kcal/mol and all systems discussed here were calculated to have a closed shell.

6.3 Results

The fully hydrogen substituted metallo-Criegee intermediate (MCI) $[(bpy)Pt(Ph)(OPy)]^+$ was defined as the baseline complex for the present computational Hammett studies. The electronic impact was measured by placing NO_2 (EWG), OMe, and NMe_2 (EDGs) in the *para* position of phenyl, the 4-position of pyridine, and 4,4'-positions of the bipyridyl supporting ligand of the Pt(II) moiety. To assess inductive effects, the same EWG and EDGs were placed in the *meta* position of phenyl, the 3-position of pyridine, and 5,5'-positions of bipyrdine.[c] The NO_2, OMe, and NMe_2 substituents with Hammett sigma values (σ_p and σ_m), listed in Table 6.1, were utilized to test extreme electronic donating/withdrawing situations for the three catalyst variables, *i.e.*, migrating group (R), leaving group of the oxygen delivery reagent (Y), and the ancillary ligand (L_n), Table 6.1.

Table 6.1. Hammett sigma values for the electronic impact of NO_2, OMe, and NMe_2 in the *meta* and *para* positions.[31]

Para Sigma Parameter (σ_p)	
NO_2	+0.78
OMe	-0.27
NMe_2	-0.83
Meta Sigma Parameter (σ_m)	
NO_2	+0.71
OMe	+0.12
NMe_2	-0.16

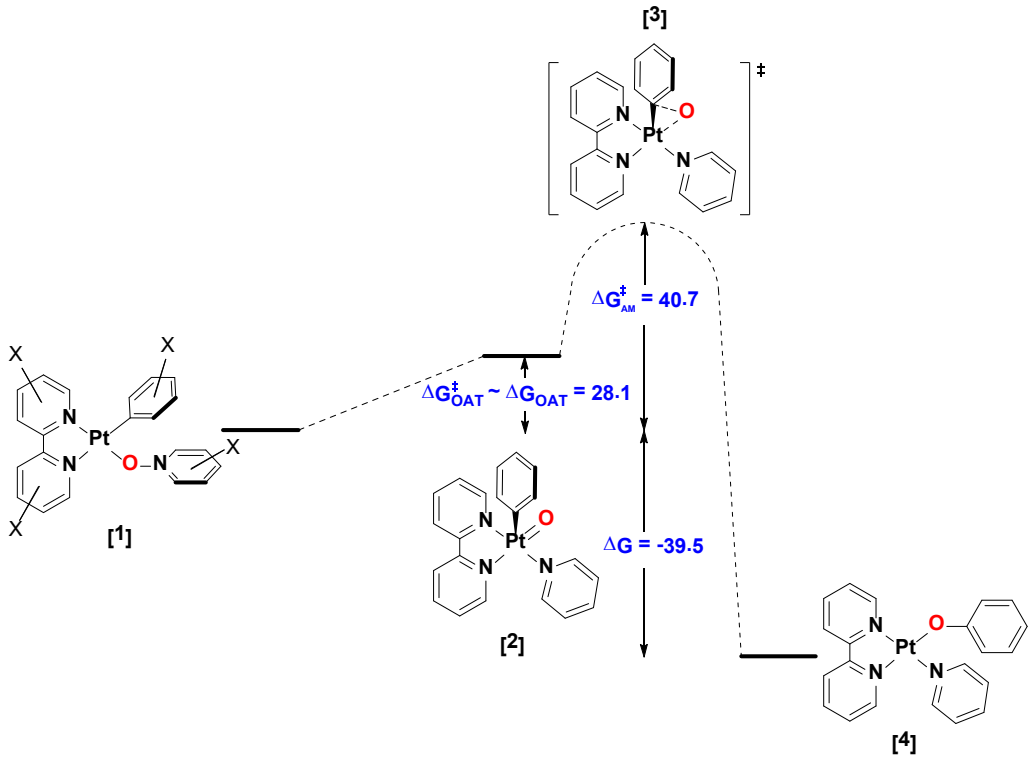

Figure 6.4. Baseline system for oxy-insertion into Pt(II)–Ph bonds utilizing PyO as the oxidant to form the phenoxide product. X represents the ligands in which the *meta* and *para* positions are altered (X = H for the baseline model). The free energy barriers and reaction free energies are given in kcal/mol.

6.3.1 Baseline System

The baseline system for the two-step oxy-insertion pathway (reaction 6.1), shown in Figure 6.4, in which all catalytic components (*i.e.*, Ph, Py, bpy) are fully decorated with hydrogens, will act as the point of reference for the various substituted moieties studied here. All energetics are reported with respect to the coordinatively and electronically saturated MCI, **[1]**.

The insertion reaction was calculated to be exergonic (ΔG = -39.5 kcal/mol) upon formation of the phenoxide product, [**4**]. Formation of the oxo (ΔG_{OAT}) is found to be endergonic by 28.1 kcal/mol.

[1]		[3]		[4]	
MCI		**Oxo**		**Aryloxide**	
Pt–Py	= 3.02	Pt–Py	= 2.10	Pt–Py	= 2.07
Pt–O	= 2.09	Pt–O	= 1.85	Pt–O	= 2.01
Pt–N1	= 2.04	Pt–N1	= 2.21	Pt–N1	= 2.07
Pt–N2	= 2.15	Pt–N2	= 2.06	Pt–N2	= 2.04
Ph–O	= 3.00	Ph–O	= 3.31	Ph–O	= 1.37
Pt–Ph	= 2.03	Pt–Ph	= 2.08		

Figure 6.5. Calculated B3LYP ground state geometries for the two-step oxy-insertion reaction. Bond lengths of the respective catalyst components are given in Å.

Repeated calculations and scans of the active site bond lengths and angles for the formation of the oxo intermediate ($\Delta G^{\ddagger}_{OAT}$) suggested a barrier approximately equal to the ΔG_{OAT}. Thus, the reverse reaction from **[2]** → **[1]** was essentially barrierless. Migration of the aryl **[3]** onto the oxo ligand yielded a barrier of height ($\Delta G_{AM}^{\ddagger}$) of 40.7 kcal/mol to form the product, **[4]**.

Aryl Migration Transition State

Bond Lengths (Å)

Pt–Py	~	2.07
Pt–O	~	1.92
Pt–N1	~	2.16
Pt–N2	~	2.05
Ph–O	~	2.28
Pt–Ph	~	2.16

Figure 6.6. Calculated B3LYP ground state geometry for the aryl migration transition state. The transition is denoted by a dotted line (**- - -**). Bond lengths of the respective catalyst components are given in Å.

A distorted square pyramidal structure with the oxo ligand bent out of the plane is in agreement to the Pt(IV)–oxo complex isolated by Milstein and coworkers.[17] The ground state geometries for the MCI, oxo intermediate and aryloxide product are given in Figure 6.5. The conversion of the Pt(IV)–oxo intermediate to the aryloxide involved an elongation and eventual cleavage of the Pt–Ph bond (Pt–C_{ipso} for the phenyl transfer group). This was evident as the

Pt–Ph bond was elongated from 2.08 to 2.16 Å (~3.9 %) in the aryl migration TS3, Figure 6.6. The Pt–O bond increased from the oxo bond length of 1.85 Å in the oxo intermediate to 1.92 Å (~3.8 %) in TS **4** and was further elongated to 2.01 Å upon forming the aryloxide product.

The Pt–Py bond length showed negligible change during the migratory insertion process. The Pt–N1 bond of the bpy ancillary ligand *trans* to the oxo ligand was shortened from 2.21 to 2.16 Å (~2.3 %) in the aryl migration TS and then to 2.07 Å upon formation of the product, Figure 6.5. This was most likely a result of the diminished trans influence of the oxygen-based ligand as the Pt–O bond length is elongated during aryl migration. The Ph–O bond length was decreased from 3.31 to 2.28 Å (~31 %) in the migration TS, finally resulting in a short bond length of 1.37 Å in the aryloxide product. The resulting exergonicity may be attributed to the formation of the strong phenyl-oxygen and metal-oxygen bonds.

6.3.2 Hammett Study on the Migrating Group "R"

The electronic impact of the phenyl migrating group (R = *p*-X-C_6H_4 or *m*-X-C_6H_4; X = NO_2, H, OMe, NMe_2) for the aryl migration to form a phenoxide product is highlighted in reaction (6.1); see the reaction coordinate in Figure 6.4. The transition states for the systems in which electron-withdrawing NO_2 and electron donating OMe and NMe_2 have been substituted in the phenyl *para* and *meta* positions were calculated. The orientations of the NO_2, OMe, and NMe_2 groups enable π-interactions with the aryl substituent allowing for resonance effects. Comparing the geometries to the parent system (Figure 6.4) placement of a *para* substituent in the phenyl ligand resulted in minimal changes in the bond lengths surrounding the platinum center (geometries given in Supporting Information). The free energy of reaction (**[1]** → **[4]**) also varied minimally, by ~ 1 kcal/mol for the various *para* substituted moieties.

The free energy of activation for the aryl migration of phenyl onto the Pt–oxo bond was calculated to **increase** by 2.6 kcal/mol from 40.7 to 43.1 kcal/mol upon placement of a *para*-NO_2 group on the migrating phenyl. Placing the OMe group into the *para* position of the phenyl migrating group **lowered** the barrier by 0.8 kcal/mol to 39.9 kcal/mol. Introduction of the NMe_2 group into the *para* position of the phenyl group **lowered** the barrier to 38.7 kcal/mol, resulting in a **decrease** of the free energy barrier by 2.0 kcal/mol. The electronic impact was estimated as $\Delta\Delta G^{p}_{R}{}^{\ddagger}$ = -4.4 kcal/mol. $\Delta\Delta G_{R}{}^{\ddagger}$ is defined as $\Delta G_{NMe2}{}^{\ddagger}$ - $\Delta G_{NO2}{}^{\ddagger}$. *The magnitude and sign of* $\Delta\Delta G^{p}_{R}{}^{\ddagger}$ *implies the migrating group had a mild impact upon the energetics and that more nucleophilic migrating groups result in an increase of the rate of the aryl migration reaction.*

Placing an NO_2 group into a *meta* position of the phenyl ring resulted in an **increase** of 2.7 kcal/mol to the free energy barrier from 40.7 to 43.4 kcal/mol. Once OMe was placed in the *meta* position the free energy barrier is **increased** by 0.3 kcal/mol to 41.0 kcal/mol. Substituting NMe_2 also resulted in a barrier **increase** of 0.3 kcal/mol to 41.0 kcal/mol. Thus, $\Delta\Delta G^{m}_{R}{}^{\ddagger}$ = -3.4 kcal/mol, from NMe_2 and NO_2, *suggesting a slightly milder meta (inductive) impact on the electronics compared to the para (resonance) substituted phenyl ligand moieties, but these are of the same sign.*

6.3.3 Electronic Impact of the Leaving Group "Y"

The electronic impact of the pyridine group (Y = 4-X-NC_5H_4 or 3-X-NC_5H_4; X = NO_2, H, OMe, NMe_2) was calculated with respect to the parent complex $[(bpy)Pt(Ph)(OPy)]^{+}$. The electron withdrawing (EWG) and electron donating groups (EDG) were attached to the 4-position of the pyridine ring in the aryl migration transition state. The $\Delta G_{AM}{}^{\ddagger}$ is **decreased** by 0.4 kcal/mol from 40.7 to 40.3 kcal/mol upon placing NO_2 in the 4-position of the pyridine ring. Introduction of OMe resulted in a **decrease** by 0.8 kcal/mol to 39.9 kcal/mol. Placement of

NMe_2 on the pyridine ring **decreased** the barrier by 0.2 kcal/mol to 40.5 kcal/mol. The electronic impact was thus calculated to be $\Delta\Delta G^{p}_{Y}{}^{\ddagger}$ = +0.6 kcal/mol. This relatively small impact, reasonably, resulted from the oxidant leaving group not being directly involved in the aryl migration transition state bond making/breaking. *Interestingly, the effect of the oxidant in the BV transformation was much more significant, $\Delta\Delta G^{BV}{}_{Y}{}^{\ddagger}$ = 4.2 kcal/mol,* and thus had moderate Hammett sensitivity.[1]

Substituting NO_2 into the 3-position of the pyridine ring **decreased** the free energy barrier by 1.0 kcal/mol from 40.7 to 39.7 kcal/mol. Placement of OMe and NMe_2 into the 3-position show similar results, both increased the barrier by 0.4 kcal/mol to 41.1 kcal/mol. The difference in free energy barriers result in a minimal impact on the electronics $\Delta\Delta G^{m}_{Y}{}^{\ddagger}$ = +1.4 with electron withdrawing groups on the oxidant accelerating the rate. *However, the Hammett impact of the 3-position was more significant than calculated for corresponding 4-X-PyO, implying that inductive effects are more important than resonance effects in the choice of this catalyst component.* However, the pyridine leaving group of the oxidant in the aryl migration transition state was essentially a spectator in terms of the electronic contributions with minimal rate accelerations proposed for electron withdrawing substituents on PyO-based oxidants.

6.3.4 Electronic Impact of the Ancillary Ligand "L_n"

The Hammett impact of the bipyridyl supporting ligand (^{X}bpy = 4,4'-X-bpy; X = NO_2, H, OMe, NMe_2) upon phenyl migration to the oxo ligand was calculated with respect to the parent MCI complex $[(bpy)Pt(Ph)(OPy)]^{+}$. Placement of NO_2 onto the 4,4'-positions of the bpy component **increased** the free energy barrier by 1.5 kcal/mol from 40.7 to 42.0 kcal/mol. Introduction of OMe to the 4,4'-positions of bpy **decreased** the barrier 39.7 kcal/mol reducing the free energy barrier by 1.0 kcal/mol. Placing NMe_2 on the rings reduced the barrier by 1.7

kcal/mol to 39.0 kcal/mol. *The calculated* $\Delta\Delta G^{4,4'}{}_{Ln}^{\ddagger}$ *= -3.0 kcal/mol, implied a minor electronic impact, albeit much greater in impact than observed for substituted bipyridine supporting ligands in OMBV reactions* for which the corresponding $\Delta\Delta G^{4,4'}{}_{Ln}^{\ddagger}$ was essentially zero.[1]

Mono-substituted moieties for the 5 or 5' were not explored due to the expected synthetic difficulties in introducing such single functionalities to bipyridine. Substituting NO_2 onto the 5,5'-positions of the bpy ancillary ligand **increased** the barrier by 0.4 kcal/mol from 40.7 to 42.1 kcal/mol. Placement of OMe into the 5,5' positions **increased** the barrier by 2.6 kcal/mol to 43.3 kcal/mol. Placing NMe_2 into the 5,5' positions decreased the barrier by 2.1 kcal/mol to 38.6 kcal/mol. The resulting calculated $\Delta\Delta G^{5,5'}{}_{Ln}^{\ddagger}$ = -3.5 kcal/mol, resulted in a minor electronic impact with the placement of EDG in the 4,4'- and 5,5'-positions improving the rates by approximately equal magnitudes. Thus, it may be beneficial to synthetically explore 4,4'- and 5,5'- *bis*-substituted complexes for late metal oxy-insertion, although it must be admitted such ligand sets are rare.

6.4 Discussion of Oxo-Mediated and OMBV Oxy-insertion

The resulting electronic impacts for the representative catalytic components (*i.e.*, R, Y, and L_n) are summarized in Figure 6.7 for the various substitution environments of the OMBV (from reference 1) and aryl migration transition states reported here.

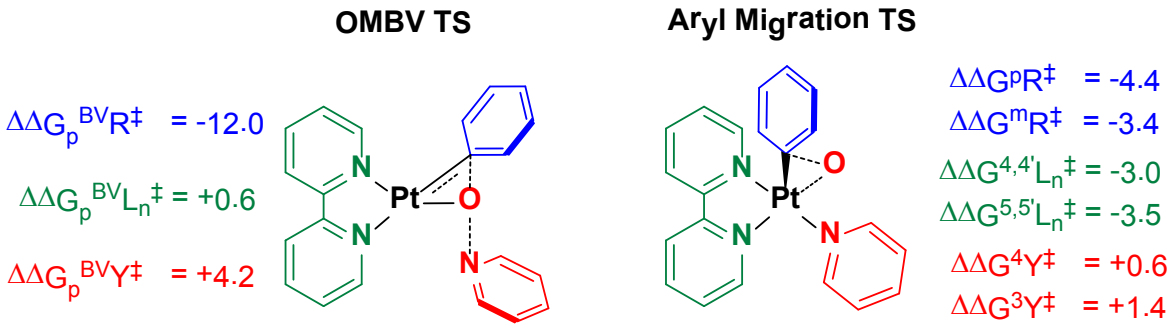

Figure 6.7. Electronic impact comparison for the various catalytic components (R, Y and L_n) for an OMBV and aryl migration transition state.

The phenyl migrating group (R) had the largest impact among the OMBV moieties ($\Delta\Delta G^{BV}{}_{R}^{\ddagger}$ = -12.0 kcal/mol) with a rate accelerated by the presence of electron donating groups in the *para* position. However, as the transition state was pushed toward an aryl migration description, see Figure 6.3, the electronic impact of R was greatly diminished from -12.0 to -4.4 kcal/mol for *para* substituted, and -3.4 kcal/mol for *meta*-R. While the rate was accelerated by more nucleophilic migrating groups for both OMBV and aryl migration transformations, *the OMBV transition state was approximately three times more sensitive in a free energy sense to changing the electronic environment as compared to the aryl migration TS*. In Hammett terms, this implies a reduced ρ value for aryl migration versus BV transition states, although the sign of □ was the same for both functionalization mechanisms.

The leaving group component (Y) of the external oxidant (*i.e.*, Y = Py from PyO) was calculated to have moderate impact within the OMBV transition state ($\Delta\Delta G^{BV}{}_{Y}^{\ddagger}$ = +4.2 kcal/mol). The positive sign of $\Delta\Delta G^{BV}{}_{Y}^{\ddagger}$ implies an increase of the rate by the presence of an electron withdrawing group. Once the TS was shifted toward the aryl migration extreme, Figure 6.3, the electronic impact of Y was diminished from +4.2 to +0.6 kcal/mol for the substitution at the 4-position of the pyridine ring and +1.4 for substitution at the 3-position. Thus, this indicated a *reduced magnitude and similar sign for the ρ value for 3- and 4-substituted Y within the aryl migration transition state and the para-substituted BV transition states, and a greater sensitivity to inductive over resonance effects for aryl-based oxidant leaving groups*.

The bipyridyl ancillary ligand (L_n) was shown to have almost no impact for the OMBV reaction[1] ($\Delta\Delta G^{BV}{}_{Ln}^{\ddagger}$ = +0.6 kcal/mol). In the aryl migration TSs, the L_n component was found to have a moderate $\Delta\Delta G_{Ln}^{\ddagger}$ of -3.0 and -3.5 kcal/mol for 4,4'- and 5,5'-substituted moieties, respectively. In Hammett terms, *the bpy component of the aryl migration transition state had a*

larger ρ value and a different sign compared to the related OMBV transition state. The OMBV transition state barrier was lowered by the presence of an electron-withdrawing group while the aryl migration barrier was lowered by the presence of electron-donating groups. Although the effects were moderate, one might propose Hammett-based ligand dependence experiments as being a possible mechanistic probe to discriminate the two pathways.

Hammett plots of the empirical sigma value (σ) versus the $\log(k_x/k_H)$ where k_x is the rate constant of the substituted complexes and k_H is the rate constant of the baseline complex decorated in hydrogens were constructed for the R, Y, and L_n components for aryl migration for the *para*- and *meta*- substituted moieties, (*i.e.*, R = *p*-X-C_6H_4 or *m*-X-C_6H_4; Y = 4-X-pyridine or 3-X-pyrdine; ^{X}bpy = 4,4'-X-bpy or 5,5'-X-bpy; X = NO_2, H, OMe, NMe_2) Figure 6.8 and Figure 6.9, respectively. The calculated ρ values are summarized in Table 6.2 and, as expected, commensurate with the calculated $\Delta\Delta G^{\ddagger}$ for R, Y and L_n (Figure 6.7) catalytic components within the OMBV and BV transitions states.[1,25]

Figure 6.8. Hammett plot of calculated $\log(k_x/k_H)$ versus the empirical sigma value (σ_p) for *para* substituents on $[(^x\text{bpy})\text{Pt}(\text{R})(\text{OY})]^+$ for the aryl migration transition state (R = *p*-X-C_6H_4, shown in blue (ρ_R); Y = 4-X-pyridine, shown in red (ρ_Y); ^{X}bpy = 4,4'-X-bpy, shown in green; X = NO_2, H, OMe, NMe_2).

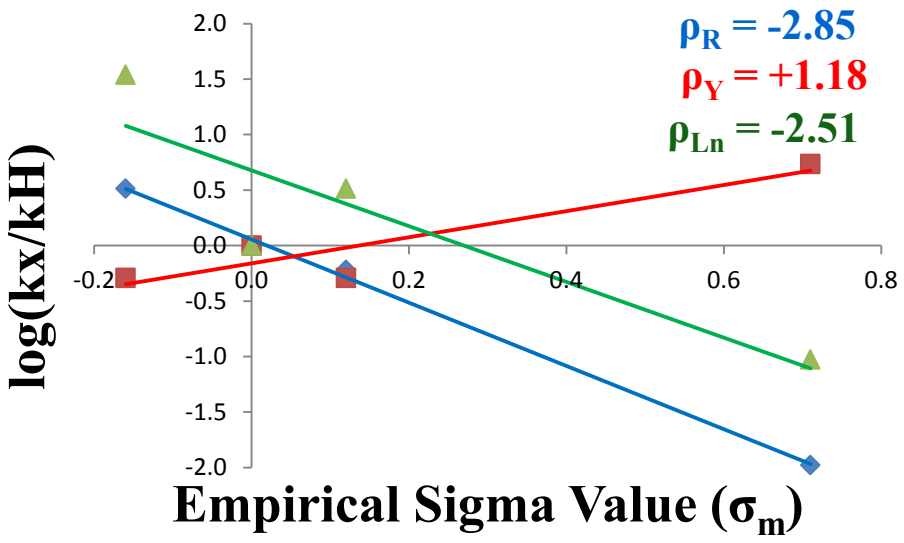

Figure 6.9. Hammett plot of calculated $\log(k_x/k_H)$ versus the empirical sigma value (σ_m) for *meta* substituents on $[(^{x}bpy)Pt(R)(OY)]^+$ for the aryl migration transition state (R = *m*-X-C_6H_4, shown in blue (ρ_R); Y = 3-X-pyridine, shown in red (ρ_Y); ^{X}bpy = 5,5'-X-bpy, shown in green; X = NO_2, H, OMe, NMe_2).

Table 6.2. Summary of calculated Hammett impact for OMBV and aryl migration transition states.

Catalytic Component	$\Delta\Delta G_{AM}^{\ddagger}$ (kcal/mol)	$\Delta\Delta G_{OMBV}^{\ddagger}$ (kcal/mol)[1]	ρ (AM)	ρ (OMBV)[1]
para-R	-4.4	-12.0	-2.0	-5.4
4-X-Y	+0.6	+4.2	+0.0	+1.8
4,4'-X-L_n	-3.0	+0.6	-1.4	+0.1
meta-R	-3.4	-	-2.9	-
3-X-Y	+1.4	-	+1.2	-
5,5'-X-L_n	-3.5	-	-2.5	-

6.5 Summary and Conclusions

A summary of all substituted moieties that were discussed in this paper is listed in Table 6.3. Comparing the aryl migration transition state free energy to that of the oxo-intermediate ($\Delta G^{OXO}{}_{AM}^{\ddagger}$) reveals negligible (< 2.5 kcal/mol) changes in the energetics upon modification of

the supporting ligand, leaving group, and migrating group substituents. This result implies that the oxo intermediate and the aryl migration transition state have similar electronic sensitivity to the electronic donating/withdrawing power of the various catalyst components. This is reasonable given the relatively early (*i.e.*, oxo-like) transition state geometries for aryl migration. Thus, stabilization/destabilization of the MCI relative to the aryl migration TS emerges as a critical factor in oxy-insertion of late transition metal-carbon bonds.

Table 6.3. Summary of calculated free energy barriers for aryl migration.

R	Y	L_n	$\Delta G^{MCI}_{AM}{}^{\ddagger}$ (kcal/mol)[a]	$\Delta G^{OXO}_{AM}{}^{\ddagger}$ (kcal/mol)[b]
Ph	Py	bpy	40.7	12.6
p-NO_2-Ph	Py	bpy	43.1	12.4
p-OMe-Ph	Py	bpy	39.9	12.8
p-NMe_2-Ph	Py	bpy	38.7	12.4
m-NO_2-Ph	Py	bpy	43.4	13.6
m-OMe-Ph	Py	bpy	41.0	12.5
m-NMe_2-Ph	Py	bpy	40.0	13.5
Ph	4-NO_2-Py	bpy	40.3	13.2
Ph	4-OMe-Py	bpy	39.9	12.9
Ph	4-NMe_2-Py	bpy	40.5	12.4
Ph	3-NO_2-Py	bpy	39.7	14.6
Ph	3-OMe-Py	bpy	41.1	12.6
Ph	3-NMe_2-Py	bpy	41.1	12.6
Ph	Py	4,4'-NO_2-bpy	42.0	12.0
Ph	Py	4,4'-OMe-bpy	39.7	13.3
Ph	Py	4,4'-NMe_2-bpy	39.0	13.1
Ph	Py	5,5'-NO_2-bpy	42.1	12.3
Ph	Py	5,5'-OMe-bpy	40.0	12.8
Ph	Py	5,5'-NMe_2-bpy	38.6	13.5

[a] $\Delta G^{MCI}_{AM}{}^{\ddagger}$ represents the aryl migration barrier relative to the metallo-Criegee intermediate
[b] $\Delta G^{MCI}_{AM}{}^{\ddagger}$ represents the aryl migration barrier relative to the oxo-intermediate

Shifting the transition state geometry from OMBV to one that is closer to aryl migration results in some beneficial alterations to the electronic impact of the various catalytic components. In the present research, the phenyl migrating group (R) within the aryl migration transition statewas shown to have a calculated impact factor of $\Delta\Delta G^{p}_{R}{}^{\ddagger}$ = -4.4 kcal/mol and a ρ_R = -2.0 for *para*

substitution, $\Delta\Delta G^{m}{}_{R}^{\ddagger}$ = -3.4 kcal/mol and a ρ_R = -2.9 for *meta* substituted aryl groups in which the rate is increased by the presence of EDGs. These are greatly diminished compared to the electronic impact on the OMBV transition state ($\Delta\Delta G_p{}^{BV}{}_{R}^{\ddagger}$ = -12.0 and ρ_R = -5.4).[1] The reduced sensitivity of the oxo-mediated mechanism to the migrating group could be an advantage in a methane functionalization catalyst given that methyl groups are extremely reluctant migrating groups in Baeyer-Villiger pathways. The leaving group component (Y) shows little to no impact for *para* and *meta* substituted moieties within the aryl migration transition state ($\Delta\Delta G^{p}{}_{Y}^{\ddagger}$ = +0.6 kcal/mol and a ρ_Y = 0.0 for *para* and $\Delta\Delta G^{m}{}_{Y}^{\ddagger}$ = +1.4 kcal/mol and a ρ_Y = +1.2 for *meta*).

The Pt–Y and Pt–R bond lengths and angles around the platinum center change negligibly for the various Y-substituted complexes. Thus, with little impact upon energetics and geometries the Y group may be considered a spectator ligand. This result is in contrast to the OMBV and organic BV scenarios where the leaving group had moderate impact ($\Delta\Delta G_p{}^{BV}{}_{Y}^{\ddagger}$ = +4.2 and ρ_Y = +1.8)[1] with rate accelerating occurring upon addition of EWGs. This result provides further support for the transition state continuum depicted in Figure 6.3, in that the leaving group is more intimately involved in the bond breaking/making of Baeyer-Villiger than migration transition states and thus would be expected to have a greater Hammett impact in the former. However, as the results in Table 6.3 imply, the (de)stabilization of the aryl migration transition state mimics that of the oxo intermediate preceding it. One may propose a primarily thermodynamic role for the oxidant in that stronger oxidants are expected to stabilize the oxo intermediate and hence by extension the migration TS in a two-step, redox based pathway for metal-carbon bond functionalization. One obvious caveat with respect to catalyst design is the expectation that the use of more potent oxidants may engender side reactions that degrade the catalyst.

The bipyridyl supporting ligand (L_n) was shown to have no impact in the OMBV transition state ($\Delta\Delta G_p{}^{BV}{}_{Ln}{}^{\ddagger}$ = +0.6 and ρ_Y = +0.1)[1]. Pushing the transition state geometry towards the aryl migration extreme increases the electronic impact of L_n ($\Delta\Delta G^p{}_{Ln}{}^{\ddagger}$ = -3.0 and ρ_{Ln} = -1.4 for *para* and $\Delta\Delta G^m{}_{Ln}{}^{\ddagger}$ = -3.5 and ρ_{Ln} = -2.5 for *meta*). The supporting ligand barriers are lowered by the presence of EDGs and hence alterations to the supporting ligand could aid in facilitating migration. In a catalyst design scenario enhanced kinetic sensitivity to supporting ligand is particularly encouraging for oxo-mediated oxy-insertion pathways as changing the supporting ligand is typically the most facile synthetic modification.

In closing, the data presented here lead us to hypothesize that OMBV and aryl migration transition states are intimately linked in a structural sense, Figure 6.3, through modification of the catalyst components and by the power of the oxidant. The latter plays largely a thermodynamic role in making the oxo intermediate more thermodynamically accessible. Pushing the transition state geometry toward the aryl migration extreme by altering the electronic impact of the various catalytic components R, Y and L_n in a favorable manner may result in improved catalytic conditions for selective partial oxidation of hydrocarbons. However, the data in Table 6.3 indicate that these components have in a global sense a modest impact as the smallest calculated $\Delta G^{MCI}{}_{AM}{}^{\ddagger}$ is 38.6 kcal/mol and the largest 43.4 kcal/mol, a total range of ~ 5 kcal/mol. Thus, we must conclude that among the catalyst components depicted in Figure 6.3 that the metal and oxidant have the most prominent role in controlling the oxy-insertion functionalization reaction crucial to selective oxidation of methane, benzene, and other hydrocarbons.

6.6 References

(1) Figg, T. M.; Cundari, T. R.; Gunnoe, T. B. *Organometallics* **2011**, 30, 3779-3785.

(2) Figg, T. M.; Webb, J. R.; Cundari, T. R.; Gunnoe, T. B. *J. Am. Chem. Soc.* **2012**, 134, 2332-2339.

(3) Figg, T.M.; Cundari, T. R. *Organometallics* **2012**, 31, 4998-5004.

(4) Olah, G. A.; Goeppert, A.; Surya Prakash, G. K. *J. Org. Chem.* **2009**, 74, 487-498.

(5) Webb, J. R.; Bolaño, T.; Gunnoe, T. B. *ChemSusChem* **2011**, 4, 37-49.

(6) Brown, S. N.; Mayer, J. M. *J. Am. Chem. Soc.* **1996,** 118, 12119-12133.

(7) Brown, S. N.; Mayer, J. M. *Organometallics* **1995,** 14, 2951-2960.

(8) Alsters, P. L.; Teunissen, H. T.; Boersma, J.; Spek, A. L.; Vankoten, G. *Organometallics* **1993**, 12, 4691-4696.

(9) Kamaraj, K.; Bandyopadhyay, D. *Organometallics* **1999**, 18, 438-446.

(10) Smeltz, J. L.; Boyle, P. D.; Ison, E. A. *J. Am. Chem. Soc.* **2011**, 133, 13288-13291.

(11) Conley, B. L.; Ganesh, S. K.; Gonzales, J. M.; Tenn, W. J.; Young, K. J. H.; Oxgaard, J.;

(12) Goddard, W. A.; Periana, R. A. *J. Am. Chem. Soc.* **2006,** 128, 9018-9019.

(13) Gonzales, J. M.; Distasio, R.; Periana, R. A.; Goddard, W. A.; Oxgaard, J. *J. Am. Chem. Soc.* **2007,** 129, 15794-15804.

(14) Asselt, A. V.; Trimmer, M. S.; Henling, L. M.; Bercaw, J. E. *J. Am. Chem. Soc.* **1998**, 110, 8254-9255.

(15) Matsunaga, P. T.; Hillhouse, G. L.; Rheingold, A. L. *J. Am. Chem. Soc.* **1993,** 115, 2075-2077.

(16) Matsunaga, P. T.; Mavropoulos, J. C.; Hillhouse, G. L. *Polyhedron* **1995**, 14, 175-185.

(17) Poverenov, E.; Efremenko, I.; Frenkel, A. I.; Ben-David, Y.; Shimon, L. J. W.; Leitus, G.; Konstantinovski, L.; Martin, J. M. L.; Milstein, D. *Nature* **2008**, 455, 1093-1096.

(18) Efremenko, I.; Poverenov, E.; Martin, J. M. L.; Milstein, D. *J. Am. Chem. Soc.* **2010**, 132, 14886-14900.

(19) Reyes, L.; Alvarez-Idaboy, J. R.; Mora-Diez, N. *J. Phys. Org. Chem.* **2009**, 22 643-649.

(20) Reyes, M.; Meunier, B. *Eur. J. Org. Chem.* **1999**, 737-750.

(21) Palmer, B. W.; Fry, A. *J. Am. Chem. Soc.* **1970**, 92, 2580.

(22) DeYonker, N. J.; Foley, N. A.; Cundari, T. R.; Gunnoe, T. B.; Petersen, J. L. *Organometallics* **2007**, *26*, 6604-6611.

(23) Bischof, Steven M., Cheng, Mu-Jeng; Nielsen, Robert J.; Gunnoe, T. Brent; Goddard, William A., III; Periana, Roy A. *Organometallics* **2011**, *30*, 2079-2082.

(24) Frisch, M. J. *et al.* Gaussian 09, Gaussian, Inc.: Wallingford, CT, **2009**.

(25) Becke, A. D. *J. Chem. Phys.* **1993**, 98, 1372– 1378.

(26) Becke, A. D. *J. Chem. Phys.* **1993**, 98, 5648– 5652.

(27) Stevens, W. J.; Basch, H.; Krauss, M., *J. Chem. Phys.* **1984,** *81*, 6026-6033.

(28) Cundari, T. R.; Stevens, W. J., *J. Chem. Phys.* **1993,** *98*, 5555.

(29) Stephens, P. J.; Devlin, F. J.; Chabalowski, C. F.; Frisch, M. J., *J. Phys. Chem.* **1994,** *98*, 11623-11627.

(30) Cossi, M.; Rega, N.; Scalmani, G.; Barone, V. J. *Comput. Chem.* **2003**, 24, 669.

(31) Barone, V.; Cossi, M. *J. Phys. Chem. A* **1998**, 286, 253.

(32) Hansch, C.; Leo, A.; Taft, R. W. *Chem. Rev.* **1991**, 91, 165-195.

CHAPTER 7

COOPERATIVITY BETWEEN LOW-VALENT IRON AND POTASSIUM PROMOTERS IN DINITROGEN FIXATION*

7.1 Introduction

Conversion of dinitrogen (N_2) into useful materials is desired for uses such as the production of ammonia (NH_3), one of the most important chemicals used in synthetic fertilizers.[1] However, N_2 is difficult to activate due to the inherent strength of the N≡N triple bond (~235 kcal/mol). The dominant industrial method for the reductive cleavage of N_2 and formation of NH_3 is the catalytic reduction of N_2 with dihydrogen (H_2) via the Haber-Bosch process. Due to its low cost, iron is commonly used to catalyze the Haber-Bosch process.[2] Potassium promoters improve the catalytic activity of iron surfaces, partially due to an increase in the rate constant for N_2 dissociation on the iron surface.[3] In synthetic compounds, cooperative binding of N_2 by iron and alkali metal ions has been shown to weaken the N–N bond more than iron alone, and this trend has been extended to chromium,[4] cobalt[5,6] and nickel.[7] However, these systems do not cleave the N-N bond. Further progress in cooperative N_2 activation requires better understanding of two key factors: (1) the reductive cleavage of the N_2 bond, and (2) the role of promoters such as potassium.

Recently, Holland and coworkers reported a soluble iron-β-diketiminate (≡ [Fe]) system that can cleave N_2 to give a bis(nitride) intermediate (Figure 7.1).[11] Relatively few Fe-nitride complexes have been reported in the literature that involve more than two iron centers interacting with nitride atoms, and no others are derived from N_2.[12,13] The complex in Figure 1 arises from cleavage of N_2, and has three [Fe] fragments interacting directly with nitrides and a fourth [Fe]

*This chapter is presented in its entirety from T. M. Figg, P. L. Holland, and T. R. Cundari "Cooperativity Between Low-Valent Iron and Potassium Promoters In Dinitrogen Fixation" Inorg. Chem., 2012, 51, 7546 with permission from the American Chemical Society.

interacting indirectly through a series of chlorine and potassium interactions. Though this system is not catalytic, the chemistry depicted in Figure 7.1 is a potential stepping stone to a better understanding of catalysts for solution phase N_2 fixation.

In this study, DFT calculations are employed to understand the role of cooperativity between multiple iron-β-diketiminate fragments. For example, how many iron atoms are needed to cleave the N_2 bond in the reduction step, and what intermediates are potentially involved? Theoretical calculations have greatly aided in understanding N-N bond cleavage.[8-10] The research reported here indicates that interaction of N_2 with more metal centers increases the N-N activation, and thus N_2 fixation benefits from cooperation between metals. The present calculations also yield insight into the effects of potassium promoters in N_2 fixation.[14]

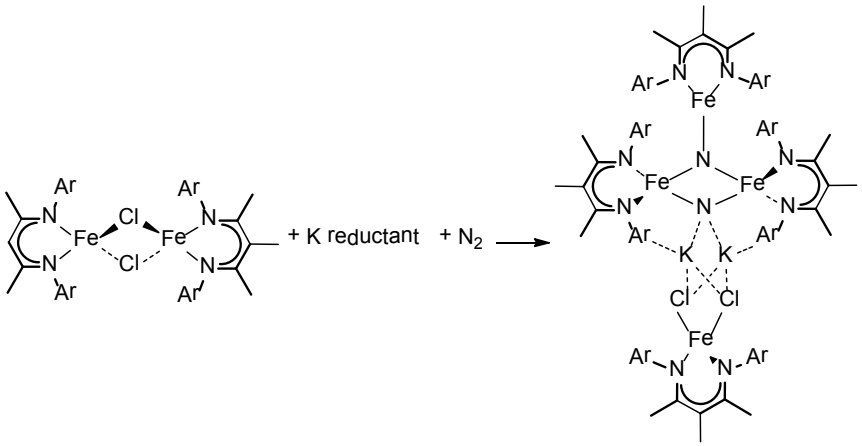

Figure 7.1. Structure of the soluble iron-β-diketiminate-nitride complex formed upon cleavage of the N_2 triple bond. Ar = 2,6-$C_6H_3Me_2$.

7.2 Computational Methods

Density functional theory (DFT) was used to facilitate comparison between the various ground states of the $[Fe]_3N_2$ and $[Fe]_3(N)_2$ species. The Gaussian 09 software package[15] was used for geometry optimizations and frequency calculations. The B3LYP/6-31+G(d) calculated geometries and properties of $[Fe]N_2$ and $[Fe]_2N_2$ species are similar to those previously reported

from MCSCF computations.[17-19] Additional continuum solvent corrections are computed in THF using the SMD formulation and are compared to the gas phase energetics.[20] Since computations on the monometallic and bimetallic Fe-β-diketiminate species have been reported previously,[17-19] the present contribution focuses on trimetallic species, the interactions of K^+ on important intermediates in an array of binding modes, and the role of reduction.

Various isomers of the $[Fe]_n$-N_2 complexes were calculated in all plausible spin states. Free energies are quoted relative to separated starting materials: (iron-β-diketiminate)$_n$ + N_2 (n = number of [Fe] fragments involved in the reaction). Bond lengths are given in Å. Initial attempts to model the tetra-iron complex in Figure 1 molecule with ONIOM techniques revealed that the substituents need to be modeled with full QM techniques to due to the importance of K^+/π-arene interactions. The ligands were thus truncated to $C_3N_2H_5^-$ for computational expediency; in previous reports, we have found that this truncation gives iron-dinitrogen complexes with metrical and spectroscopic parameters that agree well with experiment and faithfully represents the core electronic properties of larger β-diketiminate supporting ligands.[6,17-19] The studies here are limited to a single potassium ion and three iron atoms because the fourth iron atom in the complex reported by Holland *et al.*[11] interacts indirectly with the Fe_3N_2 core via K^+/π-arene interactions.

7.3 Results and Discussion

This paper explores the effect of sequentially adding Fe-β-diketiminate fragments to free N_2 in various binding modes. The experimental route to the complex in Figure 7.1 starts from potassium reduction of an iron(II)-β-diketiminate starting material to give a presumed iron(I) species that were modeled here as the unsaturated fragment iron-β-diketiminate. Previous work revealed that three-coordinate iron(I) gives strong backbonding into the π* orbitals of N_2, and

binding of a second fragment enhances N_2 bond lengthening.[17,19] A single [Fe] binds N_2 in an end-on (E) fashion in a quartet spin state, $\Delta G_{rel}(^4\text{E-FeN}_2)$ = -13 kcal/mol. The lowest energy bimetallic N_2 complex is end-on/end-on (EE) in a septet state, as seen experimentally for closely related compounds,[19] with $\Delta G_{rel}(^7\text{EE-Fe}_2\text{N}_2)$ = -40 kcal/mol. Binding of the second fragment is thus cooperative (defined here as the extra stabilization in a bimetallic complex beyond that expected from two monometallic interactions) by 40 – (2 × 13) = 14 kcal/mol. The ligation of a second E-Fe increases the N_2 bond length by 5%, from 1.127 to 1.187 Å.

The key advance here is to explore the interaction of more than two iron(I) fragments with N_2, and so potential binding modes were explored for a third [Fe] fragment interacting with N_2. Three isomers of trimetallic complexes were compared: end-on/end-on/side-on (abbreviated EES-Fe_3N_2), end-on/side-on/side-on (abbreviated ESS-Fe_3N_2), and all-side-on (abbreviated SSS-Fe_3N_2). Note that [S-Fe] indicates a side-on interaction of iron with N_2, which to our knowledge has never been observed experimentally in an iron complex; thus this study gives insight into the expected geometry of such an interaction. Various conformers within each family were explored; the lowest energy geometries are given in the figures.

The lowest energy neutral trimetallic isomer, Figure 7.2 (bottom), is calculated to be ^{10}EES-Fe_3N_2, ΔG_{rel} = -62 kcal/mol, with an N–N bond length of 1.234 Å. A ^{10}ESS-Fe_3N_2 linkage isomer, Figure 7.2 (top), d_{NN} = 1.284 Å, is only 6 kcal/mol higher than the calculated lowest energy isomer. SSS-Fe_3N_2 isomers were calculated to be thermodynamically unfavorable (by ≥ 12 kcal/mol) with respect to those in Figure 7.2, and are thus not discussed further. Binding of the third [Fe] fragment to ^{7}EE-Fe_2N_2 to give ^{10}EES-Fe_3N_2 is found to release 22 kcal/mol, which is 5 kcal/mol less exergonic than binding of a second [Fe] fragment to ^{4}E-FeN_2. Importantly,

both EES and ESS isomers are energetically accessible, and each lengthens the N-N bond significantly more than two iron fragments in ^{7}E-Fe_2N_2.

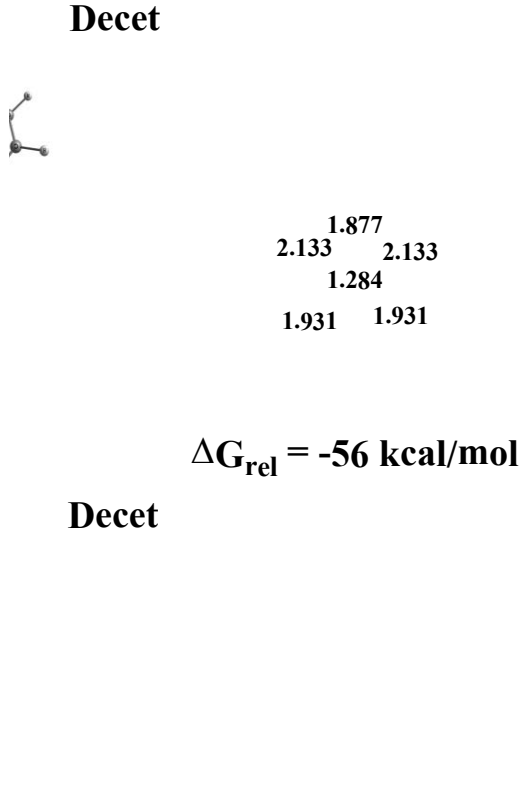

Figure 7.2. B3LYP geometries of ^{10}EES-Fe_3N_2 (top) and ^{10}ESS-Fe_3N_2 (bottom). The superscript numeral denotes the lowest energy multiplicity ($2S + 1$). Bond lengths in Å.ΔG_{rel} is calculated relative to isolated [Fe] and N_2.

Interestingly, ^{6}ESS-$Fe_2(N)_2$, an isomer with a cleaved N–N bond where $(N)_2$ denotes a bis(nitride) complex, was also located (Figure 7.3). This complex has a N···N distance of 2.598 Å and a relative ΔG_{rel} of -40 kcal/mol. One of the two nitrides in this species is attached to only two iron atoms. This nitride nitrogen forms an apparent double bond to one of the iron atoms

with d_{FeN} = 1.654 Å, a relatively strained interaction that may explain why it is 16 kcal/mol less stable than ^{10}ESS-Fe_3N_2 (Figure 7.4).

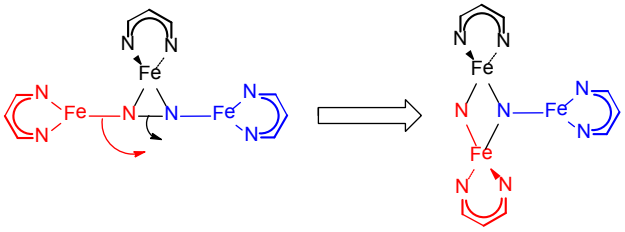

Figure 7.3. Potential energy scans (red/black arrows) between EES-Fe_3N_2 (left) and ESS-$Fe_3(N)_2$ (right) indicate small barriers to N_2 scission.

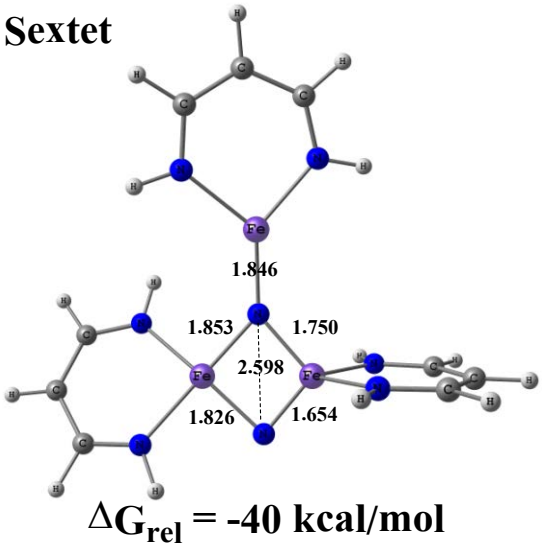

Figure 7.4. B3LYP calculated geometry of ^{6}ESS-$Fe_3(N)_2$ with an broken N_2 bond. Bond lengths in Å. ΔG_{rel} is calculated relative to isolated [Fe] and N_2.

Transformation from EES-Fe_3N_2 to ESS-$Fe_3(N)_2$ was explored by scanning the potential energy surfaces of low energy sextet, octet, and decet spin state pathways, Figure 7.3. The scans reveal low (< 5 kcal/mol) barriers for the transformation on each of the three potential-energy surfaces. Thus, calculations imply that isomerization could be kinetically rapid as a part of the reaction leading to N_2 cleavage, but that the N–N cleavage is somewhat thermodynamically unfavorable for the neutral cluster.

Inspection of Figure 7.1 indicates several K^+ directly interacting with the π-system of the aryl substituents and the nitrides.[8] Several potential roles of the potassium in the N-N cleavage can be envisioned: K^+ may enforce geometrical constraints, stabilize the nitride (N^{3-}), and/or increase the π-backbonding capacity of the Fe centers as proposed for the heterogeneous catalyst.[1] To assess the impact of K^+ on N_2 fixation, a K^+ ion was placed in several locations in proximity to the N_2 moiety for the low energy dinitrogen and dinitride structures (*i.e.*, ^{10}EES-Fe_3N_2 with an intact N_2 and ^{6}ESS-$Fe_3(N)_2$ with a broken N_2 bond), respectively. Addition of K^+ to ^{10}EES-Fe_3N_2 always rearranges upon DFT geometry optimization to the structure in Figure 7.5 (top).

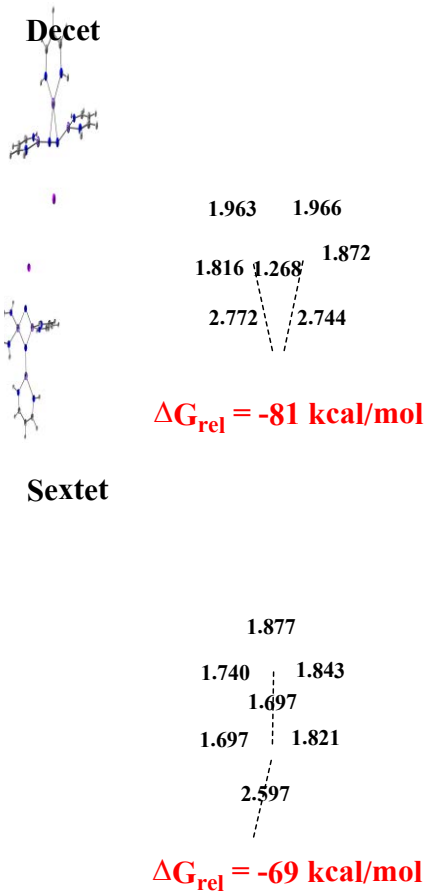

Figure 7.5. B3LYP structures resulting from addition of K^+ to ^{10}EES-Fe_3N_2 (top) and ^{6}ESS-$Fe_3(N)_2$ (bottom). ΔG_{rel} is calculated relative to isolated [Fe] and N_2.

Binding of K^+ to ^{10}EES-Fe_3N_2 is exergonic by 19 kcal/mol and the calculated lowest energy multiplicity of EES-Fe_3N_2K remains a decet. The N–N bond is elongated from 1.234 to 1.268 Å (3%) upon K^+ addition. Addition of K^+ to ^{6}ESS-$Fe_3(N)_2$ yielded the geometry in Figure 7.5 (bottom) with the sextet remaining the lowest energy spin state. Addition of K^+ to ^{6}ESS-$Fe_3(N)_2$ is 11 kcal/mol more exergonic than K^+ addition to ^{10}EES-Fe_3N_2. Thus, potassium ion addition stabilizes the bis(nitride) product more than the bridged N_2 complex in the gas phase. However, the nitride complex continues to have one unusually short Fe–N bond.

Addition of K^+ to ^{6}ESS-$Fe_3(N)_2$ makes the resulting bis(nitride), Figure 7.4, more energetically accessible relative to the dinitrogen isomers, with a free energy for ^{6}ESS-$Fe_3(N)_2K^+$ → ^{10}EES-$Fe_3N_2K^+$ of only 12 kcal/mol, roughly half the comparable isomerization free energy in the absence of K^+. Analysis of calculated atomic charges suggests that greater stabilization of the N^{3-} ligand by K^+ coordination is responsible for the diminution of the endergonicity in the nitrogen scission reaction.

Finally, an electron was added to the ^{10}EES-Fe_3N_2 complex to mimic reduction by the fourth Fe(I) fragment in the experimental reaction. This yielded $[^9$EES-$Fe_3N_2]^-$ as the lowest energy state, and resulted in only slight geometric distortion (RMSD = 0.22 Å). The largest perturbation was elongation of one Fe–N bond from 1.976 to 2.089 Å for the [S-Fe] fragment, which coincided with an increase of atomic charge on the nitrogen involved in the bond, from -0.19 to -0.58. The added electron occupies a non-bonding, Fe-based orbital, Figure 7.6, consistent with the minor change in geometry upon reduction. Thus, addition of a single electron to the tri-iron structure has a minor impact on the degree of N_2 activation by trimetallic EES-Fe_3N_2.

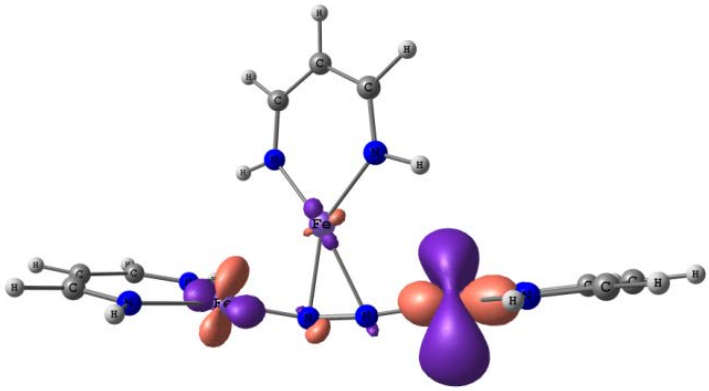

Figure 7.6. HOMO for ^{9}[EES-Fe_3N_2]$^{-}$ complex in which the added electron occupies a non-bonding metal-based orbital.

On the other hand, addition of an electron to ^{6}ESS-$Fe_3(N)_2$ gave a significant effect. Reduction yielded [^{5}ESS-$Fe_3(N)_2$]$^{-}$ as the lowest energy state. The distance between the nitride ligands is shortened from 2.598 to 2.587 Å. The added electron was found to occupy a bonding Fe-nitride orbital, Figure 7.7. A K^{+} ion was added to the reduced complexes [^{9}EES-Fe_3N_2]$^{-}$ and [^{5}ESS-$Fe_3(N)_2$]$^{-}$ changing the overall charge on the cluster model to neutral; the resulting complexes were found to possess the same ground spin states as their anionic precursors, Figure 7.8.

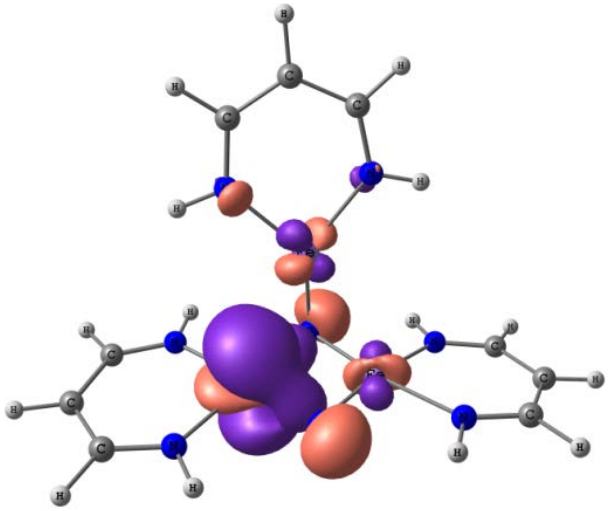

Figure 7.7. HOMO for [^{5}ESS-$Fe_3(N)_2$]$^{-}$ in which the added electron occupies a bonding metal-nitride based orbital.

The addition of K^+ to the reduced species makes the [^{5}ESS-$Fe_3(N)_2K$] cluster 3 kcal/mol more stable than [^{9}EES-Fe_3N_2K], Figure 7.8.

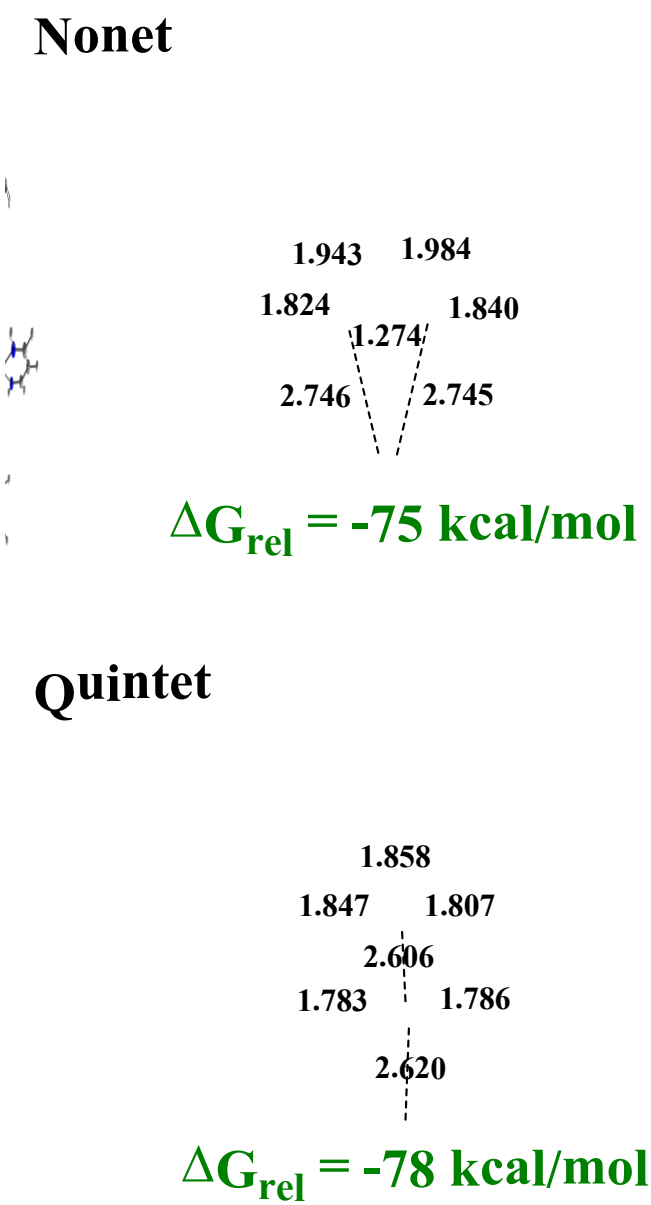

Figure 7.8. B3LYP structures resulting from addition of K^+ to [^{9}EES-Fe_3N_2]K (top) and [^{5}ESS-$Fe_3(N)_2$]K (bottom). ΔG_{rel} is calculated relative to isolated [Fe], K^+ and N_2.

It also gives a structure in which the Fe-N bonds are closer to the experimental crystal structure where the Fe-N bonds proximal to coordinated K^+ are shorter than the corresponding distal Fe-N

bond lengths. Therefore, addition of three iron(I) fragments, a K^+ ion, and an electron makes N-N cleavage favorable, presumably because of the stronger interaction of the potassium cation with the anionic nitride core.

While gas-phase simulations may more appropriately model an industrial nitrogen fixation catalyst, inclusion of solvent effects is more pertinent to attempts to create a homogeneous version. Continuum solvation corrections in THF were thus computed and compared to the gas phase energetics to assess the impact of solvation on the reactions of interest. The THF thermodynamics, Figure 7.9 (right, blue border), are calculated to be similar to the gas phase models with one interesting difference. The thermodynamics of ^{10}EES-Fe_3N_2 → ^{6}ESS-$Fe_3(N)_2$ is little changed by inclusion of solvent effects, ΔG_{gas} = +22.0 kcal/mol, ΔG_{THF} = +21.5 kcal/mol, Figure 7.9. Similarly, there is a mild solvent influence calculated for the K^+ and K-ligated reactions, *e.g.*, $^{10}[EES\text{-}Fe_3N_2K]^+ \rightarrow {}^{6}[ESS\text{-}Fe_3(N)_2K]^+$, ΔG_{gas} = +11.3 kcal/mol, ΔG_{THF} = +14.9 kcal/mol, Figure 7.9. However, reduction upon the nitride to bis(nitride) transformation is significantly modulated by solvent, going from endergonic, ΔG_{gas} = +8.4 kcal/mol, to mildly exergonic, ΔG_{THF} = -0.5 kcal/mol for $^{9}[EES\text{-}Fe_3N_2]^- \rightarrow {}^{5}[ESS\text{-}Fe_3(N)]^-$, Figure 9. Comparing the relative ΔG's in gas ($\Delta\Delta G_{gas}$) and solvent ($\Delta\Delta G_{THF}$) indicates that K^+ becomes less impactful ($\Delta\Delta G_{gas}(K^+)$ = 10.7 kcal/mol, $\Delta\Delta G_{THF}(K^+)$ = 6.6 kcal/mol) than reduction of the system ($\Delta\Delta G_{gas}(e^-)$ = 13.6 kcal/mol, $\Delta\Delta G_{THF}(e^-)$ = 22.0 kcal/mol) upon the inclusion of continuum THF solvent effects.

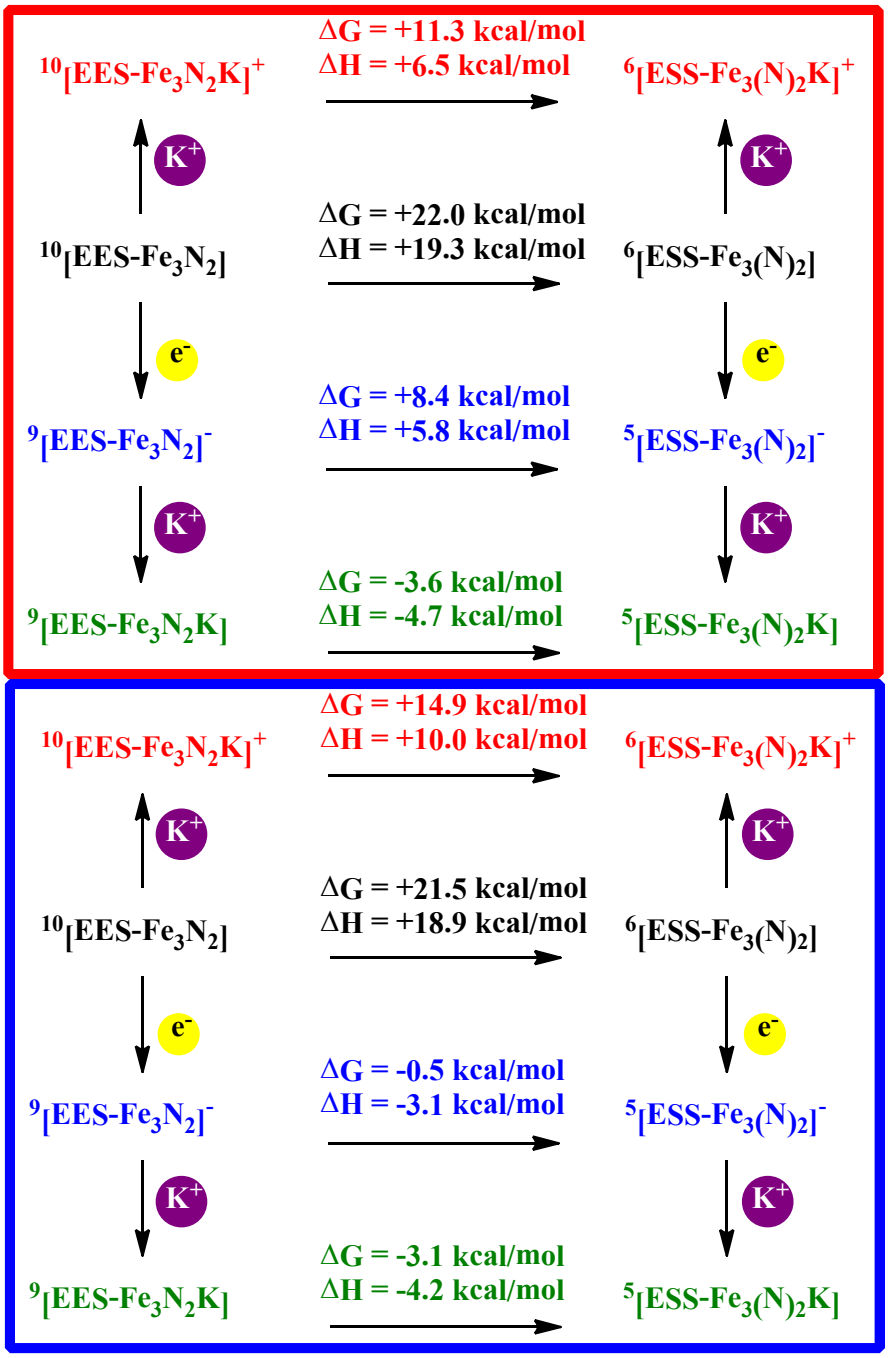

Figure 7.9. Ladder of calculated gas phase (red border) and solution phase (blue border) relative free energies (ΔG_{rel}) of dinitrogen (left) and bis(nitride) (right) species. Additions of K^+ (red) and electron (blue) to the neutral species (black) are compared ΔG). Also, addition of K^+ (green) to the reduced species (blue) is also calculated.

7.4 Conclusions

The present DFT simulations of the sequential addition of Fe-β-diketiminate fragments to dinitrogen are important because they show a reasonable series of metal binding and reduction events that cleave N_2 to give a $Fe_3(N)_2K$ core like that in a recent experimental report.[7] In addition to this mechanistic insight, it reveals that three reduced iron centers acting in a cooperative fashion make N_2 cleavage thermodynamically feasible. As summarized in Figure 7.9, the K^+ promoter stabilizes the nitride ligand of the "fixed" tri-iron-bis(nitride) isomers by about 10 kcal/mol relative to the N_2 isomers, and N-N cleavage is only favorable when an added electron *and* potassium are present. However, including a polar continuum solvent reduces the impact of the K^+ on stabilizing the reduced tri-iron-bis(nitride). The results demonstrate that the cleavage of N-N bonds by a reduced iron fragment is greatly influenced by potassium, and also illustrate the impact of cooperative Fe binding upon N_2 activation, indicating that at least three iron fragments are needed to cleave N_2.

7.5 References

(1) Schlögl, R. in *Handbook of Heterogeneous Catalysis,* Ertl, G.; Knözinger, G.; Schüth, F.; Weitkamp, J., Eds. (Wiley-VCH, Weinheim, Germany, 2nd ed., **2008**), vol. 5, pp. 2501–2575.

(2) Mittasch, A. *Geschichte der Ammoniaksynthese*; Verlag Chemie: Weinheim, **1951**.

(3) Strongin, D. R.; Somorjai, G. *J. Catal.* **1988**, *109*, 51.

(4) Monillas, W. H.; Yap, G. P.; Theopold, K. H. *Inorg. Chim. Acta* **2011**, *369*, 103.

(5) Ding, K; Brennessel, W. W.; Holland, P. L. *J. Am. Chem. Soc.* **2009**, *131*, 10804.

(6) Ding, K.; Pierpont, A. W.; Brennessel, W. W.; Lukat-Rodgers, G.; Rodgers, K. R.; Cundari, T. R.; Bill, E.; Holland, P. L. *J. Am. Chem. Soc.* **2009**, *131*, 9471.

(7) Horn, B.; Pfirrmann, S.; Limberg, C.; Herwig, C.; Braun, B.; Mebs, S.; Metzinger, R. *Z. Anorg. Allg. Chem.* **2011**, *637*, 1169.

(8) Schrock, R.R., *Angew. Chem. Int. Ed.* **2008**, *47*, 5512.

(9) Khoroshun, D. V.; Musaey, D. G.; Morokuma, K. *Mol. Phys.* **2002**, *100*, 523.

(10) Cavigliasso, G.; Wilson, L.; McAlpine, S.; Attar, M.; Stranger, R.; Yates, B.F., *Dalton Trans.,* **2010**, *39*, 4529.

(11) Rodriguez, M. M.; Bill, E.; Brennessel, W. W.; Holland, P. L. *Science* **2011**, *334*, 780.

(12) Bennett, M. V.; Stoian, S.; Bominaar, E. L.; Münck, E.; Holm, R. H. *J. Am. Chem. Soc.* **2006**, *127*, 12378.

(13) Bennett, M. V.; Holm, R. H. *Angew. Chem. Int. Ed.* **2006**, *45*, 5613.

(14) Strongin, D. R.; Carrazza, J.; Bare, S. R.; Somorjai, G. A. *J. Catal.* **1987**, *103*, 213.

(15) Frisch, M. J. *et al. Gaussian 09*, Gaussian Inc.: Wallingford, CT, **2009**.

(16) Mortensen, J. J.; Hansen, L. B.; Hammer, B.; Nørskov, J. K. *J. Catal.* **1999**, *182*, 479.

(17) Smith, J. M.; Lachicotte, R. J.; Pittard, K. A.; Cundari, T. R.; Lukat-Rodgers, G.; Rodgers, K. R.; Holland, P. L. *J. Am. Chem. Soc.* **2001,** *123,* 9222.

(18) Pierpont, A. W.; Cundari, T. R. *J. Coord. Chem.* **2011**, *64*, 3123.

(19) Smith, J. M.; Sadique, A. R.; Cundari, T. R.; Rodgers, K. R.; Lukat-Rodgers, G.; Lachicotte, R. J.; Flaschenriem, C. J.; Vela J.; Holland, P. L. *J. Am. Chem. Soc.* **2006**, *128*, 756.

(20) Marenich, A. V.; Cramer, C. J.; Truhlar, D. G. *J. Phys. Chem.* **2009**, *113*, 6378.

CHAPTER 8

CLOSING REMARKS

8.1 Chapter Summary

In chapter 3, a Hammett analysis of platinum-mediated oxy-insertion into Pt-aryl bonds is performed using DFT calculations. Modeled transformations involve the conversion of cationic Pt(II)–aryl complexes, $[(^{X}bpy)Pt(R)(OY)]^{+}$ (R = *p*-X-C_6H_4; Y = 4-X-pyridine; ^{X}bpy = 4,4'-X-bpy; X = NO_2, H, NMe_2), to the corresponding $[(^{x}bpy)Pt(OR)]^{+}$ complexes via an organometallic Baeyer-Villiger (BV) pathway. Computational modeling predicts that incorporation of an electron-deficient NO_2 group at the 4-position of pyridine-*N*-oxide lowers the activation barrier to the organometallic BV transformation. In contrast, computational studies reveal that increasing the donor ability of the migrating aryl group, by placement of NMe_2 at the *para*-position, lowers the activation barrier to the oxy-insertion step. The impact on the calculated activation barrier is greater for variation of the R group than for modification of Y of the oxygen delivery reagent. For the *p*-NO_2/*p*-NMe_2-substituted aryl migrating groups (R), the $\Delta\Delta G^{\ddagger}$ for X = NMe_2 versus X = NO_2 is 12 kcal/mol, which is three times larger than calculated for the changes that occur upon substitution of NO_2 and NMe_2 groups ($\Delta\Delta G^{\ddagger} \sim 4$ kcal/mol) at the 4-position of the pyridine group. For these Pt(II) complexes with bipyridine (bpy) supporting ligands, the influence of modification of the bpy ligand is calculated to be minimal with $\Delta\Delta G^{\ddagger} \sim 0.4$ kcal/mol for the oxy-insertion of bpy ligands substituted at the 4/4' positions with NMe_2 and NO_2 groups. Overall, the predicted activation barriers for oxy-insertion (from the YO adducts $[(^{X}bpy)Pt(R)(OY)]^{+}$) are large, and in most cases are > 40 kcal/mol, although some calculated $\Delta G^{\ddagger}$'s are as low as 32 kcal/mol.

In chapter 4, calculations surveying the impact of metal identity on Bayer-Villiger type insertions were carried out in an effort to identify promising new systems. The reaction under study involved four and six coordinate systems: $[(bpy)_xM(Me)(OOH)]^n \rightarrow [(bpy)_xM(OMe)(OH)]^n$ (x = 1 or 2; bpy = 2,2'-bipyridyl; n is varied to maintain the d-electron count at d^6 or d^8). Six square planar d^8 complexes (Pt(II), Pd(II), Ni(II), Ir(I), Rh(I) and Co(I)) and eight octahedral d^6 systems (Ir(III), Rh(III), Co(III), Fe(II) Ru(II), Os(II), Mn(I) and Tc(I)) were studied. Using DFT calculations, the structures and energies of ground state and transition state species were elucidated. This study resulted in clear trends in calculated $\Delta G^{\ddagger}$'s for the O-atom insertions. The organometallic Baeyer-Villiger insertions are favored by lower coordination numbers (x = 1 versus x = 2), earlier transition metals and first row (3d) transition metals.

In chapter 5, an extremely rare example of a 3d metal mediating the oxy-functionalization of metal-carbon bonds was explored. These systems are based on a series of Ni(II) alkyl complexes reacting with nitrous oxide reported by Hillhouse and coworkers in which the mechanism was never fully elucidated. A computational study was performed on bipyridyl nickel metallacycles that form nickel alkoxides upon reaction with N_2O to attain insight for future catalyst design for oxygen atom transfer reactions. Two possible mechanisms were explored. Of the two pathways, the computations suggest that the preferred mechanism proceeds through a Ni–oxo intermediate followed by alkyl migration of the nickel–carbon bond to form an alkoxide. Oxo formation was computed to be the rate-determining step with a free energy barrier of 29.4 kcal/mol for bpyNi(II) (cyclo-$(CH_2)_4$). Complexes that contain sp^2-hybridized molecules at the β-carbon site within the metallacycle ring do not undergo oxy-insertion due to elevated barriers. While exploring insertion with another oxidant, namely pyridine-N-oxide, it was found that N_2O is critical for net oxy-insertion with this complex due to the substantial thermodynamic

advantage of N_2 expulsion. Reaction with pyridine-N-oxide necessitated expulsion of a "worse" leaving group, resulting in much higher barriers ($\Delta G^{\ddagger}$ = 49.7 kcal/mol) for the oxo-formation step.

In chapter 6, a computational Hammett analysis of oxy-insertion into platinum–aryl bonds was performed. Modeled transformations involve the two-step conversion of $[(^{X}bpy)Pt(R)(OY)]^{+}$ (R = *p*- or *m*-X-C_6H_4; Y = 4- or 3-X-pyridine; ^{X}bpy = 4,4'- or 5,5'-X-bpy; X = NO_2, H, OMe, NMe_2) proceeding through a Pt–oxo intermediate to form aryloxide $[(^{X}bpy)Pt(OR)(Y)]^{+}$, which contrasts the one-step non-redox (Baeyer-Villiger) oxy-insertion. A structural connection was proposed between redox and non-redox transition states, linked to, among other parameters, oxidant identity. The electronic impact of the catalytic components was compared to previous Hammett studies on OMBV transformations. The Hammett sensitivity for aryl migration is diminished for the migrating group (R) and leaving group (Y), components as compared to OMBV transitions, while the bipyridine supporting ligand (L_n) has an increased impact. The Hammett impact of R, Y and L_n upon the aryl migration transition state is small in a global sense, *ca.* 5 kcal/mol; therefore, we conclude that the metal and oxidant are the most important factors in controlling oxy-insertion kinetics for these late metal systems. These results also point to a possible mechanistic advantage for redox over non-redox functionalization of hydrocarbons to alcohols.

In chapter 7, a DFT study was performed to understand the role of cooperativity between iron-β-diketiminate fragments and potassium promoters in N_2 activation. Sequential addition of iron fragments to N_2 reveals that a minimum of three iron centers interact with N_2 in order to break the triple bond. The potassium promoter stabilizes the N^{3-} ligand formed upon N_2 scission, thus making the activated iron-nitride complex more energetically accessible. Reduction of the

complex and stabilization of N^{3-} by K^+ have similar impact on the energetics in the gas phase. However, upon inclusion of continuum THF solvent effects, coordination of K^+ has a reduced influence upon the overall energetics of dinitrogen fixation; thus, reduction of the trimetallic Fe complex becomes more impactful than coordination of K^+ vis-à-vis N_2 activation upon the inclusion of solvent effects.

8.2 Conclusions

The results presented in chapters 3 - 6 lead to several salient conclusions. Late transition metal mediated oxy-insertion into metal–carbon bonds will be difficult. The utilization of 3d metals provide a promising avenue; however, competing and non-specific radical chemistry may be difficult to prevent. Attempts to extend non-redox organometallic Baeyer-Villiger mechanisms to non-d^0 systems is unlikely due to the formation of a transition metal oxo/oxyl complex being energetically more favorable in all cases studied thus far. A connection between non-redox and redox mediated pathways was proposed in chapter 5 and further evaluated in chapter 6. Pushing towards the redox extreme affords more favorable catalytic conditions making the oxidant and metal identity the key players in late metal mediated oxy-insertion reactions. Three further studies can be proposed to further improve this area of study. First, investigate the role of the oxidant in the two mechanistic pathways. This is key to fully elucidate the details of the connection between these two pathways. Second, a study of the d-count dependence would also be of interest as most of the complexes studied in this dissertation are either d^6 or d^8 systems. What about other d-counts? Will OMBV reactions truly only be favored for d^0 closed shell systems? Third, a study looking into a different family of supporting ligands would be of interest. One possible ligand family includes the use of redox active or non-innocent ligands that could help avoid the possible problem of 1 e-/radical chemistry prevalent in 3d

metal chemistry. One may propose that non-innocent ligands could avoid one-electron chemistry by an additional 1 e- oxidation/reduction from the ligand effectively mimicking a 2-electron oxidation/reduction. Thus, a comprehensive series of computational studies involving the role of oxidant, d-count, and exploration of different ligand families could be of great interest for late transition metal mediated C–O bond forming reactions.

The results presented in chapter 7 suggest that three iron-β-diketiminate fragments bound to N_2 are needed to completely cleave the N_2 bond; while the role of potassium was suggested to aid in the reduction of the iron center and stabilize the terminal nitride. However, the full system involves a fourth fragment bound through a series of potassium and chlorine interactions. A computational study to better understand the role of this fourth metal fragment would be of interest in designing future homogeneous systems.